ABSTRACT

Title of dissertation: IMPACTS OF FAIR-WEATHER CUMULUS CLOUDS, BAY BREEZES, AND LANDUSE ON URBAN AIR QUALITY AND CLIMATE

Christopher P. Loughner
Doctor of Philosophy, 2011

Dissertation directed by: Dr. Dale J. Allen
Department of Atmospheric and Oceanic Science

Professor Russell R. Dickerson
Department of Atmospheric and Oceanic Science

Fair-weather cumulus clouds, bay breezes, and land use influence air quality and climate. The impacts of urban land surface changes and model resolution on fair-weather cumulus clouds, bay breezes, air quality, and climate are examined. As model resolution increases, more pollutants are transported aloft through fair-weather cumulus clouds causing an increase in the rate of sulfur dioxide conversion to sulfate aerosols and an increase in boundary layer venting. As model resolution increases, a larger temperature gradient develops along the shoreline of the Chesapeake Bay causing the bay breeze to form sooner, push farther inland, and loft more pollutants upward. This stronger bay breeze results in low-level convergence, a buildup of near surface ozone over land and a decrease in the land-to-sea flux of ozone and ozone precursors. Also, an examination of the sensitivity of sulfur dioxide to sulfate conversion to different model cloud parameters shows the importance of accurately simulating clouds to obtain accurate sulfate concentrations. To analyze the impact of urbanization on the atmosphere, an urban tree parameterization is developed for the Weather Research and Forecasting model coupled

with an urban canopy model (WRF-UCM) to determine how urban trees can dampen the urban heat island (UHI). Adding vegetation decreases the (subgrid-scale) surface air temperature due to tree shading and evapotranspiration. The impact of building height on the UHI shows that shorter urban buildings have higher daytime surface temperatures due to less shading and lower nighttime temperatures due to less longwave radiative trapping in urban street canyons. The WRF-UCM with urban trees is utilized with an air quality model to investigate how urban vegetation changes impact air quality. Cooling due to planting urban trees is expected to improve air quality. However, for one case study that does not include anthropogenic emissions reductions due to cooling from increased vegetation, adding trees in the model results in higher ground level ozone concentrations due to a shallower planetary boundary layer and more pollutants converging near a stronger bay breeze near Baltimore, MD. Future work incorporating changes in anthropogenic emissions with changes in urban vegetation will help quantify how urban trees impact air quality.

IMPACTS OF FAIR-WEATHER CUMULUS CLOUDS, BAY BREEZES, AND LAND USE ON URBAN AIR QUALITY AND CLIMATE

by

Christopher P. Loughner

Dissertation submitted to the Faculty of the Graduate School of the
University of Maryland, College Park, in partial fulfillment
of the requirements for the degree of
Doctor of Philosophy
2011

Advisory Committee:

Dr. Dale J. Allen, Co-Chair / Research Advisor
Professor Russell R. Dickerson, Co-Chair / Academic Advisor
Professor Da-Lin Zhang
Dr. Kenneth E. Pickering
Professor Sheryl H. Ehrman

Acknowledgements

I would especially like to thank my research advisor, Dale Allen, as well as the rest of my Advisory Committee, Russ Dickerson, Ken Pickering, Da-Lin Zhang, and Sheryl Ehrman, for their inspiration and guidance. Thanks to Jeff Stehr for helping me relate my research to policy oriented professionals and Patti Castellanos for guidance on using SMOKE. I would also like to thank Bill Stockwell, my master's degree advisor, for getting me started in the atmospheric chemistry field and continued guidance and support. Finally, thank you to my family for their love and support.

Table of Contents

List of Tables

List of Figures

Chapter 1: Introduction

1.1 Background and motivation

The production of secondary air pollutants and the accumulation and dispersion of pollutants depends on emissions, meteorology, and the chemical composition of the atmosphere. Air pollution may degrade human health and natural resources as well as alter the radiative budget and cloud properties affecting Earth's climate and weather systems. A change in land surface characteristics can alter weather and climate and therefore impact air quality. Understanding air pollution formation processes and interactions between air quality, weather, climate, and land surface processes will aid in developing air pollution and climate change mitigation plans and forecasting air quality, weather, and climate.

1.1.1 Air pollution impacts on human, terrestrial, and aquatic health

Tropospheric ozone is a secondary pollutant, harmful to human health. High concentrations of ozone near the surface may cause permanent lung damage (Mudway and Kelly, 2000). Tropospheric ozone is formed through complex chemical and photochemical reactions involving nitrogen oxides, volatile organic compounds (VOCs), and carbon monoxide. Also, ground-level aerosols may produce heart and lung disease (Docker et al., 1993; Samet et al., 2000). Aerosols can be emitted directly into the atmosphere and form through reactions in the atmosphere. The U.S. Environmental Protection Agency (EPA) recognizes the health hazards of ground-level ozone and

aerosols and set National Ambient Air Quality Standards (NAAQS) that include ozone and aerosol concentration limits.

Air pollution is also harmful to land and aquatic ecosystems. High ozone concentrations damage plants and reduce crop yields (Booker et al., 2009; Fishman et al., 2010; Sanders et al., 1992). Sulfate and nitrate aerosols contribute to acid precipitation, which can make lakes and streams uninhabitable for fish. Acid precipitation can also erode buildings, monuments, and paint on cars. Nitrogen deposited into watersheds degrades river and coastal water quality by causing more algae blooms. These algae blooms block sunlight preventing underwater grasses from growing. The decrease in these grasses lowers dissolved oxygen levels to dangerous levels for fish and shellfish (Moffat, 1998; Morgan and Owens, 2001, Galloway et al., 2003; NRC, 2000).

1.1.2 Air pollution impacts on weather and climate

Tropospheric ozone and aerosols impact the radiative budget and therefore climate (Shine, 2000; Fishman et al., 1979). Ozone is a greenhouse gas that absorbs infrared radiation emitted by Earth and contributes to climate change. Scattering aerosols reflect solar radiation away from Earth causing a cooling effect on the climate. On the other hand, black carbon aerosols absorb radiation contributing to a warming climate. Also, black carbon aloft causes the upper atmosphere to warm, therefore stabilizing the atmosphere and preventing cloud formation and/or inhibiting convection (Hansen et al., 1997). This further contributes to a warming climate since clouds have a high albedo and reflect solar radiation away from Earth's surface.

Aerosols can also lengthen the lifetime of a cloud and alter precipitation processes. The formation of precipitation depends largely on the presence of aerosols.

Cloud droplets form when water vapor condenses onto small particles or cloud condensation nuclei (CCN) (Wallace and Hobbs, 1977). Increasing the number of CCN produces more numerous but smaller cloud droplets (Toon, 2000). Consequently, pollution increases the amount of aerosols in the atmosphere that act as CCN causing cloud droplets to be smaller and more numerous producing 'whiter' clouds that increase the amount of solar radiation reflected by clouds (Twomey, 1974). In addition, the cloud droplet growth rate is dependent on droplet radius so droplets in polluted clouds grow less quickly than droplets in unpolluted clouds (Toon, 2000). Smaller droplets may not be able to fall to the surface before evaporating. NASA satellite imagery has been used to show polluted clouds from urban and industrial sources contain smaller cloud droplets and a lower precipitation rate than clean clouds (Rosenfeld, 2000). Long-lived polluted clouds result in reduced precipitation formation near the pollutant source, but the cloud water is eventually converted to precipitation further downwind of the pollution source causing enhanced precipitation further downwind (Rosenfeld, 2006).

1.1.3 Weather impacts on air pollution

Meteorology is an important component in the production of secondary pollutants and accumulation of air pollution. Wind patterns determine where pollutants are transported and help determine the chemical composition of the atmosphere in a specific area, therefore helping to determine what molecular collisions take place that may result in a chemical reaction and formation of secondary air pollutants. Stagnant conditions allow pollutants to accumulate in one location while high wind events disperse pollutants (U.S. Environmental Protection Agency, 2006).

Localized air circulation patterns, like a sea breeze, bay breeze, or lake breeze, influence pollutant dispersion and accumulation. A sea breeze forms during the day due to differential heating along a coastline, with relatively warm near surface air temperature over the land and cool air over the water. This temperature structure results in a localized circulation pattern with low-level convergence and rising motion over the land and descending motion over the water. A sea breeze can exacerbate air pollution levels near the sea breeze's convergence zone (Boucouvala and Bornstein, 2003; Evytugina et al., 2006). Rising air can transport pollution out of the planetary boundary layer and into the free troposphere. Once in the free troposphere, pollutants have longer lifetimes and are able to be transported further downwind. Pollutants in the free troposphere are able to travel further distances before being deposited to the ground and are able to degrade air quality further downwind than pollutants that are not vented into the free troposphere. Since pollutants that reach the free troposphere have a longer lifetime than pollutants that stay in the PBL, pollutants in the free troposphere have a larger impact on climate.

Clouds have a large impact on atmospheric chemistry. Clouds influence the amount of solar radiation reaching near surface air, therefore affecting photochemistry. Clouds also play an important role in the sulfur cycle. Gas phase sulfur dioxide oxidation rates are slow, but sulfur dioxide can be quickly converted to sulfate aerosols in clouds. Sulfur dioxide can be oxidized rapidly through heterogeneous reactions in clouds when ozone is present and the pH is greater than 5 or when hydrogen peroxide is present over all pH values (Daum, 1990; Finlayson-Pitts and Pitts, 2000; Jacob et al., 1989). In the Mid-Atlantic in 2007, the pH of rainwater reported by the National Atmospheric Deposition Program/National Trends Network was around 4.5, so the quickest path of

sulfur dioxide to sulfate conversion in this region is in the presence of liquid water and hydrogen peroxide. Also, updrafts associated with clouds vent pollutants out of the planetary boundary layer (PBL) and into the free troposphere. Therefore, pollutants that are vented into the free troposphere through clouds have a larger impact on air quality further downwind and have a larger impact on climate than pollutants that stay in the PBL.

1.1.4 Urbanization impacts on weather, climate, and air pollution

There is a positive correlation between high air pollution and high temperature events (Weaver et al., 2009; Banta et al., 1998; Cheng and Byun, 2008; Jacob and Winner, 2009; Bloomer et al., 2009; Bloomer et al., 2010; Tai et al., 2010). Urbanization can increase temperatures locally creating an urban heat island (UHI) (Oke, 1987; Bornstein and Lin, 2000; Arnfield, 2003, Zhang et al., 2009; Landsberg, 1981). UHI effects can also propagate downwind to another city and amplify the downwind UHI (Zhang et al., 2009; Zhang et al., 2011). In addition to UHIs contributing to warmer temperatures which can result in higher concentrations of unhealthy air pollution, UHIs can amplify summertime heat waves that cause heat stress (Kunkel et al., 1996).

Planting trees in urban areas has a potential to dampen the urban heat island. The addition of trees will increase the amount of evaporative cooling in the urban area helping to cool near surface temperatures. Also, additional urban trees provide more shade cooling near surface air as well as ground and urban building wall surfaces. The change in temperature has a beneficial impact on reducing heat-related illnesses and air pollution. The addition of urban trees, however, adds more biogenic emissions of VOCs, which can react in the presence of nitrogen oxides to form ozone (Chameides et al., 1998). On the

other hand, the addition of trees increases the deposition of pollutants. Pollutants can be deposited on tree leaves. Cooling building wall surfaces increases buildings energy efficiency and reduces electrical demand. This results in a decrease in anthropogenic emissions from power plants and therefore has a beneficial impact on air quality and climate.

An UHI can influence the strength of a sea, lake, or bay breeze, which can affect air quality. For example, urbanization near an ocean can alter the temperature gradient along the coastline and therefore influence the strength of a sea breeze. Likewise, planting additional trees in a coastal city will dampen the UHI, alter the temperature gradient between land and sea, and therefore influence the strength of the sea breeze.

1.1.5 Roles of earth system models

Meteorological, air quality, and land surface models are important tools for studying the interactions among the land surface, air chemistry, and meteorology. They are used alongside observations to gain a better understanding of earth science. Models are also used to help understand how future changes to emissions, climate, or land surfaces will impact the earth system. Models are also used to help evaluate air pollution and climate change mitigation plans.

1.2 Objectives

This work investigates interactions among the atmosphere, land surface changes and atmospheric chemistry. Chapter 2 examines how current-generation meteorological and air quality models simulate two fine-scale meteorological processes and their impact on air chemistry and answers the following questions:

- How does model grid resolution influence fair-weather cumulus clouds and sulfur dioxide oxidation?
- How do differences in model cloud parameters affect sulfate concentrations?
- How does model grid resolution impact transport between the planetary boundary layer and the free troposphere?
- How does model grid resolution impact the simulation of the Chesapeake Bay breeze, the dispersion of pollutants, and ozone formation?
- What can be done to improve future model simulations?

Chapter 3 investigates how urban trees and building heights impact meteorology in and downwind of urban areas. The following questions are addressed:

- How do urban trees and building heights impact surface and air temperatures?
- How do trees in cities near a coastline impact a sea, bay, or lake breeze?

To accomplish this goal, an urban tree canopy parameterization is developed and implemented into a meteorological model. Chapter 4 explores the role of urban trees on air quality by answering the following questions:

- How do meteorological changes associated with planting trees in cities affect air quality?
- How do additional biogenic volatile organic compound emissions associated with planting urban trees influence air quality?

A summary and recommendations for future work are provided in Chapter 5.

Chapter 2: Impact of fair-weather cumulus clouds and the Chesapeake Bay breeze on pollutant transport and transformation

2.1 Introduction

Ozone and aerosols have health and climate implications. Ground-level ozone may cause permanent lung damage (Mudway and Kelly, 2000) and ground-level aerosols may produce heart and lung disease (Docker et al., 1993; Samet et al., 2000), and both tropospheric ozone and aerosols impact the radiative budget (Shine, 2000). The production of secondary pollutants, such as ozone and sulfate aerosols, depends on emissions, meteorological conditions, and the chemical composition of the atmosphere. Numerical Weather Prediction (NWP) and chemical models along with observations have been used to investigate how pollutants evolve in the atmosphere, to forecast air quality and climate impacts of pollutants, and to help evaluate air pollution and climate change mitigation plans.

Fine scale weather structures, such as fair-weather cumulus clouds and a sea breeze, influence air chemistry. Clouds play an important role in the sulfur cycle. While gas phase sulfur dioxide oxidation rates are slow, sulfur dioxide can be oxidized rapidly through heterogeneous reactions in clouds when ozone is present and the pH is greater than 5 or when hydrogen peroxide is present over all pH values (Daum, 1990; Finlayson-Pitts and Pitts, 2000; Jacob et al., 1989). For example, Eatough et al. (1984) studied the conversion of sulfur dioxide to sulfate aerosols in a power plant plume near the Pacific Ocean coast and found that on average 24-36% of the sulfur dioxide was oxidized in one hour in the presence of fog, but only 2-4% of the sulfur dioxide was oxidized when the

plume was not located in a cloud. The pH of rainwater reported by the National Atmospheric Deposition Program/National Trends Network in the Mid-Atlantic is around 4.5, so the quickest path of sulfur dioxide to sulfate conversion in the region is in the presence of liquid water and hydrogen peroxide.

Many atmospheric chemistry models have a high bias in sulfur dioxide and a low bias in cloud cover compared with observations. Hains (2007) found that sulfur dioxide column content has a 55% high bias in the Environmental Protection Agency's (EPA) Community Multiscale Air Quality (CMAQ) model when run at a 12 km horizontal resolution and a 50% high bias in the Georgia Tech / Goddard Global Ozone Chemistry Aerosol Radiation and Transport (GOCART) model when run at a 2° latitude by 2.5° longitude resolution. Hains (2007) suggested that the high biases are due to an underestimation of sulfate conversion in clouds. Mueller et al. (2006) noted that CMAQ has a low cloud bias and high sulfur dioxide bias and used two alternative cloud parameterizations to improve the simulation. In their study the alternative parameterizations improved the frequency of clear sky and overcast sky conditions but still underestimated the frequency of partly cloudy sky conditions. Sulfur dioxide and sulfate biases decreased with the alternative parameterizations as additional clouds increased the rate at which sulfur dioxide was converted to sulfate. A high bias of total sulfur in the planetary boundary layer (PBL) remained and Mueller et al. (2006) stated that CMAQ might underestimate the removal of pollutants from the PBL by convective venting. Increasing convective venting causes pollutants to have longer lifetimes and be transported greater distances exacerbating air pollution downwind. Previous studies showed air quality models underestimating inter-state transport of pollutants (e.g.,

Gilliland et al. (2008) and Godowitch et al. (2010) using CMAQ and Hogrefe (2000) using the Urban Airshed Model, Variable-Grid Version (UAM-V)).

On the other hand, Lee et al. (2011) showed that GEOS-CHEM, a global chemistry model, reproduced the column content of SO_2 measured by aircraft or satellite instruments implying that the short lifetime was captured. Yu et al. (2007) has shown that CMAQ simulations at 12 km horizontal resolution have good agreement with SO_2 aircraft observations in Ohio River Valley power plant plumes at ~1000 m altitude, but have a high bias below 700 m in the New York City and Boston urban plumes. Yu et al. (2007) suggested that this could be attributed to an overestimation of emissions from the New York City and Boston areas. It has also been shown that CMAQ simulations at 12 km horizontal resolution have a high SO_2 bias compared with ship observations off the coast of New England when the airflow is from the west and southwest (Yu et al., 2010). This high bias could be due to an overestimation of emissions in the Washington, DC, New York City, and Boston metropolitan areas (Yu et al., 2010) or to a too slow removal rate in the model.

Previous studies have shown that a sea breeze circulation can exacerbate air pollution levels. Evtyugina et al. (2006) showed that along the Portuguese west coast ozone levels are elevated when a sea breeze is present. Boucouvala and Bornstein (2003) found that peak ozone concentrations in southern California on high ozone days occur at the farthest inland location of a sea breeze's convergence zone. In Houston, high ozone episodes begin when the large-scale flow is offshore (Banta et al., 2005; Darby, 2005). As the bay breeze begins to develop stagnant conditions ensue allowing ozone and ozone

precursors to accumulate before being advected farther onshore as the bay breeze increases in intensity later in the afternoon (Banta et al., 2005; Darby, 2005).

With rapid increases in computing power in recent years, there have been a growing number of higher-resolution model simulations. The importance of increasing resolution in producing better-defined and more realistic mesoscale structures has been long recognized in the NWP community, since the horizontal resolution in operational models has been reduced from 300-400 km in middle 1950's to a few km today. In particular, many studies have shown benefits of using high-resolution NWP models to resolve frontal structures, orographic flows, and vertical circulations induced by surface inhomogeneities (see Mass et al., 2002 for review). Mass et al. (2002) explained that while it is difficult to prove that high-resolution simulations are more accurate due to the sparseness of observational sites, high-resolution simulations appear to produce more realistic weather structures.

High-resolution CMAQ modeling is also desirable for understanding the transport of air pollutants. Cohan et al. (2006) found that while air quality modeling at a horizontal resolution of 12 km is sufficient to determine regional-scale features of ozone changes to emissions reductions, finer resolution is necessary to capture localized variability. Jimenez et al. (2006) determined that a 2 km CMAQ simulation better simulates ozone concentrations in the presence of a sea-breeze than 4 and 8 km simulations. Weijers et al. (2004) found evidence that the spatial scale of aerosol variability is below 1 km in urban areas. Sokhi et al. (2006) showed that CMAQ run at a horizontal resolution of 1 km reproduces temporal fluctuations in ozone well, but like coarse model simulations underpredicts daily maximum ozone and overpredicts nighttime ozone concentrations.

Nevertheless, few numerical studies have been performed to examine the variability of air chemistry interacting with fair-weather cumulus clouds and sea-breeze circulations with horizontal resolutions below 1 km.

In the present study, the above issues are examined with state-of-the-art NWP and air quality models by pushing the horizontal resolution down to 0.5 km. The objectives of this study are to a) investigate how model resolution impacts the development of fair-weather cumulus clouds, the transport of pollutants through clouds, and sulfur dioxide to sulfate aerosol conversion in clouds in the model; and b) examine the effects of varying horizontal resolution on the development of the Chesapeake Bay breeze and the associated advection of air pollutants. These objectives are achieved by performing simulations with the Weather Research and Forecasting (WRF) model (Skamarock et al., 2008) coupled with the Urban Canopy model (UCM, Kusaka et al., 2001) and simulations with the CMAQ model (Byun and Schere, 2006) covering the Washington-Baltimore metropolitan areas from 1200 UTC 7 July to 1200 UTC 10 July 2007. This time period covers a period of fair-weather cumulus clouds (afternoon of 7 July), and one of the worst air pollution events of the decade (9 July) in which 8-h maximum ozone concentrations reached 114 ppbv downwind of Baltimore, MD near the Chesapeake Bay coastline in Edgewood, MD. Yegorova et al. (2011) analyzed this same air pollution event using the WRF model with online chemistry (WRF/chem) at 12 km resolution and observations. The air pollution event began with the passage of a cold front on 6 July 2007. Subsequently, an anticyclone developed and approached the Mid-Atlantic from the southeast and brought sunny, stagnant conditions to the region.

2.2 Model description

In this study, we use the Environmental Protection Agency's (EPA) Community Multiscale Air Quality (CMAQ) model, fed off-line by output from the Advanced Research WRF (WRF-ARW) model via the Meteorology-Chemistry Interface Processor (MCIP) (Otte and Pleim, 2010), to achieve the above-mentioned objectives.

2.2.1 Meteorological model and post-processing

The WRF model is coupled with the Noah land surface model and the single layer Urban Canopy Model (UCM). The Noah scheme produces soil moisture, soil temperature, skin temperature, canopy water content, and the energy flux and water flux terms in the surface energy balance and surface water balance (Chen and Dudhia, 2001). The UCM improves the parameterization of physical processes involved in the exchange of heat, momentum, and water vapor in urban environments by including shadowing from buildings, reflection of short and longwave radiation, wind profile information in the canopy layer and a multi-layer heat transfer equation for roof, wall and road surfaces (Kusaka and Kimura, 2004). Other physics options include a double-moment six-class microphysics scheme that calculates water vapor, cloud water, rain, cloud ice, snow, and graupel mixing ratio (Lim and Hong, 2010), the Mellor-Yamada-Janjic (MYJ) boundary layer parameterization (Janjic, 1994), and the Grell three-dimensional (3D) ensemble cumulus scheme, which expands on the Grell-Devenyi scheme (Grell and Devenyi, 2002) to allow subsidence in neighboring grid cells (Skamarock et al., 2008). The Grell 3D scheme is only used in the outermost domain.

Zhang et al. (2009) and Shou and Zhang (2010) used WRF-UCM simulations to show that upstream land use can exacerbate the urban heat island (UHI) effect. Herein,

the WRF-UCM is used with the same domain along with CMAQ to investigate the impact of model resolution on sulfur dioxide oxidation in fair-weather cumulus clouds, the Chesapeake Bay breeze, the dispersion of pollutants, and ozone formation. The model was run at 13.5, 4.5, 1.5, and 0.5 km horizontal resolution from 1200 UTC 7 July to 1200 UTC 10 July 2007 with dimensions of 181 × 151, 244 × 196, 280 × 247, and 349 × 349 grid cells, respectively (see Figure 2-1 for the model domains). All of the domains use 30 layers in the vertical with 20 layers in the lowest 2 km. The North American Regional Reanalysis is used for the model initial and outermost lateral boundary conditions. In the present study, Version 3.1.1 of the WRF model is used instead of Version 2.2.1, used by Zhang et al. (2009) and Shou and Zhang (2010). In order to examine the impact of varying model resolutions on the simulated air chemistry, one-way feedback is used instead of two-way feedback between the domains. Two-way feedback involves information being exchanged bi-directionally between the finer and coarser grids, whereas one-way feedback only involves information exchange from the coarse grid to the finer grid (Zhang et al., 1986).

A mass conservation problem was identified in the 0.5 km resolution domain of the WRF-UCM and CMAQ simulations. A mass balance analysis from a CMAQ simulation with chemistry turned off revealed a change in mass of chemical species that was inconsistent with model calculated sources, sinks, and fluxes. After analysis of the WRF-UCM output, we determined that the mass non-conservation was caused by waves reflecting off the top of the model domain. Fortunately, WRF-UCM includes damping options to minimize unrealistic reflections at the top of the model. WRF-UCM was re-run with gravity wave damping (Klemp et al., 2008) and vertical velocity damping

(Skamarock et al., 2008) with respective damping coefficients of 0.2 and 0.3. These changes minimize unrealistic reflections at the top of the modeling domain and loss in mass.

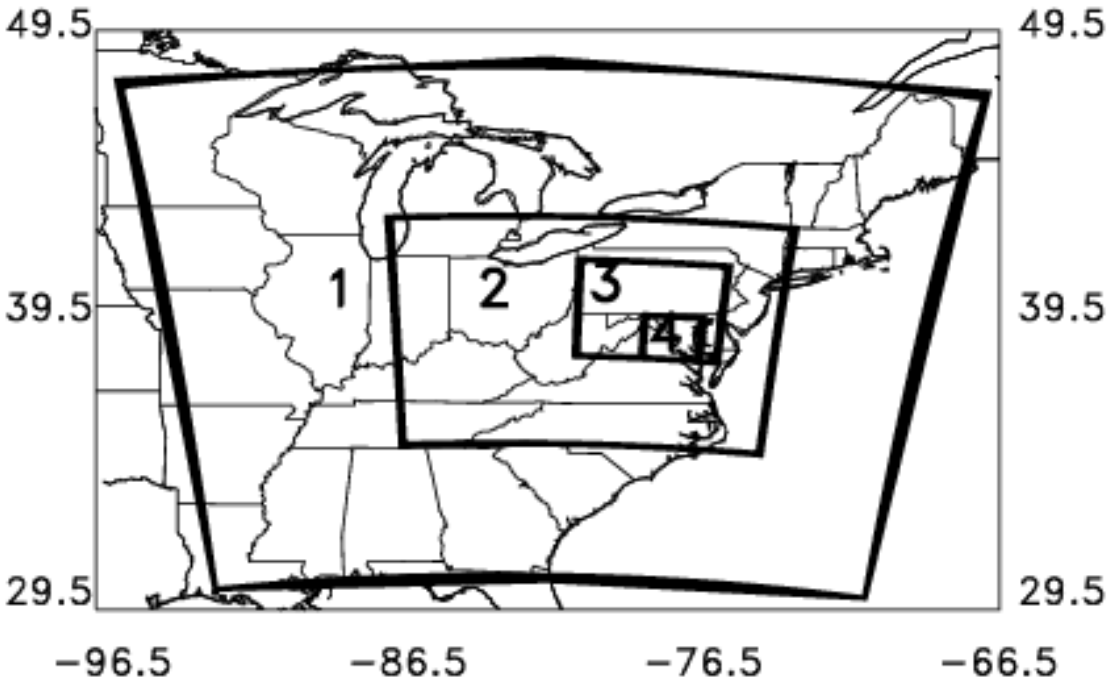

Figure 2-1: Location of modeling domains 1, 2, 3, and 4, with horizontal resolutions of 13.5, 4.5, 1.5, and 0.5 km, respectively.

Version 3.4 of MCIP was used to ingest the WRF-UCM outputs and create input files for processing emissions data and running air chemistry simulations. This step requires modifying MCIP to write out the percentage of each WRF-UCM grid cell that is urban. The urban fraction is used in CMAQ to calculate vertical diffusion. This model update is available beginning in Version 3.5_beta of MCIP.

2.2.2 Emissions

Emissions input files are created with the Sparse Matrix Operator Kernel Emissions (SMOKE) modeling system (Houyoux and Vukovich, 1999). Because a 2007

emissions inventory is not yet available, projected annual 2009 emissions from U.S. Regional Planning Organizations (RPOs) are processed with SMOKE to create hourly emissions input files for CMAQ. The annual 2009 projected emissions from the U.S. RPOs were grown from annual 2002 emissions and include estimated emissions changes due to growth and emissions controls expected to be implemented by 2009.

Area source emissions input to SMOKE are annual, countywide emissions, and are temporally and horizontally spatially distributed with SMOKE to create hourly gridded CMAQ emissions input files. Annual emissions are distributed based on the time of day, day of the week, and season based on temporal emissions distributions provided by the U.S. RPOs. Countywide area emissions are horizontally distributed based on gridded highly detailed landuse patterns from a spatial surrogate file. These landuse patterns are obtained from shapefiles that describe landuse from the 2000 census, National Land Cover Characteristics Data, and other spatial sources available from EPA's Emissions Modeling Clearinghouse. The shapefiles are input into the Multimedia Integrated Modeling System (MIMS) Spatial Allocator (Eyth and Brunk, 2005) to create a spatial surrogate file.

Point source emissions data are annual emissions for a specific location, and are temporally and spatially distributed in the vertical with SMOKE. Similar to the area emissions, the point source emissions are distributed based on temporal emissions distributions provided by the U.S. RPOs, except for power point sources, which are temporally distributed based on continuous emissions monitoring (CEM) observations. Also, point sources are vertically distributed based on temperature and velocity of the emissions, stack height, and meteorological conditions.

Mobile and biogenic emissions are also processed to create CMAQ emissions input files. Mobile emissions are created with MOBILE6 (U.S. Environmental Protection Agency, 2003) and biogenic emissions are processed with the Biogenic Emissions Inventory System (BEIS) Version 3.12 based on meteorology and land use (Vukovich and Pierce, 2002). MOBILE6 and BEIS are coupled with SMOKE.

2.2.3 Air quality model description

The EPA's CMAQ model Version 4.6 (Byun and Schere, 2006) is used to investigate the role of fair-weather cumulus clouds in the conversion of sulfur dioxide to sulfate aerosols and how the bay breeze influences the dispersion of pollutants and the formation of ozone. Here the model is run with the following user options: (1) a density based mass-conserving Piecewise Parabolic Method advection scheme (Colella and Woodward, 1984); (2) the Carbon Bond-05 gas-phase chemical mechanism (Yarwood et al., 2005); (3) the Asymmetric Convective Model Version 2 (Pleim, 2007) for vertical diffusion; and (4) a cloud module that uses the Regional Acid Deposition Model (Chang et al., 1987) to calculate the aqueous phase chemistry and the Asymmetric Convective Model (Pleim and Chang, 1992) to compute convective mixing. CMAQ is run with the same vertical resolution as the WRF-UCM simulations. Chemical initial and boundary conditions come from a Model for Ozone and Related chemical Tracers, Version 4 (MOZART-4) simulation (Emmons et al., 2010). Also, the 13.5 km resolution domain simulation begins 2 weeks prior to 1200 UTC 7 July 2007 to spin up the chemistry of the atmosphere for the species unavailable from global model output files used for chemical initial conditions.

Several model improvements are made to CMAQ based on Castellanos (2009), Castellanos et al. (2011), and Odman and Hu (2009). The non-urban minimum eddy diffusion coefficient used in CMAQ is reduced from 0.5 to 0.1 $m^2 s^{-1}$ to be consistent with micrometeorological observations and to improve model results (Castellanos, 2009; Castellanos et al., 2011). Also, the CO dry deposition velocity is reduced from 0.001 to 0.0 $m\ s^{-1}$, turning off CO dry deposition, which agrees better with observations (Castellanos, 2009). Bug fixes to the advection and horizontal diffusion schemes are implemented following Odman and Hu (2009). Finally, the CMAQ code is modified to output the flux of each species due to horizontal advection to adjacent grid cells.

CMAQ uses cloud properties to calculate photolysis rates and aqueous chemistry reactions. However, the representation of these cloud properties differ dramatically between the photolysis and aqueous chemistry schemes (Byun and Schere, 2006; Otte and Pleim, 2010). The cloud properties used in CMAQ's aqueous chemistry scheme consist of three-dimensional cloud water, rain, cloud ice, snow, and graupel mixing ratio from explicit clouds calculated in the WRF-UCM (Byun and Schere, 2006). When the horizontal resolution is coarser than 8 km, CMAQ adds parameterized clouds calculated in CMAQ's cloud module to the explicit clouds (Byun and Schere, 2006). The cloud properties used in CMAQ's photolysis scheme are two dimensional and consist of cloud top, cloud base, cloud fraction, and the total cloud water content averaged between the cloud top and cloud base (Otte and Pleim, 2010). These variables are diagnosed in MCIP using an algorithm based on a relative humidity (RH) threshold as described by Byun et al. (1999).

Differences in the representation of cloud properties between the photolysis and aqueous chemistry schemes are analyzed and simulations using the photolysis clouds in the aqueous chemistry scheme, hereafter referred to as MCIP clouds simulations, are performed to determine the sensitivity of sulfur dioxide and sulfate concentrations to the representation of cloud properties in the WRF-MCIP-CMAQ system. In order to perform the MCIP clouds simulations, MCIP is modified so that the input fields of the aqueous chemistry scheme use the same cloud properties as the photolysis cloud properties. Three-dimensional cloud fraction and total cloud water content are calculated in the same way as the photolysis scheme's two-dimensional cloud fraction and total water content but are not averaged in the vertical between the cloud base and cloud top. Total cloud water is then multiplied by the cloud fraction to obtain a new total cloud water content for use in CMAQ's aqueous chemistry scheme in the MCIP clouds simulations. The MCIP clouds simulations use the same graupel, ice, snow, and rain content as the base case, i.e., from the WRF model output. The graupel, ice, snow, and rain content are then subtracted from the new total cloud water content variable to obtain cloud liquid water content that is used in CMAQ. The 13.5 km MCIP clouds simulation is run with CMAQ calculated parameterized clouds turned off in the aqueous chemistry scheme as they are not needed since the MCIP RH-based clouds are calculated at all resolutions and includes parameterized clouds.

2.3 Results

This section evaluates how model simulations with different horizontal resolutions affect the development of fair-weather cumulus clouds, the transport of pollutants through clouds, and sulfur dioxide to sulfate aerosol conversion in clouds; and

then investigates the impact of varying horizontal resolution on the development of the Chesapeake Bay breezes and the associated advection of air pollutants.

2.3.1 Impact of fair-weather cumulus clouds

Fair-weather cumulus clouds, which play a role in converting sulfur dioxide to sulfate aerosols, developed during the afternoon of 7 July 2007. A Geostationary Operational Environmental Satellite (GOES) visible image at 2000 UTC is shown in Figure 2-2 and the average total cloud water content used in CMAQ's aqueous phase chemistry scheme from the 13.5 and 0.5 km resolution base and MCIP clouds simulations are compared in Figure 2-3. The cloud properties from the MCIP clouds simulations agree better with satellite observations, while the base case simulations underestimate the spatial coverage of clouds. The 13.5 km resolution simulation is unable to resolve small, fair-weather cumulus clouds, as expected, and tends to produce smooth cloud fields, e.g., as shown by a single cloud system in Figure 2-3a. RH maps from the 0.5 km resolution WRF simulation show many moist bubbles at 750 and 800 hPa (Figure 2-4), two levels where fair-weather cumulus clouds are found. In these regions of high RH, water vapor is close to condensing to form clouds. The large spatial differences between Figures 2-3c, 2-3d, 2-4a, and 2-4b show the sensitivity of model calculated fair-weather cumulus clouds to small variations in RH. These differences illustrate the difficulties involved in accurately diagnosing cloud properties in numerical models. The short spin-up time (8 hours) may also contribute to the biases in model cloud cover. It can be seen from Figure 2-5 that the MCIP clouds simulations have larger cloud fractions and average total cloud water content at all resolutions than in the base case. As the model resolution increases

in the base case, the cloud fraction over the innermost domain on 7 July and 9 July decreases, and the clouds that do form have lower total water content (Figure 2-5).

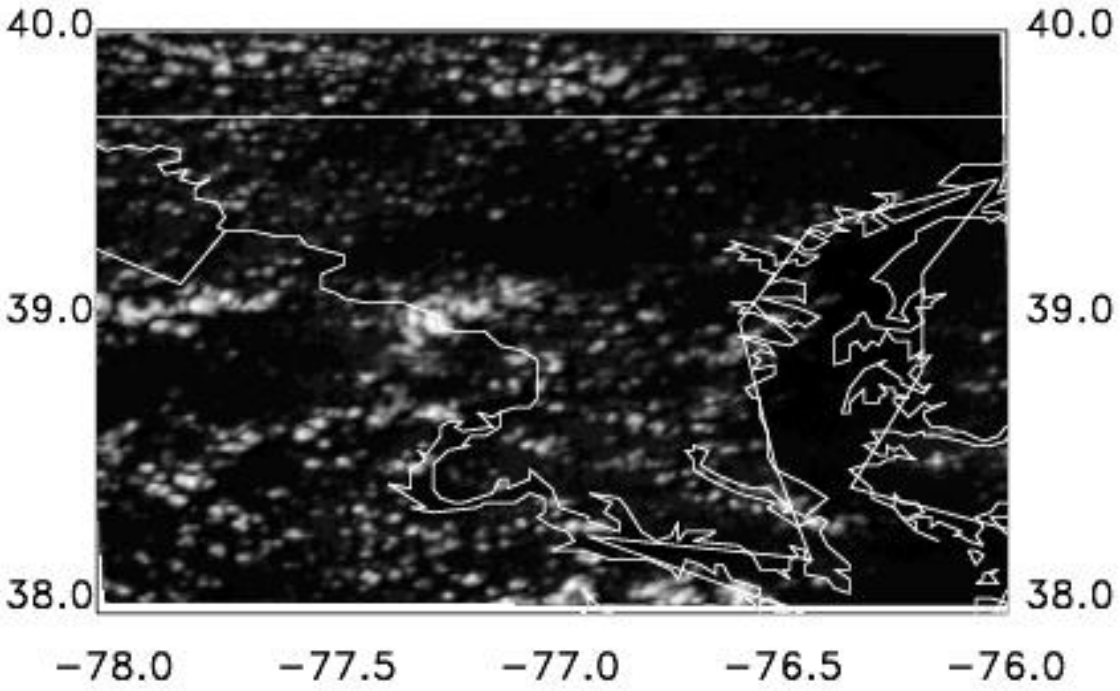

Figure 2-2: GOES Visible satellite image at 2000 UTC 7 July 2007. White regions show locations of fair-weather cumulus clouds in the region. The white lines depict state borders and coastlines.

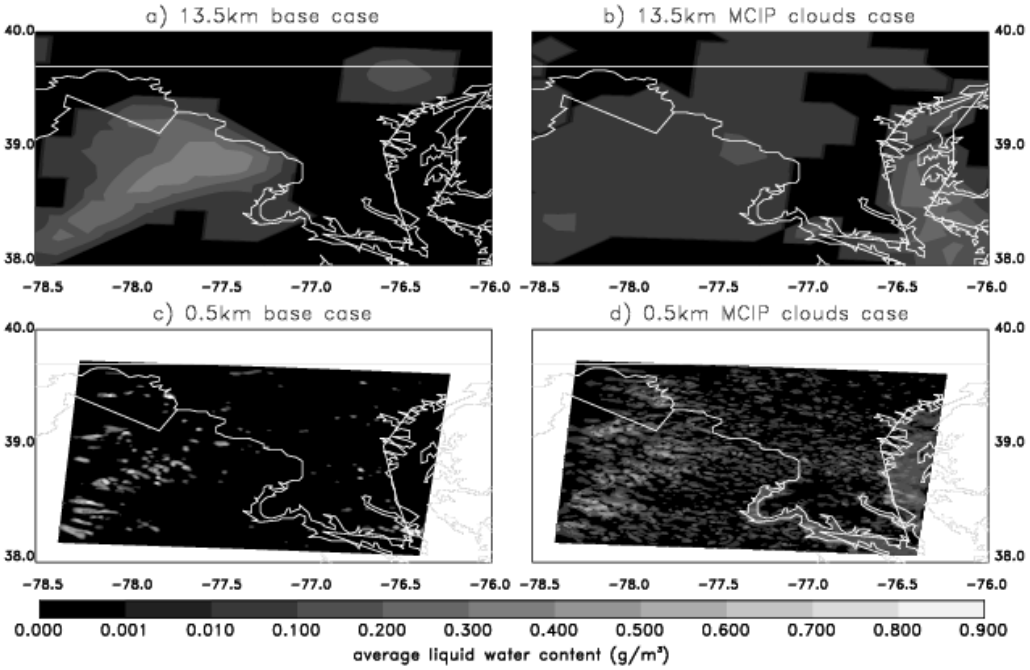

Figure 2-3: Cloud average liquid water content (g/m^3) used in CMAQ's aqueous chemistry scheme for the a) 13.5 km base case, b) 13.5 km MCIP clouds case, c) 0.5 km base case, and d) 0.5 km MCIP clouds case at 2000 UTC 7 July 2007. The white lines depict state borders and coastlines. The high resolution MCIP clouds most nearly resemble observations (Figure 2-2).

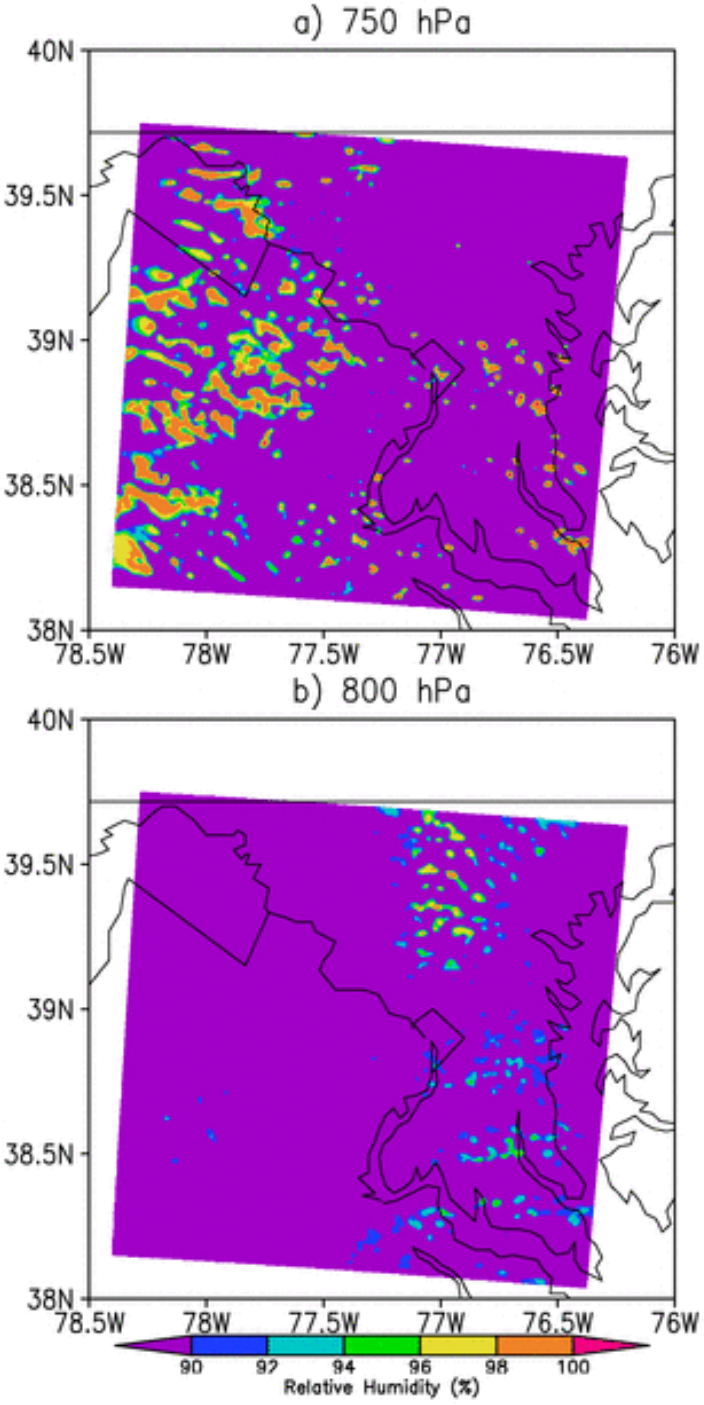

Figure 2-4: Relative humidity (%) for the 0.5 km horizontal resolution simulation at 2000 UTC 7 July 2007 at a) 750 hPa and b) 800 hPa.

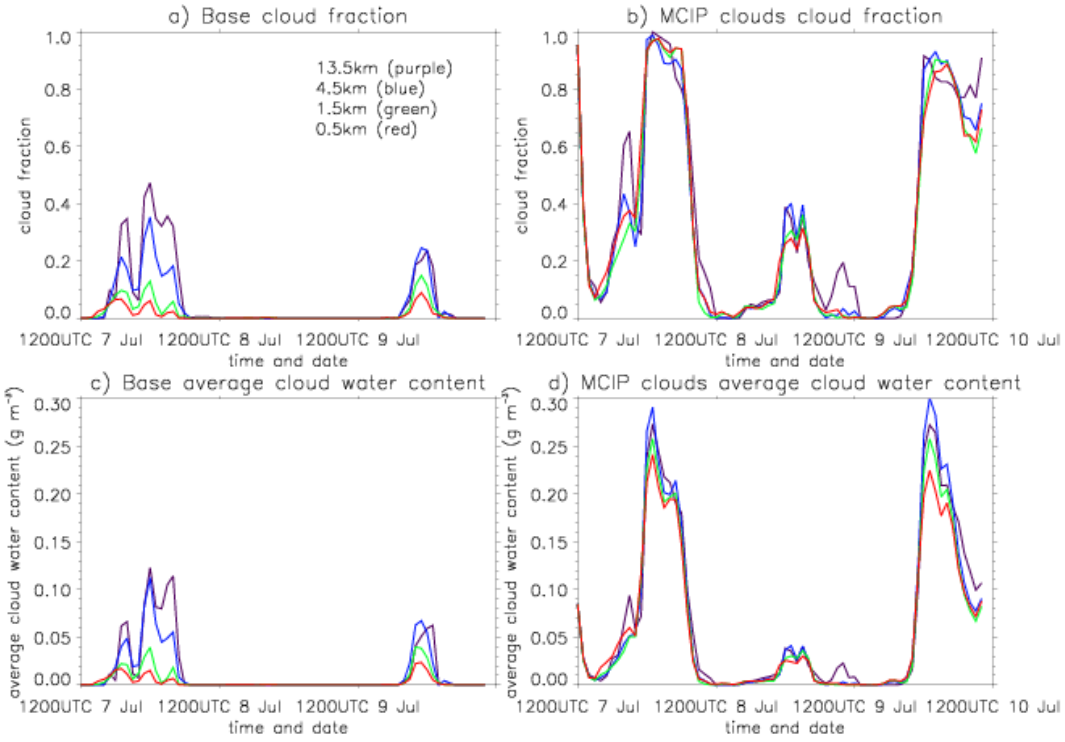

Figure 2-5: Time-series of model cloud fraction for the a) base case and b) MCIP clouds case and average cloud liquid water content (g/m^3) for the c) base case and d) MCIP clouds case for the 13.5, 4.5, 1.5, and 0.5 km horizontal resolution simulations averaged over the 0.5 km domain from 1200 UTC 7 July to 1200 UTC 10 July 2007.

The simulated sulfur dioxide is compared to surface measurements from the EPA's Air Quality System (AQS) at two locations. The observed 24-h average sulfur dioxide concentrations from 1200 UTC 7 July to 1200 UTC 8 July at Beltsville, MD (39.06°N, 76.88°W) and Essex, MD (39.31°N, 76.47°W) are 2.01 and 2.45 ppbv, respectively. The model ground-level sulfur dioxide and sulfate aerosol concentrations for the base and MCIP clouds cases are shown in Table 2-1 for Beltsville and Table 2-2 for Essex. The CMAQ simulations have a high bias in sulfur dioxide at the measurement sites at all resolutions at both sites and for both the base and MCIP clouds cases. The higher resolution simulations have larger median SO_2 concentrations than the 13.5 km

simulations around Essex because the higher resolution runs simulate stagnation downwind of emissions sources southeast of Essex causing pollution to accumulate. Observed median and 10^{th} and 90^{th} percentile sulfur dioxide concentrations for the month of July 2007 were 1.1, 0.2, and 4.2 ppbv, respectively at Beltsville and 3, 1, and 9 ppbv, respectively at Essex. It can be seen from Tables 2-1 and 2-2 that mean sulfur dioxide concentrations in the MCIP clouds simulations are slightly lower (1-6%) and sulfate concentrations are higher (7-20%) than the base case simulated sulfur dioxide and sulfate. More clouds in the MCIP clouds case cause more sulfur dioxide to be converted to sulfate aerosols. Since the PBL is well mixed, many sulfate aerosols formed in clouds aloft are transported downward to the surface.

	Base SO_2 (ppbv)	MCIP Clouds SO_2 (ppbv)	Base SO_4 ($\mu g/m^3$)	MCIP Clouds SO_4 ($\mu g/m^3$)
13.5km	3.32, 3.85, 7.96	3.16, 3.69, 7.77	4.73, 5.62, 6.22	5.70, 6.17, 7.16
4.5km	2.66, 3.40, 4.27	2.62, 3.35 4.19	4.05, 5.29, 5.99	4.60, 4.60, 6.20
1.5km	2.60, 4.16, 5.30	2.55, 4.06, 5.21	4.12, 5.36, 5.86	4.57, 5.95, 6.39
0.5km	3.17, 3.97, 4.63	2.95, 3.72, 4.36	4.59, 5.49, 5.94	5.59, 6.58, 7.12

Table 2-1: 10^{th} percentile, median, and 90^{th} percentile 24-h average sulfur dioxide (ppbv) and sulfate ($\mu g/m^3$) concentrations at Beltsville, MD from 1200 UTC 7 July to 1200 UTC 8 July for the 13.5, 4.5, 1.5, and 0.5 km Base and MCIP Clouds simulations. Values reflect variability in space for a 1,640.25 km^2 region surrounding the measurement site, which represents the area of 9 grid cells for the 13.5 km simulation. The observed 24-h average SO_2 concentration at Beltsville, MD was 2.01 ppbv.

	Base SO_2 (ppbv)	MCIP Clouds SO_2 (ppbv)	Base SO_4 ($\mu g/m^3$)	MCIP Clouds SO_4 ($\mu g/m^3$)
13.5km	4.02, 4.91, 6.48	3.85, 4.80, 6.33	4.94, 5.85, 6.14	5.84, 6.42, 6.94
4.5km	4.00, 7.32, 10.64	3.88, 7.18, 10.52	5.06, 6.56, 7.75	5.75, 7.23, 8.33
1.5km	3.53, 5.53, 12.94	3.38, 5.36, 12.83	4.93, 5.66, 7.57	5.72, 6.45, 8.34
0.5km	3.63, 4.99, 13.58	3.40, 4.78, 13.44	4.99, 5.69, 7.51	6.11, 6.75, 8.36

Table 2-2: 10^{th} percentile, median, and 90^{th} percentile 24-h average sulfur dioxide (ppbv) and sulfate ($\mu g/m^3$) concentrations at Essex, MD from 1200 UTC 7 July to 1200 UTC 8 July for the 13.5, 4.5, 1.5, and 0.5 km Base and MCIP Clouds simulations. Values reflect variability in space for a 1,640.25 km^2 region surrounding the measurement site, which represents the area of 9 grid cells for the 13.5 km simulation. The observed 24-h average SO_2 concentration at Essex, MD was 2.45 ppbv.

Figure 2-6 displays west-east cross sections of sulfate aerosols averaged over the north-south direction covering the innermost domain at 2000 UTC 7 July when fair-weather cumulus clouds are present in the 13.5 and 0.5 km resolution base and MCIP clouds simulations. It can be seen that more sulfate aerosols are present in the 0.5 km simulation. Even though the cloud fraction is lower and the liquid water content of clouds that do form is lower in the 0.5 km base case simulation than in the 13.5 km base case simulation, more sulfur dioxide is being converted to sulfate aerosols in the 0.5 km resolution simulation. Apparently, higher resolution simulations cause more sulfur dioxide to be transported vertically into the clouds where it is converted to sulfate aerosols, and as expected, updrafts occur preferentially under clouds. Updraft speeds also increase as the resolution increases. At 2000 UTC 7 July the 4.5, 1.5, and 0.5 km resolution base case simulations averaged over the innermost domain have mass fluxes at 910 hPa that are 1.8, 7.5, and 20.3 times larger than the 13.5 km base case mass flux; these updraft calculations include vertical advection but not vertical diffusion. As expected, the SO_2 to sulfate conversion rates are also sensitive to cloud amount. Sulfate aerosols change noticeably between the MCIP clouds and base cases. More sulfate aerosols are present in the MCIP clouds case simulations due to the presence of more clouds (Figure 2-6).

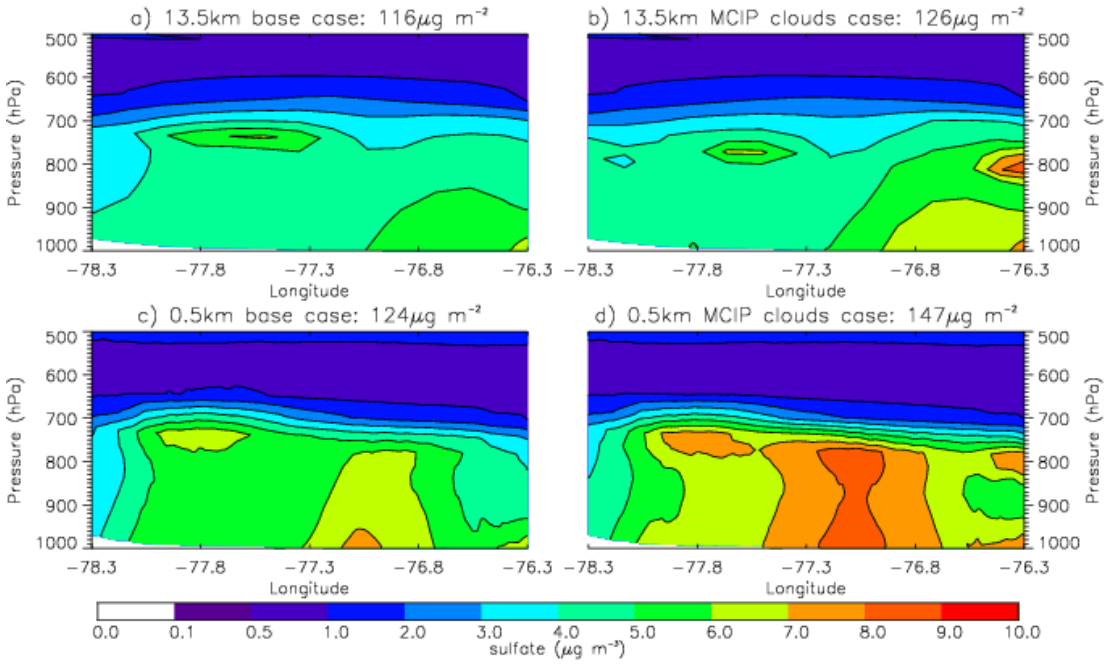

Figure 2-6: West-east cross-section of sulfate aerosols (μg/m^3) averaged over the north-south direction covering the area of the 0.5 km domain for the a) 13.5 km base case, b) 13.5 km MCIP clouds case, c) 0.5 km base case, and d) 0.5 km MCIP clouds case at 2000 UTC 7 July 2007. Fair-weather cumulus clouds are present at this time. The surface to 500 hPa sulfate column averaged over the innermost domain is shown above each figure.

Sixteen hours later (i.e., at 1200 UTC 8 July), there is noticeably less sulfur dioxide present at higher resolutions (Figure 2-7). Specifically, the surface to 215 hPa sulfur dioxide columns at 1200 UTC 8 July, averaged over the innermost domain for the 4.5, 1.5 and 0.5 km resolution base case simulations are 14, 21, and 23% smaller than that from the 13.5 km resolution base case simulation (Figure 2-7). However, differences in the amount of sulfate aerosols between the base and MCIP clouds simulations are small. The base case sulfate column of the 4.5 km simulation is 3% larger than in the 13.5 km simulation, while the 1.5 and 0.5 km simulations' sulfate columns are 4% smaller.

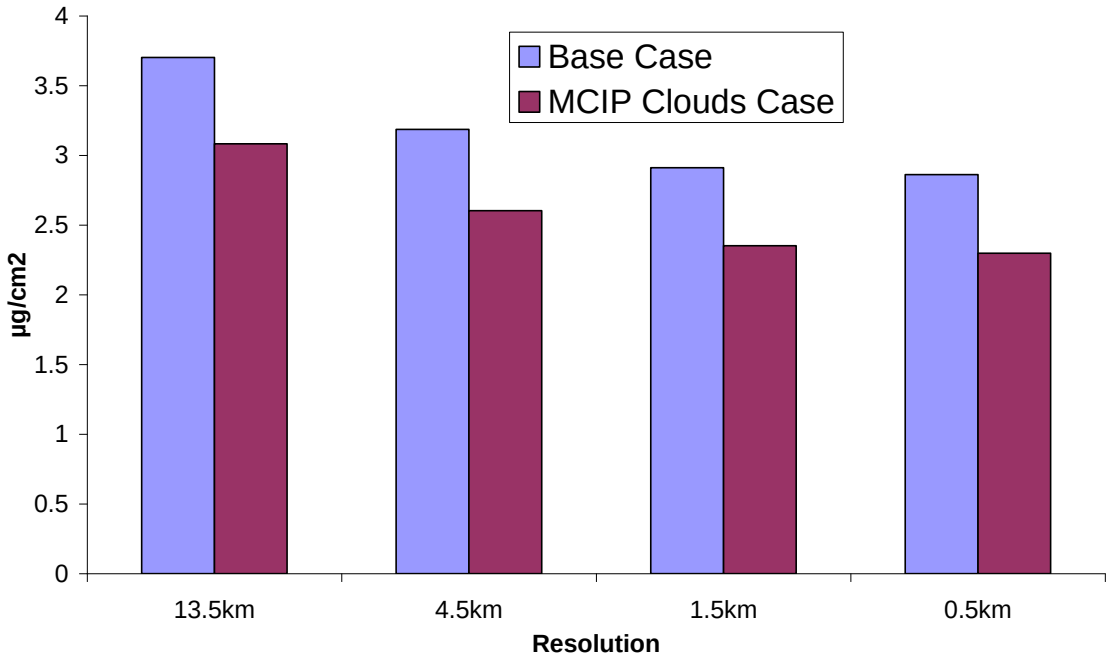

Figure 2-7: Surface to 215-hPa SO_2 column (µg/cm^2) at 1200 UTC 8 July 2007 averaged over the innermost domain for the base and MCIP clouds case simulations at 13.5, 4.5, 1.5, and 0.5 km horizontal resolutions. The smaller column content should bring CMAQ into better agreement with observations (Hains 2009; Lee et al., 2011).

The net flux of total sulfur (sulfur dioxide, sulfate aerosols, and sulfuric acid) integrated over the vertical extent of the model into and out of the area of the innermost domain for each simulation will now be analyzed to examine why the column content sulfur dioxide decreases as the horizontal resolution increases. While all of the CMAQ simulations have a net flux of total sulfur out of the area during the first 24 h of simulations, due partly to sulfur from emissions in the innermost domain being transported out of the domain, the magnitude of the net outward flux increases as the resolution increases. When integrating over the depth of the model the 4.5, 1.5, and 0.5 km resolution simulations have 52, 68, and 70% more sulfur leaving the area than the 13.5 km resolution.

There is a net import of sulfur in the PBL and a net export in the free troposphere. As the model resolution increases, more sulfur is transported aloft and vented out of the PBL to the free troposphere where winds are stronger causing the pollutants to be transported downwind more quickly. Figure 2-7 shows that as the resolution increases, sulfur dioxide integrated from the surface to 215 hPa within the innermost domain decreases due to more sulfur dioxide being converted to sulfate aerosols and more being transported out of the area of the innermost domain. Also, the MCIP clouds simulations have less column integrated sulfur dioxide than the base case simulations due to the presence of more clouds, which causes more sulfur dioxide to be oxidized to form sulfate aerosols. Uncertainties in vertical transport through clouds are difficult to quantify. Conversion of sulfur dioxide to sulfate is faster in clouds than clear skies (Daum, 1990; Finlayson-Pitts and Pitts, 2000; Jacob et al., 1989; Eatough et al., 1984). Therefore, it is expected that sulfate concentrations increase as cloud cover and transport through clouds increases.

2.3.2 Impact of the Chesapeake Bay breezes

Coarser resolution model simulations are unable to capture large abrupt changes in surface characteristics, such as land-water boundaries of fronts. In the early morning of 9 July 2007, the synoptic-scale winds were westerly. By mid-morning (i.e., at 1400 UTC or 0900 EST), stagnation is present in the northern Chesapeake Bay (downwind of Baltimore, MD) in the 4.5, 1.5, and 0.5 km resolution simulations (Figure 2-8) as a result of the wind direction changing from a westerly to southeasterly direction as the bay breeze sets up (Figure 2-9). This stagnation allows ozone and ozone precursors to accumulate east of Baltimore and Washington, DC over the bay. The 13.5 km resolution

simulation, however, does not generate stagnation over the bay and produces a weaker bay breeze that starts later due to a smaller temperature gradient along the coastline. Instead, the winds over the northern Chesapeake Bay in the 13.5 km resolution simulation shift from a westerly to southwesterly direction by mid-morning. By mid-afternoon, the winds at all resolutions shift to a southerly direction. At 1900 UTC, it can be seen that as the resolution increases, the bay breeze increases in strength, and its convergence zone pushes farther inland (Figure 2-9). The area of land grid boxes with easterly winds at 1900 UTC near the surface between 76.5-76.25°W and 38.5-39.5°N for the 13.5, 4.5, 1.5, and 0.5 km resolution domains are 182, 851, 1040, and 1087 km^2, respectively.

Air quality was poor on 9 July 2007, and mean ozone concentrations from all of the CMAQ simulations agree well with EPA's AQS observations at 30 sites in the innermost domain (see Figure 2-10). The 8-h maximum ozone concentrations for the 13.5 and 4.5 km resolution simulations have mean low biases of 1.9 and 1.3 ppbv, respectively, whereas the 1.5 and 0.5 km simulations have mean high biases of 0.56 and 1.0 ppbv, respectively. A notable improvement in the centered root mean squared error is obtained as the resolution increases from 13.5 to 4.5 km. The centered root mean squared error of the 8-h maximum ozone is 9.60, 6.92, 6.77, and 6.92 ppbv for the 13.5, 4.5, 1.5, and 0.5 km simulations, respectively.

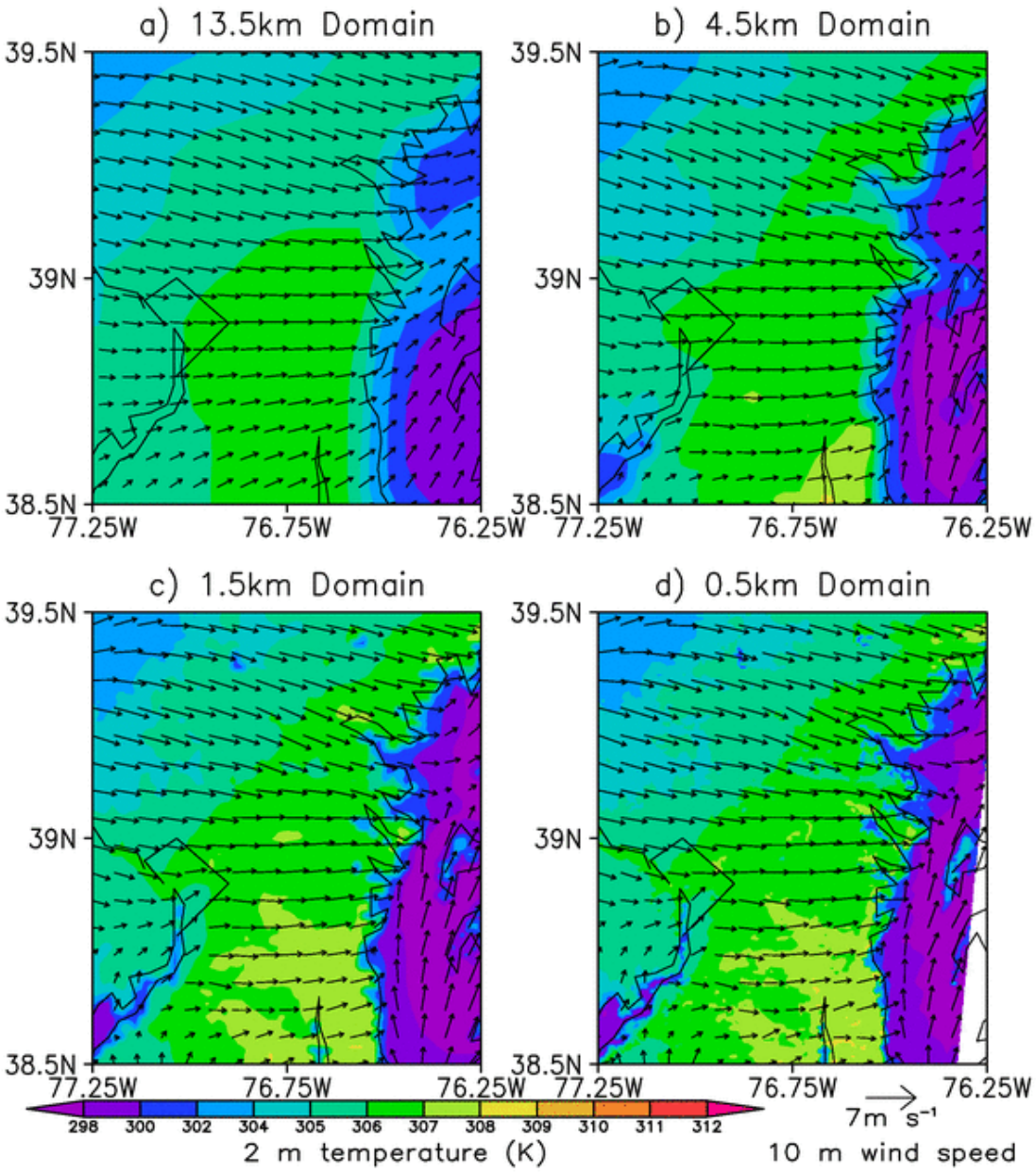

Figure 2-8: 2-m temperature (K) and 10-m wind speeds for the a) 13.5, b) 4.5, c) 1.5, and d) 0.5 km horizontal resolution simulations at 1400 UTC (0900 EST) 9 July 2007.

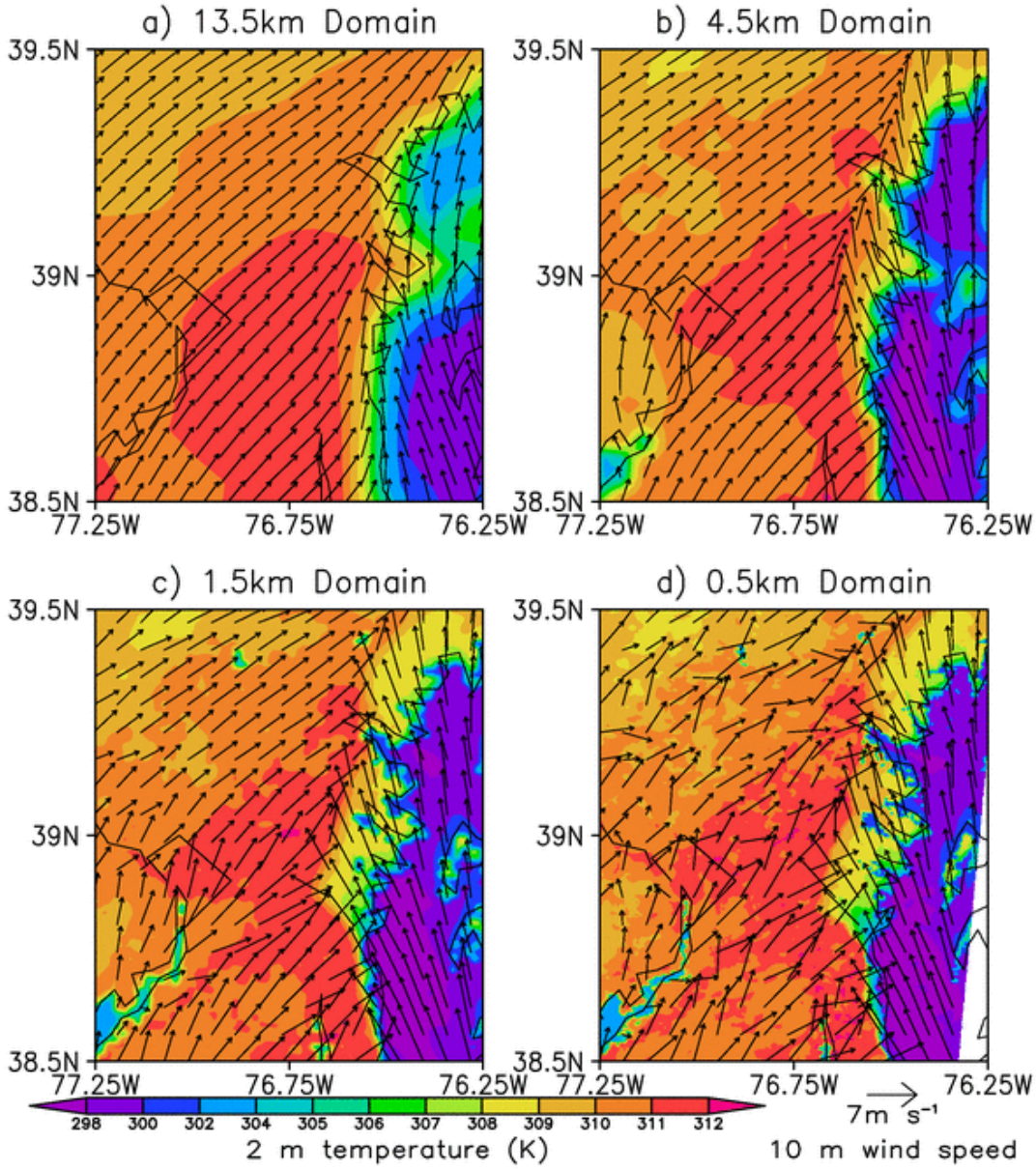

Figure 2-9: 2-m temperature (K) and 10-m wind speeds for the a) 13.5, b) 4.5, c) 1.5, and d) 0.5 km horizontal resolution simulations at 1900 UTC (1400 EST) 9 July 2007.

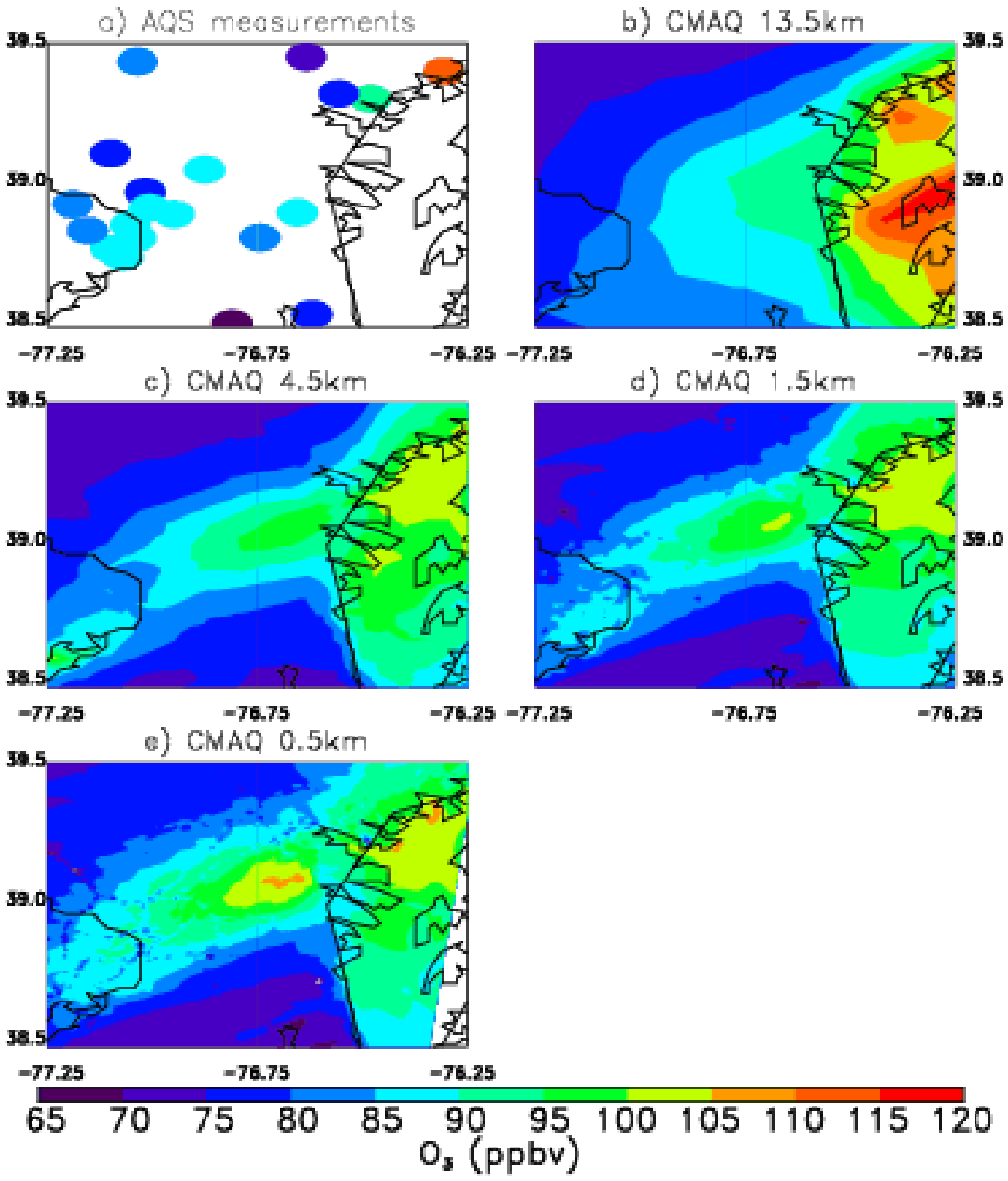

Figure 2-10: 8-h maximum ozone concentrations (ppbv) from a) EPA's Air Quality System (AQS) observations and the b) 13.5, c) 4.5, d) 1.5, and e) 0.5 km horizontal resolution simulations at the lowest model level on 9 July 2007. The black lines depict state borders and coastlines.

The highest 8-h maximum ozone measured on 9 July in the innermost domain occurred at Edgewood, MD (39.4°N, 76.3°W), the northeastern-most measurement point depicted in Figure 2-10a located on the northern coast of the Chesapeake Bay. Its value

was 114 ppbv while the model simulates 8-h maximum concentrations of 75, 91, 92, and 96 ppbv at 13.5, 4.5, 1.5, and 0.5 km resolution, respectively. The low bias may be partially due to a low bias in emissions. Projected 2009 emissions used, which may contain emissions controls, or emissions reductions, which had not been implemented by July 2007. A time series of ozone observations and model results at Edgewood shows that the model has a low bias during the day on 9 July at all resolutions with the 13.5 km resolution simulation performing the worst (Figure 2-11). The high bias at night may be attributed to the dry deposition velocity of pollutants being too slow in CMAQ. Y. Choi (personal communication) found that adjusting the aerodynamic resistance with improved forest canopy heights increases dry deposition velocity and brings CMAQ into better agreement with observations in the Northeastern US. While the increased ozone dry deposition velocities improved CMAQ simulated ozone in the Southeastern US, a high bias still remained (Y. Choi, personal communication). The high bias in the southeast corresponded with a high bias in formaldehyde and more NO_x sensitive regions than observations reveal, which may be due to a high bias in biogenic emissions (Y. Choi, personal communication). The 4.5, 1.5, and 0.5 km resolution simulations come into better agreement with the observations at Edgewood on 9 July because they simulate mid-morning stagnation over the northern Chesapeake Bay causing pollutants to accumulate, a late-morning bay breeze causing pollutants to converge over Edgewood, and afternoon advection by southerly winds causing additional ozone that had built up over the bay to be transported to Edgewood (Figure 2-12). The 13.5 km resolution simulation does not produce a bay breeze convergence zone over Edgewood.

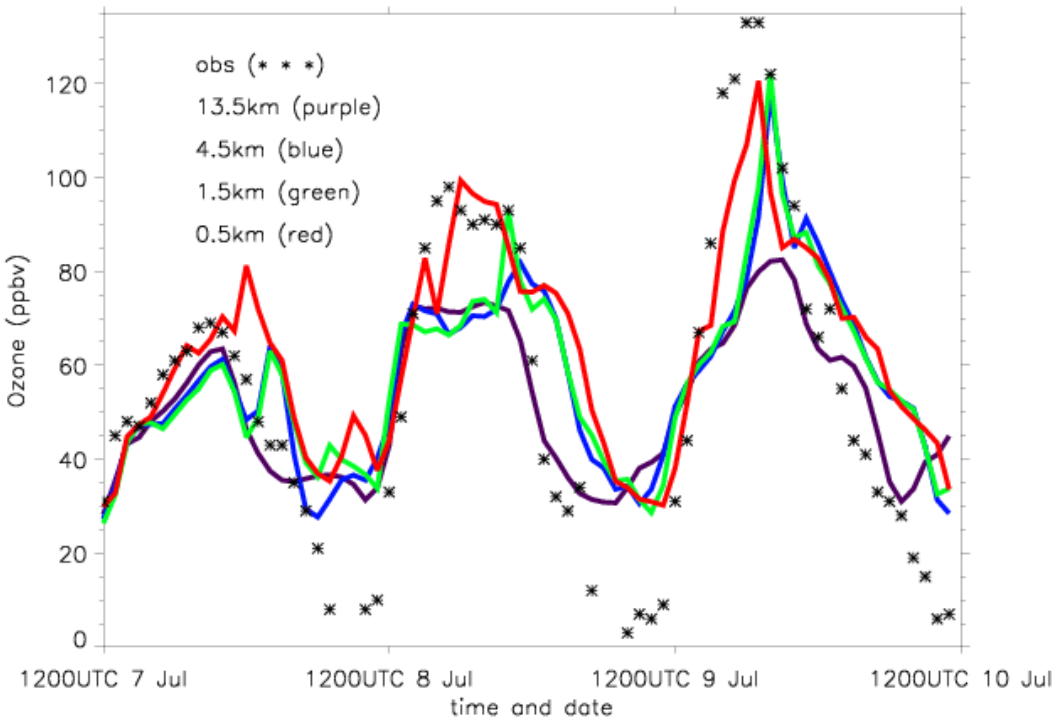

Figure 2-11: Ozone (ppbv) time-series at Edgewood, MD from AQS measurements and the 13.5, 4.5, 1.5, and 0.5 km resolution simulations at the lowest model level from 1200 UTC 7 July to 1200 UTC 10 July 2007.

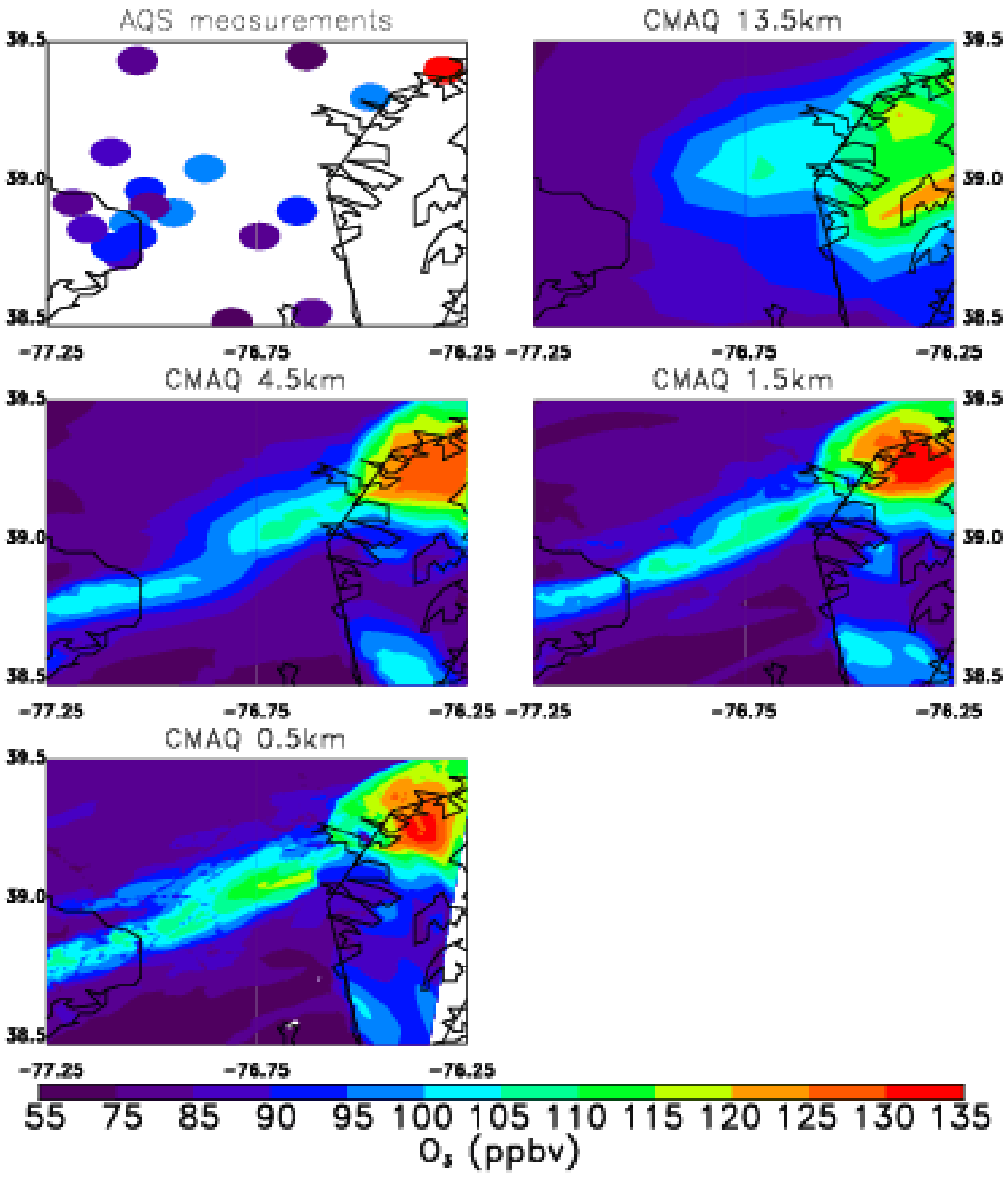

Figure 2-12: Ozone concentrations (ppbv) from a) AQS observations and the b) 13.5, c) 4.5, d) 1.5, and e) 0.5 km horizontal resolution simulations at the lowest model level at 1900 UTC 9 July 2007. The black lines depict state borders and coastlines.

The 13.5 km CMAQ simulation has higher 8-h maximum ozone concentrations near the surface over the Chesapeake Bay than over land (Figure 2-10) even though less stagnation is present over the bay during the morning in the 13.5 km resolution

simulation (Figure 2-8). The early morning stagnation seen in the higher resolution runs causes localized high concentrations over the bay. However, concentrations decrease later in the day as the bay breeze transports the pollutants northward and as it limits the west to east transport across the coastline. Since the simulated bay breeze is weaker at 13.5 km, more pollutants flow near the surface over the bay where the PBL is shallow over the cool water surface. In addition, it appears that more pollutants are directly emitted over the bay in coarser resolution simulations due to the failure to properly resolve the coastline. Emissions in a grid cell that straddle the coastline can appear to be emitted over the water, but in reality they are emitted over land. Figure 2-13 depicts a west-east cross section of CO for the 13.5, 4.5, 1.5, and 0.5 km resolution base case simulations at 1900 UTC 9 July, in which the coastline is located at 76.42°W. The cross section is located at 39.1°N, which includes the area of high ground-level ozone concentrations between Washington, DC and Baltimore, MD in the 0.5 km resolution simulation. One can see that the 0.5 km resolution model run simulates a stronger bay breeze that inhibits pollutants from being transported eastward over the water near the surface. Instead, pollutants are lofted and then transported eastward. The higher resolution simulations shows a local maximum in CO mixing ratio near the top of the PBL, as has been observed for CO and O_3 in this area (Castellanos et al., 2011; Taubman et al., 2006). Profiles of CO and O_3 near the coastline in the 0.5 km resolution simulation reveal concentration peaks at the surface and aloft (Figure 2-14). The peaks at ground level are from local sources while the peaks aloft are from pollutants being transported into the bay breeze convergence zone where they are lofted and then transported eastward.

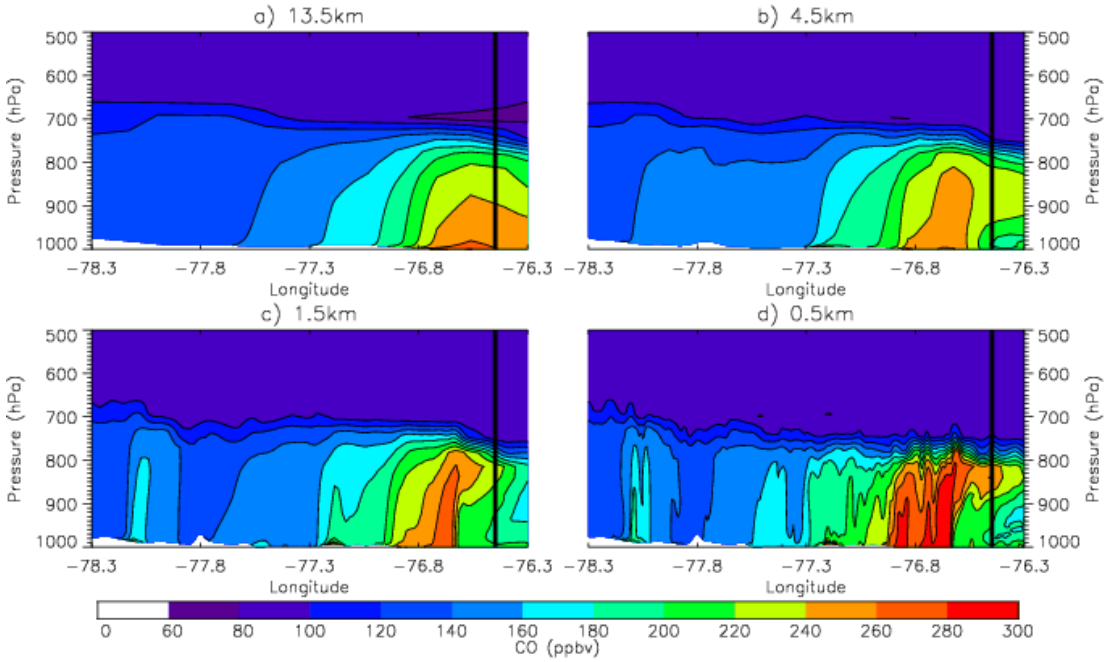

Figure 2-13: West-east cross-section of carbon monoxide (ppbv) passing between Washington, DC and Baltimore, MD at 39.1° latitude for the a) 13.5, b) 4.5, c) 1.5, and d) 0.5 km domains at 1900 UTC 9 July 2007. The coastline of the Chesapeake Bay is located at -76.42° longitude and is marked with a vertical black line. The local maximum in CO mixing ratio produced near the top of the boundary layer has been observed in aircraft profiles (Castellanos et al., 2011; Taubman et al., 2006).

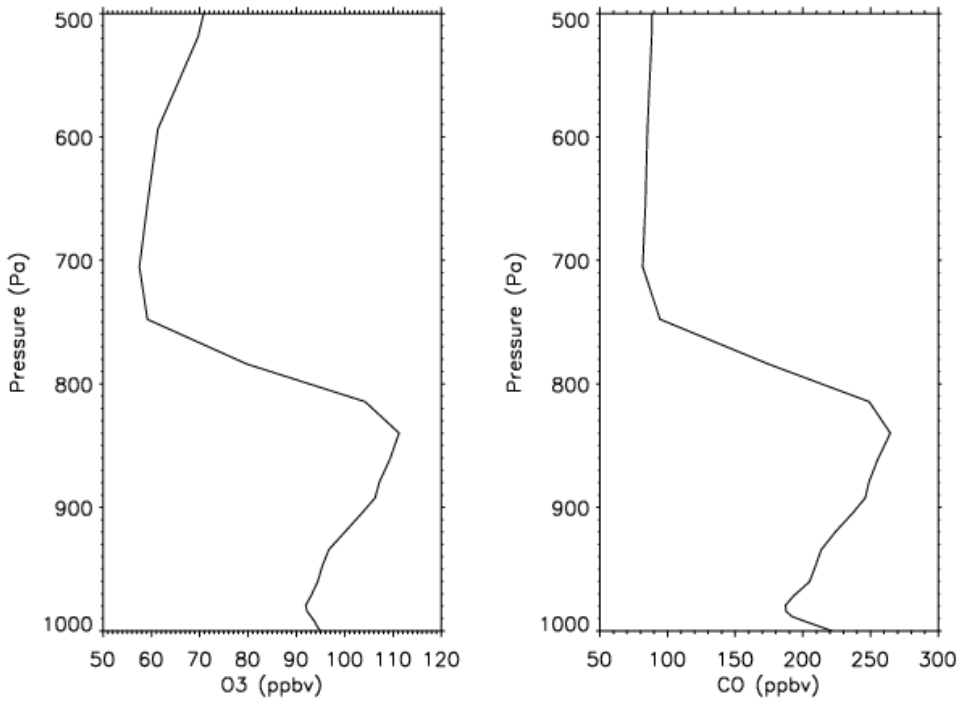

Figure 2-14: Profiles of ozone and carbon monoxide (ppbv) at the coastline of the western shore of the Chesapeake Bay at 39.1° latitude -76.4° longitude for the 0.5 km domains at 1900 UTC 9 July 2007.

The lofting associated with the bay breeze causes lower pollutant concentrations near the surface over the water in the higher resolution simulations (Figure 2-10). The simulated maximum 8-h surface ozone concentrations over the Chesapeake Bay on 9 July are 116, 105, 105, and 106 ppbv for the 13.5, 4.5, 1.5, and 0.5 km resolution simulations, respectively.

Even though the bay breeze increases in strength with increasing resolution, the bay breezes in the 4.5 and 1.5 km resolution simulations are strong enough to prevent pollutants emitted over land in the afternoon from being transported over the water near the surface similar to the 0.5 km resolution simulation. This results in similar maximum 8-h ozone concentrations over the water. The mean 8-h maximum ozone concentrations

over land between 77.25-76.25°N and 38.5-39.5°N are 83.7, 82.4, 82.4, and 84.1 ppbv, and the mean 8-h maximum ozone concentrations over water with the same boundaries are 105.0, 96.4, 94.0, and 94.2 ppbv for the 13.5, 4.5, 1.5, and 0.5 km resolution domains, respectively. As the resolution increases, 8-h maximum ozone concentrations increases near the bay-breeze convergence zone and decrease over the entire Chesapeake Bay.

2.4 Discussion

In previous studies, CMAQ has shown a weakness in modeling partly cloudy sky conditions (Mueller et al., 2006) and the sulfur budget (Hains, 2007; Mueller et al., 2006). This work shows these problems can be improved by using diagnosed clouds that agree with observations and by increasing the model resolution. CMAQ's aqueous chemistry scheme and photolysis scheme generate dramatically different cloud cover. These cloud properties need to be harmonized. For this particular case the photolysis scheme's clouds agree better with observations than the aqueous chemistry scheme's clouds. Simulations using the photolysis scheme's clouds in the aqueous chemistry scheme result in more sulfur dioxide oxidizing to form sulfate aerosols due to more clouds present.

As resolution increases, more vigorous convective vertical mixing occurs in the PBL and between the PBL and free troposphere. Faster vertical mixing in the presence of fair-weather cumulus clouds results in more sulfur dioxide transport into clouds and more sulfate formation. More transport across the PBL to the free troposphere allows pollutants to have a longer lifetime and travel further downwind. The longer trace gases and aerosols remain in the atmosphere, the larger the radiative, microphysical, and climate impacts. Also, an increase in pollutant transport exacerbates air pollution

downwind.

The bay breeze increases in strength as the resolution increases. The 13.5 km resolution simulation does not capture the bay breeze and allows ground level pollutants to cross the coastline. This causes larger 8-h maximum ozone concentrations over the water and lower concentrations inland near the bay breeze convergence zone seen in finer resolution simulations and in observations. Even though ozone concentrations differ near the bay breeze convergence zone in the 4.5, 1.5, and 0.5 km simulations, a comparison of error statistics between model simulations and observations indicates that running CMAQ at a horizontal resolution of 4.5 km is sufficient for modeling ground level ozone in the vicinity of the Chesapeake Bay. However, it should be noted that the 8-h maximum ozone concentrations near the convergence zone of the bay breeze on the western shore of the Chesapeake Bay, which is not co-located with an observational site, are sensitive to resolution equaling 93, 98, 101, and 107 ppbv for the 13.5, 4.5, 1.5, and 0.5 km simulations, respectively. Due to the sparseness of observational sites, it is difficult to prove that CMAQ simulations at resolutions greater than 4.5 km are more accurate at calculating ground level ozone.

It is difficult to simulate or parameterize fine spatial scale features, such as fair-weather cumulus cloud development and a bay breeze, at a coarse resolution. However, it is impractical to run model simulations at a horizontal resolution of 0.5 km for many projects due to computational restraints. The results discussed earlier can be used to help improve coarse model simulations. Even though cloud fraction and liquid water content decreases with increasing resolution in the base case simulations, the rate of SO_2 oxidation increases with increasing resolution, due to more vertical transport through

clouds. Also, more pollutants are transported out of the PBL to the free troposphere. These results suggest that the vertical diffusion scheme for coarse simulations could be modified to produce faster vertical transport to allow more pollutants to be transported into clouds and across the top of the boundary layer.

In order to simulate a bay, sea, or lake breeze at resolutions coarser than 4.5 km, a bay, sea, or lake breeze parameterization needs to be developed. Otherwise, finer horizontal resolutions are needed along coastlines. This can be accomplished with nested simulations along coastlines or a stretched grid with the resolution increasing as the distance from the coastline decreases.

2.5 Conclusions

In this study, CMAQ simulations at 13.5, 4.5, 1.5, and 0.5 km horizontal resolution are performed using the corresponding meteorological modeling results. Results show that more sulfur dioxide is converted to sulfate aerosols as the resolution increases when fair-weather cumulus clouds are present. Even though for the base case simulations there are fewer clouds in the higher resolution simulations, more pollutants are transported vertically through clouds causing more sulfur dioxide to be converted to sulfate aerosols. Also, in higher resolution simulations more pollutants are vented out of the PBL to the free troposphere, where winds are faster, and transported downwind at a faster rate.

CMAQ uses one method to diagnose clouds for aqueous chemistry calculations and another for photolysis rates. For this modeling scenario, use of the photolysis scheme's clouds in both the photolysis and aqueous chemistry schemes leads to better agreement with GOES visible satellite observations. Simulations using the photolysis

scheme's clouds in the aqueous chemistry scheme displays an increase in sulfur dioxide oxidation due to the presence of more fair-weather cumulus clouds, showing the importance of accurately modeling the spatial coverage of fair-weather cumulus clouds in order to accurately model sulfate aerosol concentrations.

These results indicate that higher resolution simulations are more capable of simulating horizontal temperature gradients that can cause a bay breeze to form and impact the transport of pollutants. The 4.5, 1.5, and 0.5 km WRF-UCM simulations produce a Chesapeake Bay breeze that starts sooner and is stronger throughout the day than the 13.5 km resolution simulations. This results in less pollutants being transported near the surface over the Chesapeake Bay and instead being transported aloft. Simulations at 4.5, 1.5, and 0.5 km resolution produce higher and more realistic 8-h maximum ozone concentrations at locations near the Bay Breeze convergence zone (e.g., Edgewood) and lower concentrations near the surface of the Chesapeake Bay.

Chapter 3: Roles of an Urban Tree Canopy and Buildings on Urban Heat Island Effects: Parameterization and Application

3.1 Introduction

Urbanization can alter local climate and form an urban heat island (UHI) (Landsberg, 1981). Altering land use by creating impervious urban surfaces causes increased runoff, decreased evapotranspiration, increased solar radiation absorption, additional release of anthropogenic heat, and changes in surface friction, which results in changes in near-surface air temperature, humidity, wind speeds, low-level convergence/divergence, convection, and precipitation (e.g., Oke, 1987; Bornstein and Lin, 2000; Arnfield, 2003). Previous studies show that UHIs strengthen as city size and building density increase (Oke, 1973; Landsberg, 1981; Atkinson, 2003; Imhoff et al., 2010). In addition, a recent study reveals that upstream urbanization can magnify UHI effects (Zhang et al., 2009). Therefore a smaller city with upstream urbanization can have a larger UHI than a larger city with no upstream urbanization (Zhang et al., 2009).

An UHI can have ill effects on human health. The UHI can amplify summertime heat waves leading to heat stress (Kunkel et al., 1996). The UHI can also aggravate air pollution. Air quality model results show air pollution worsens as temperature increases (Weaver et al., 2009; Banta et al., 1998; Cheng and Byun, 2008; Jacob and Winner, 2009), and observations confirm a correlation between high temperature and high air pollution events (Bloomer et al., 2009; Bloomer et al., 2010; Tai et al., 2010).

Urban trees have the potential to dampen the UHI and decrease near-surface temperatures through direct shading and evaporative cooling. Observations show

temperatures over a grassy surface were 0.7-1.3 K cooler under urban trees than adjacent areas with no tree cover (Souch and Souch, 1993). Similarly, measurements revealed temperatures to be 2.2-3.3 K cooler under mature trees in a suburban neighborhood than in new developments with no trees (McGinn, 1982). In general, cooler summertime temperatures can result in less emissions and air pollution. Moreover, air pollution can be deposited onto leaves causing more removal of air pollutants when trees are present.

An UHI also has the potential to alter a sea, lake, or bay breeze, which can affect air quality. A summertime sea breeze is driven by the temperature gradient between the warm land and cool water. Increasing or decreasing land surface temperature through urbanization or planting urban trees, respectively, will alter the temperature gradient and therefore modify the strength of the sea breeze. Previous studies have shown that a sea breeze circulation can exacerbate air pollution levels (Boucouvala and Bornstein, 2003; Evytugina et al., 2006; Loughner et al., 2011). In Houston, high ozone episodes begin when the large scale flow is offshore before a bay breeze develops (Banta et al., 2005; Darby, 2005). As the bay breeze begins to strengthen, stagnant conditions develop allowing ozone and ozone precursors to accumulate before being advected further onshore as the bay breeze increases in intensity later in the afternoon (Banta et al., 2005; Darby, 2005).

With rapid increases in computing power in recent years, there have been a growing number of higher resolution model simulations. Many studies show benefits of using high-resolution mesoscale models to resolve frontal structures, orographical flows, and vertical circulations induced by surface inhomogeneities (see Mass et al., 2002 for review). For urban settings at fine scales (horizontal grid spacing less than 1 km), urban

canopy models are used to simulate the meteorology in the complex urban environment consisting of streets, buildings, and vegetation. Currently, the Weather Research and Forecasting (WRF) model (Skamarock et al., 2008) can be run coupled with the Noah land surface model and an urban canopy model (Kusaka et al., 2001) (WRF-UCM). However, this urban canopy model does not include soil, grass, or trees in urban street canyons. Lee and Park (2008) developed a vegetated urban canopy model and found that canyon vegetation has a large influence on surface temperatures and sensible and latent heat fluxes.

In the present study, the effects of soil, grass, and trees in urban street canyons are incorporated into Version 3.1.1 of the WRF-UCM. How urban trees dampen the UHI and the sensitivity of the UHI to urban building height are examined. These objectives are accomplished by performing simulations down to a horizontal grid spacing of 0.5 km with a modified version of the ARW WRF-UCM in which urban trees, soil, and grass are incorporated. The simulations cover the Washington-Baltimore metropolitan areas from 1200 UTC 7 to 1200 UTC 10 July 2007. This time period is significant in that high air pollution was observed in the region under hot, sunny, stagnant conditions. A cold front passed through the area on 6 July 2007, followed by a short-wave trough approaching the Mid-Atlantic states (Zhang et al., 2011). The Baltimore, MD UHI exhibited a 2 m temperature of 37.5°C and downwind of Baltimore near-surface 8 h maximum ozone mixing ratios reached 125 ppb (the current air quality standard is 75 ppb) on July 9. This same time period was analyzed to investigate the impact of upstream urbanization on the UHI (Zhang et al., 2009; Zhang et al., 2011), to characterize the air pollution event

(Yegorova et al., 2011), and to examine the impact of fair-weather cumulus clouds and the Chesapeake Bay breeze on air quality (Loughner et al., 2011).

3.2 Model description and modification

3.2.1 Model configuration

In the coupled ARW WRF-UCM, the Noah land surface model calculates soil moisture and temperature, skin temperature, canopy water content, and the energy and water flux terms in the surface and water energy balance equations (Chen and Dudhia, 2001), while the UCM improves the parameterization of physical processes involved in the exchange of heat, momentum, and water vapor in urban environments by including shadowing from buildings, reflection of short and longwave radiation, wind profile information in the canopy layer and a multi-layer heat transfer equation for roof, wall, and road surfaces (Kusaka and Kimura, 2004).

The WRF-UCM includes 3 categories of urban surfaces: commercial/industrial/transportation, high-intensity residential, and low-intensity residential. Each urban category consists of fractional coverage of urban land occupied by buildings and roads, with the remaining fraction as undeveloped land. Urban fraction is set to 95%, 90%, and 50% for grid cells labeled commercial/industrial/transportation, high-intensity residential, and low-intensity residential urban, respectively, for the model simulations described herein. The remaining land in grid cells classified as urban is considered undeveloped and classified as USGS land use type Cropland/Grassland Mosaic. Surface heat and moisture fluxes are calculated in the UCM for urban streets and buildings and in the Noah land surface model for undeveloped urban land.

The coupled model is run at 13.5, 4.5, 1.5, and 0.5 km horizontal grid spacing with (x, y) dimensions of 181 x 151, 244 x 196, 280 x 247, and 349 x 349 grid cells, respectively (see Figure 3-1 for the model domains). All of the domains use 32 layers in the vertical with 20 layers in the lowest 2 km. The North American Regional Reanalysis is used for the model initial and outermost lateral boundary conditions. The 3 category urban surfaces are defined by the U.S. Environmental Protection Agency's National Land Cover Dataset for Year 2001. The urban areas in the 0.5 km domain are displayed in Figure 3-2. The model physics schemes used include (1) a double-moment six-class microphysics scheme (Lim and Hong, 2010), (2) the Mellor-Yamada-Janjic boundary layer parameterization (Janjic, 1994), (3) the Noah Land Surface Model (Chen and Dudhia, 2001), and (4) an ensemble cumulus parameterization that advances the Grell-Devenyi scheme (Grell and Devenyi, 2002) to allow subsidence in neighboring grid cells (Skamarock et al., 2008). The cumulus parameterization is only used for the 4.5 and 13.5 km domains.

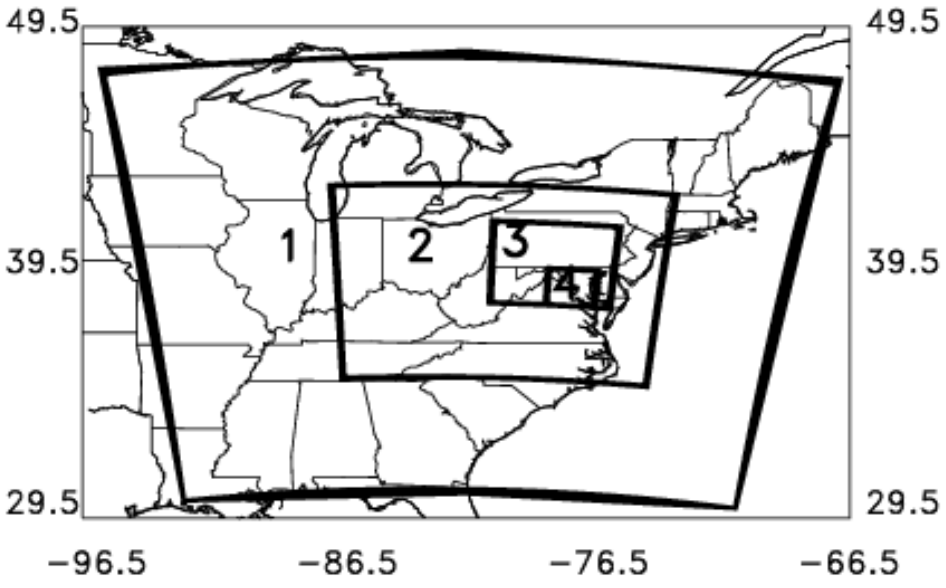

Figure 3-1: Location of modeling domains 1, 2, 3, and 4, which have horizontal grid spacing of 13.5, 4.5, 1.5, and 0.5 km, respectively.

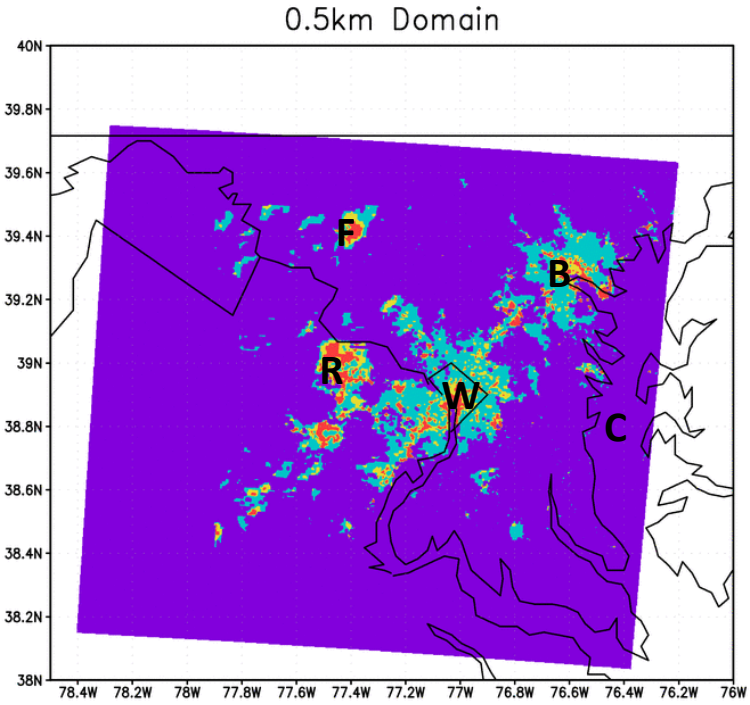

Figure 3-2: Urban land use in the 0.5 km horizontal resolution domain, where red, yellow, and cyan represent commercial/industrial/transportation, high-intensity residential, and low-intensity residential, respectively. The letters F, R, B, and W denotes the cities of Frederick, MD, Reston, VA, Baltimore, MD, and Washington, DC, respectively. The letter C shows the location of the Chesapeake Bay.

Three different WRF-UCM simulations were performed to achieve the above-mentioned objectives: 1) a base case, 2) with urban soil, grass, and trees, and 3) with shorter buildings. Hereafter, these simulations are referred to as No Trees, Trees, and No Trees Shorter Buildings. Urban fraction and building and canyon dimensions for the three model simulations and three urban categories are displayed in Table 3-1. The No Trees Shorter Buildings simulation is performed to test the sensitivity of the UHI effects to building height.

	Urban Fraction			Building Height (m)			Building Depth (m)			Urban Canyon Width (m)		
	LI	HI	C	LI	HI	C	LI	HI	C	LI	HI	C
NT	0.5	0.9	0.95	7.5	10	20	8.3	9.4	10	8.3	9.4	10
T	0.5	0.9	0.95	7.5	10	20	8.3	9.4	10	8.3	9.4	10
NTSB	0.5	0.9	0.95	5	7.5	12	8.3	9.4	10	8.3	9.4	10

Table 3-1: Specification of urban fraction, building height and depth, and urban canyon width for the three urban categories [low-intensity residential (LI), high-intensity residential (HI), and commercial/industrial/transportation (C)) and three simulations (No Trees (NT), Trees (T), and No Trees Shorter Buildings (NTSB)].

3.2.2 Parameterization of trees for the UCM

The WRF-UCM was modified to investigate how urban trees impact the UHI effects. The WRF-UCM was tailored to include grass, soil, and trees in urban street canyons and trees in undeveloped land in urban grid cells. Urban vegetation coverage is described in Tables 3-2 and 3-3. Urban canyon tree height is set to 10 m. Urban tree leaf area index (LAI) is set to 3.31, the same as USGS land use type Deciduous Broadleaf Forest and inline with favorable urban trees found in the Mid-Atlantic. Averaged LAIs by individual tree species from a tree survey in New York City range from 0.68 for honeylocust trees to 10.07 for northern white cedar trees (TreesNY and CENYC et al., 2002). Ideally, urban trees must be durable, able to thrive in an urban environment, low biogenic volatile organic compound (VOC) emitters, and have a large LAI to cause maximum shading, latent heat exchange, and pollutant deposition. A list of urban tree species from the USDA Forest Service (Chicago Botanic Garden, 2001) was referenced to find trees that are suitable to live in an urban environment. Biogenic emissions of tree species from the Biogenic Emissions Inventory System (BEIS) (Vukovich and Pierce, 2002) were referenced to find low VOC emitters. LAIs from a New York City tree

survey (TreesNY and CENYC et al., 2002) were referenced to determine which trees have a large LAI. It was determined that ash and elm trees are preferred urban trees for the Washington, DC and Baltimore, MD metropolitan areas. Observed average LAI in New York City for ash and elm trees is 4.11 and 3.12, respectively (TreesNY and CENYC et al., 2002).

	Urban Canyon Tree Canopy Fraction			Undeveloped Land Tree Canopy Fraction			Percent Tree Cover of Total Grid		
	LI	HI	C	LI	HI	C	LI	HI	C
NT	0	0	0	0	0	0	0	0	0
T	0.5	0.5	0.5	0.5	0.5	0.5	37.5	27.5	26.25
NTSB	0	0	0	0	0	0	0	0	0

Table 3-2: Specification of urban canopy tree canopy fraction, undeveloped land tree canopy fraction, and tree cover fraction over total grid cell for the three urban categories [low-intensity residential (LI), high-intensity residential (HI), and commercial/industrial/transportation (C)) and the three simulations (No Trees (NT), Trees (T), and No Trees Shorter Buildings (NTSB)].

	Urban Canyon Grass/Soil Fraction		
	LI	HI	C
NT	0	0	0
T	0.1	0.1	0.1
NTSB	0	0	0

Table 3-3: Urban canyon grass/soil fraction for the three urban categories (low-intensity residential (LI), high-intensity residential (HI), and commercial/industrial/transportation (C)) and the three simulations (No Trees (NT), Trees (T), and No Trees Shorter Buildings (NTSB)).

To increase the percentage tree cover in the undeveloped land from 0% to 50%, the undeveloped land is re-classified from USGS land use type Cropland/Grassland Mosaic to USGS land use type Cropland/Woodland Mosaic. A 50% tree cover over undeveloped land and urban streets results in a 26.25%, 27.5%, and 37.5% tree cover over commercial/industrial/transportation, high-intensity residential, and low-intensity residential urban areas, respectively. Tree canopy cover in urban and metropolitan areas

in the US averages 27% and 33%, respectively (Dwyer and Nowak, 1999). Surface heat and moisture fluxes are calculated with the Noah land surface model for undeveloped urban land and with the UCM for the urban buildings and street canyons.

The UCM was modified to account for fractional coverage of grass, soil, and tree canopies in the street canyons, including the increased momentum drag due to the tree canopy, the transmissivity of shortwave and longwave radiation through the tree canopy, tree shading on building roofs, building walls, and the ground, and additional shortwave radiative, longwave radiative, latent heat, and sensible heat fluxes due to the added trees, soil, and grass. Figure 3-3 depicts a schematic diagram of the modified UCM. The wind speed below treetops is modified to account for the additional trees. The wind speed in the street canyon or at the roof level where the trees are taller than the buildings is multiplied by $\exp(-\upsilon f_l LAI)$, where LAI is the leaf area index above the rooftops or in the street canyon, f_l is the fractional coverage of the tree canopy above the road, and υ is the extinction coefficient and it is set to 0.1 to account for momentum drag due to the tree canopy (Lee and Park, 2008).

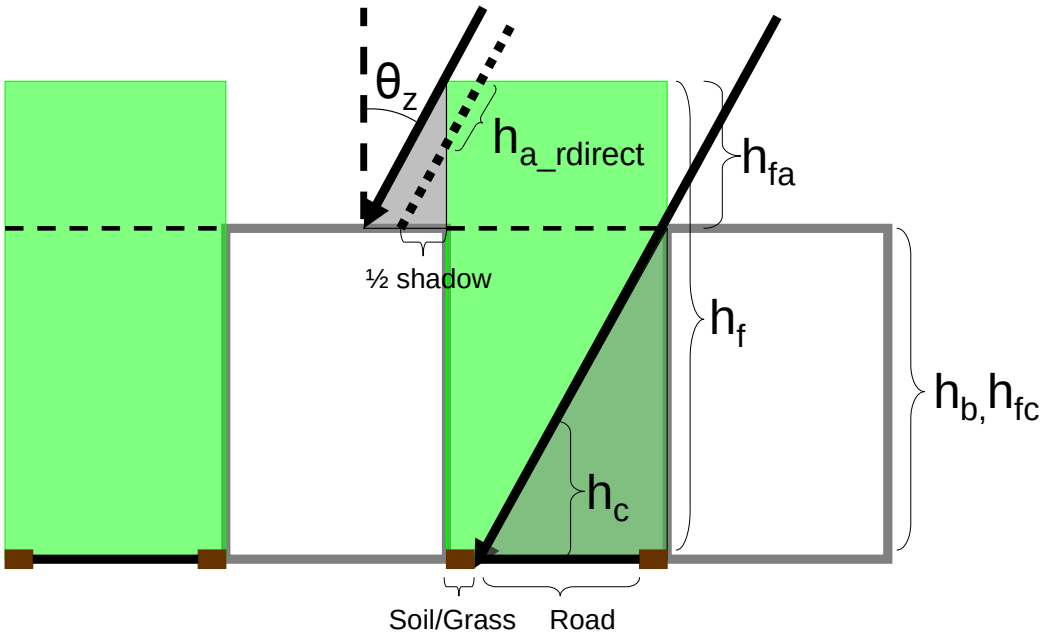

Figure 3-3: Schematic diagram of urban street canyons with trees, where h_f and h_b are tree height and building height, respectively; h_c is height where building shadow covers 50% of the tree leaves, h_{fc} is the height of the highest tree leaf in the canyon, h_{fa} is height of tree above the building, $h_{a\_rdirect}$ is path length of direct solar radiation through tree before reaching the roof, and θ_z is the solar zenith angle.

For trees taller than the adjacent buildings, the tree canopy is split into two layers, one above the building roof and another in the street canyon. The *LAI* above the street canyon is calculated by:

$$LAI_a = (h_f - h_b)\rho_l \qquad \text{(Equation 3-1)},$$

and the *LAI* in the street canyon is defined as:

$$LAI_c = h_b \rho_l \qquad \text{(Equation 3-2)},$$

where h_f and h_b are the tree and building heights, respectively. The density of the leaves is assumed invariant with height and is defined by:

$$\rho_l = \frac{LAI}{h_f} \qquad \text{(Equation 3-3).}$$

A list of all of the variables used to parameterize urban trees in the WRF-UCM is located in Table 3-4.

The amount of radiation that can be transmitted through a tree canopy needs to be defined in order to compute the radiative budget. The transmissivity of radiation through a tree canopy from height z_1 to z_2 is computed by:

$$T(z1, z2) = \exp(\int_{z1}^{z2} -0.5\rho_l \sqrt{\alpha} dz) \qquad \text{(Equation 3-4),}$$

where ρ_l is the leaf area density and α represents the absorptivity for individual leaves (Annandale et al., 2004; Campbell and Norman, 1998; Norman and Wells, 1983).
A typical value of α is 0.5 (Annandale et al., 2004) and is used here.

The direct solar radiation that reaches the surface of the leaves in the street canyon is:

$$S_l^{D*} = S_c^{D\downarrow} f_l \{[1 - T(h_c, h_{fc})]\sin\theta_n + [1 - T(0, h_{fc}](1 - \sin\theta_n)\} \qquad \text{(Equation 3-5),}$$

where $S^{D*}{}_l$, $S^{D\downarrow}{}_c$, h_c, and h_{fc} are the downward direct solar radiation that reaches the surface of leaves, downward direct solar radiation in the canyon, the height of the top of the tree in the canyon, and the average tree shaded height due to the buildings, respectively (Lee and Park, 2008); θ_n is the angle between the average canyon axis and the direction of the sun as described by Kusaka et al. (2001). The first and second terms describe the solar radiation that reaches building shaded and unshaded leaves,
respectively. If the tree height is greater than the adjacent building height, then h_{fc} is set to the building height. The height of the shaded canopy is defined by:

$$h_c = h_{fc} - \frac{w}{2\tan\theta_z \sin\theta_n} \quad \text{(Equation 3-6)},$$

where w is the width of the ground between the buildings and θ_z is the solar zenith angle. If h_c is greater than h_{fc}, then h_c is set to h_{fc}. The direct solar radiation absorbed by the leaves is:

$$S_l^{D\downarrow} = \frac{S_l^{D*}(1-\alpha_l)}{\sigma_l} \quad \text{(Equation 3-7)},$$

and the direct solar radiation reaching the surface of the wall, ground and grass/soil are:

$$S_w^{D\downarrow} = (S_c^{D\downarrow} - S_l^{D*})\frac{l_{shadow}}{2l_{height}} \quad \text{(Equation 3-8)},$$

$$S_{rd}^{D\downarrow} = f_{rd}(S_c^{D\downarrow} - S_l^{D*})\frac{l_{ground} - l_{shadow}}{l_{ground}} \quad \text{(Equation 3-9)},$$

$$S_s^{D\downarrow} = f_s(S_c^{D\downarrow} - S_l^{D*})\frac{l_{ground} - l_{shadow}}{l_{ground}} \quad \text{(Equation 3-10)},$$

where f_{rd} and f_s define the fraction of the ground that is road and grass/soil, respectively, and l_{shadow}, l_{height}, and l_{ground} are the normalized shadow length, normalized building height, and normalized street canyon width, respectively, as defined by Kusaka et al. (2004). The solar radiation absorbed by the leaves is a function of the leaf aspect ratio, σ_l, which is defined as:

$$\sigma_l = LAI^* f_l \quad \text{(Equation 3-11)},$$

where the effective leaf area index is:

$$LAI^* = 2.5[1 - \exp(-0.4LAI)] \quad \text{(Equation 3-12)},$$

as described by Lee and Park (2008).

Symbol	Description	Units
LAI	Leaf area index	-
LAI^*	Effective leaf area index	-
T_l	Temperature of leaves	K
T_{la}	Temperature of leaves above roof level	K
Y	Extinction coefficient	-
ε_l	Emissivity of leaves	-
ρ_l	Leaf density	m^{-1}
σ_l	Leaf aspect ratio	-
α	Absorptivity of a leaf	-
f_l	Tree canopy fraction in street canyon	-
f_{rd}	Road fraction of ground in street canyon	-
f_s	Grass/soil fraction of ground in street canyon	-
h_f	Tree height	m
h_b	Building height	m
h_c	Height of top of tree in street canyon	m
h_{fc}	Average tree shaded height due to buildings	m
h_{fa}	Height between the tree top and building roof level	m
$h_{a\rightarrow r\_direct}$	Distance of path of direct radiation through the tree canopy from the center of the shadow on roof	m
θ_n	Angle between average street axis and sun angle	radians
θ_z	Solar zenith angle	radians
α_r	Albedo of roof	-
w	Width of the ground between the buildings	m
l_{shadow}	Normalized shadow length	-
l_{height}	Normalized building height	-
l_{ground}	Normalized street canyon width	-
l_{shadow_roof}	Normalized shadow on roof	-
$T(z1,z2)$	Transmissivity between heights z1 and z2	-
τ_{wa}	Wall – atmosphere transmissivity	-
τ_{ww}	Wall – wall transmissivity	-
τ_{wg}	Wall – ground transmissivity	-
τ_{ga}	Ground – atmosphere transmissivity	-
$S^{D*}{}_l$	Downward direct solar radiation reaching leaves	W m^{-2}
$S^{D\downarrow}{}_c$	Downward direct solar radiation in street canyon	W m^{-2}
$S^{D\downarrow}{}_w$	Downward direct solar radiation reaching wall	W m^{-2}
$S^{D\downarrow}{}_{rd}$	Downward direct solar radiation reaching road	W m^{-2}
$S^{D\downarrow}{}_s$	Downward direct solar radiation reaching grass/soil	W m^{-2}
$S^{I\downarrow}{}_l$	Indirect solar radiation absorbed by leaves	W m^{-2}
$S^{I\downarrow}{}_c$	Indirect solar radiation in street canyon	W m^{-2}
$S^{I*}{}_l$	Indirect solar radiation reaching leaves if no buildings present	W m^{-2}
$S^{I\downarrow}{}_w$	Indirect solar radiation incident on wall	W m^{-2}
$S^{I\downarrow}{}_{rd}$	Indirect solar radiation incident on road	W m^{-2}

Table 3-4: Description of symbols used to parameterize trees in UCM.

Symbol	Description	Units
$S^{I\downarrow}_{s}$	Indirect solar radiation incident on grass/soil	W m^{-2}
$S^{\uparrow\downarrow}_{w}$	Solar radiation absorbed by wall	W m^{-2}
$S^{\uparrow\downarrow}_{rd}$	Solar radiation absorbed by road	W m^{-2}
$S^{\uparrow\downarrow}_{s}$	Solar radiation absorbed by grass/soil	W m^{-2}
$S^{\uparrow\downarrow}_{l}$	Solar radiation absorbed by leaves	W m^{-2}
S^{D*}_{la}	Direct solar radiation that reaches leaves above roof level	W m^{-2}
$S^{D\downarrow}_{a}$	Direct solar radiation from the atmosphere above	W m^{-2}
S^{I*}_{la}	Indirect solar radiation that reaches leaves above roof level	W m^{-2}
$S^{I\downarrow}_{a}$	Indirect solar radiation from the atmosphere above	W m^{-2}
$S^{D\downarrow}_{la}$	Direct solar radiation absorbed by leaves above roof level	W m^{-2}
$S^{I\downarrow}_{la}$	Indirect solar radiation absorbed by leaves above roof level	W m^{-2}
$S^{D\downarrow}_{la\_side}$	Direct solar radiation absorbed through side of tree canopy above roof level	W m^{-2}
$S^{I\downarrow}_{la\_side}$	Indirect solar radiation absorbed through side of tree canopy above roof level	W m^{-2}
$S^{\downarrow}_{la\_r}$	Solar radiation reflected by roof and absorbed by tree canopy above roof	W m^{-2}
$S^{\uparrow\downarrow}_{r}$	Solar radiation absorbed by roof	W m^{-2}
$L^{l}_{l\uparrow}$	Longwave radiation emitted by leavesthat reaches other leaves	W m^{-2}
$L^{a}_{l\uparrow}$	Longwave radiation emitted by leaves that escapes canyon	W m^{-2}
$L^{w}_{l\uparrow}$	Longwave radiation emitted by leaves that reaches wall	W m^{-2}
$L^{g}_{l\uparrow}$	Longwave radiation emitted by leaves that reaches ground	W m^{-2}
$L^{\uparrow\downarrow}_{w}$	Net longwave radiation on surface of wall	W m^{-2}
$L^{\uparrow\downarrow}_{rd}$	Net longwave radiation on surface of road	W m^{-2}
$L^{\uparrow\downarrow}_{s}$	Net longwave radiation on surface of grass/soil	W m^{-2}
$L^{\uparrow\downarrow}_{l}$	Net longwave radiation on surface of leaves	W m^{-2}
$L^{c}_{la\uparrow}$	Longwave radiation emitted from the tree canopy above the rooftop that enters the street canyon	W m^{-2}
$L_{la\uparrow}$	Longwave radiation emitted from leaves above roof level	W m^{-2}
$L^{la}_{la\uparrow}$	Longwave radiation emitted from leaves that reaches the surface of other leaves above the roof height	W m^{-2}
$L^{\uparrow\downarrow}_{r}$	Longwave radiation absorbed by roof	W m^{-2}
$L^{\uparrow\downarrow}_{la}$	Longwave radiation absorbed leaves above roof level	W m^{-2}
$F_{w\leftrightarrow a}$	Wall – atmosphere view factor	-
$F_{g\leftrightarrow a}$	Ground – atmosphere view factor	-
$F_{w\leftrightarrow g}$	Wall – ground view factor	-
$F_{w\leftrightarrow w}$	Wall – wall view factor	-
$F_{l\leftrightarrow a}$	Leaves – atmosphere view factor	-
$F_{l\leftrightarrow g}$	Leaves – atmosphere view factor	-
$F_{l\leftrightarrow w}$	Leaves – atmosphere view factor	-
$F_{la\_side\leftrightarrow a}$	Side of tree canopy above roof – sky view factor	-
$F_{la\_side\leftrightarrow r}$	Side of tree canopy above roof – roof view factor	-

Table 3-4 (Cont'd): Description of symbols used to parameterize trees in UCM.

Symbol	Description	Units
C_l	Specific heat capacity of leaves	J m^{-2} K^{-1}
H_l	Sensible heat flux of leaves	W m^{-2}
E_l	Moisture flux on leaves	kg m^{-2} s^{-1}
E_{root}	Transpiration from root zone	kg m^{-2} s^{-1}
L_v	Latent heat of vaporization	J kg^{-1}
C_{w1mm}	Specific heat capacity of 1mm water depth	J m^{-2} K^{-1}

Table 3-4 (Cont'd): Description of symbols used to parameterize trees in UCM.

The indirect solar radiation reaching the surface of the leaves if buildings cause no shade is defined by:

$$S_l^{I*} = S_c^{I\downarrow} f_l (1 - T(0, h_f)) \quad \text{(Equation 3-13),}$$

where $S^{I\downarrow}{}_c$ is the downward indirect solar radiation at the top of the street canyon (i.e., roof level) (Lee and Park, 2008).

The indirect solar radiation flux absorbed by the leaves is (Lee and Park, 2008):

$$S_l^{I\downarrow} = \frac{S_l^{I*} F_{l\leftrightarrow a} (1 - a_l)}{s_l} \quad \text{(Equation 3-14),}$$

and the indirect solar radiation incident on the surfaces of the wall, road, and soil are (Lee and Park, 2008):

$$S_w^{I\downarrow} = F_{w\leftrightarrow a} (S_c^{I\downarrow} - S_l^{I*}) \quad \text{(Equation 3-15),}$$

$$S_{rd}^{I\downarrow} = f_{rd} F_{g\leftrightarrow a} (S_c^{I\downarrow} - S_l^{I*}) \quad \text{(Equation 3-16),}$$

$$S_s^{I\downarrow} = f_s F_{g\leftrightarrow a} (S_c^{I\downarrow} - S_l^{I*}) \quad \text{(Equation 3-17),}$$

where $F_{w\leftrightarrow a}$ and $F_{g\leftrightarrow a}$ are the sky view factors at the center of the wall and ground, and $F_{l\leftrightarrow a}$ is the sky view factor of the leaves at half the height of the tree. The sky view factors are computed with the same algorithm as shown in Kusaka et al. (2001).

The mean radiative transmissivities due to the tree canopy within the street canyon are calculated by (Lee and Park, 2008):

$$\tau_{wa} = 1 - f_l[1 - T(\frac{3}{4}h_b, h_{fc})] \quad \text{(Equation 3-18)},$$

$$\tau_{ww} = 1 - f_l[1 - T(\frac{1}{4}h_b, \frac{3}{4}h_b)] \quad \text{(Equation 3-19)},$$

$$\tau_{wg} = 1 - f_l[1 - T(0, \frac{1}{4}h_b)] \quad \text{(Equation 3-20)},$$

$$\tau_{ga} = 1 - f_l[1 - T(0, h_{fc})] \quad \text{(Equation 3-21)},$$

where τ_{wa}, τ_{ww}, τ_{wg}, and τ_{ga} represent the respective transmissivity between the wall and atmosphere above the canyon, two building walls, wall and ground, and ground and atmosphere above the canyon. The UCM allows for solar radiation to be reflected twice within the urban canopy. The solar radiation absorbed by the building wall, road, soil/grass, and tree leaves are defined as:

$$S_w^{\downarrow\uparrow} = (1-\alpha_w)[S_w^{I\downarrow} + S_w^{D\downarrow} + \tau_{wg}\alpha_{rd}(S_{rd}^{I\downarrow} + S_{rd}^{D\downarrow})F_{g\leftrightarrow w} + \tau_{wg}\alpha_s(S_s^{I\downarrow} + S_s^{D\downarrow})F_{g\leftrightarrow w} + \tau_{ww}\alpha_w(S_w^{I\downarrow} + S_w^{D\downarrow})F_{w\leftrightarrow w}] \quad \text{(Equation 3-22)},$$

$$S_{rd}^{\downarrow\uparrow} = (1-\alpha_{rd})[S_{rd}^{I\downarrow} + S_{rd}^{D\downarrow} + \tau_{wg} f_{rd}\alpha_w(S_w^{I\downarrow} + S_w^{D\downarrow})F_{g\leftrightarrow w}] \quad \text{(Equation 3-23)},$$

$$S_s^{\downarrow\uparrow} = (1-\alpha_s)[S_s^{I\downarrow} + S_s^{D\downarrow} + \tau_{wg} f_s\alpha_w(S_w^{I\downarrow} + S_w^{D\downarrow})F_{g\leftrightarrow w}] \quad \text{(Equation 3-24)},$$

$$\begin{aligned} S_l^{\downarrow\uparrow} = {} & S_l^{I\downarrow} + S_l^{D\downarrow} + (1-\alpha_l)[(1-\tau_{wg})\alpha_{rd}(S_{rd}^{I\downarrow} + S_{rd}^{D\downarrow})F_{w\leftrightarrow g} + \\ & (1-\tau_{wg})\alpha_s(S_s^{I\downarrow} + S_s^{D\downarrow})F_{w\leftrightarrow g} + (1-\tau_{ww})\alpha_w(S_w^{I\downarrow} + S_w^{D\downarrow})F_{w\leftrightarrow w} + \\ & (1-\tau_{wg}) f_{rd}\alpha_w(S_w^{I\downarrow} + S_w^{D\downarrow})F_{g\leftrightarrow w} + (1-\tau_{wg}) f_s\alpha_w(S_w^{I\downarrow} + S_w^{D\downarrow})F_{g\leftrightarrow w} + \\ & (1-\tau_{wa})\alpha_w(S_w^{I\downarrow} + S_w^{D\downarrow})F_{a\leftrightarrow w} + (1-\tau_{ga})\alpha_{rd}(S_{rd}^{I\downarrow} + S_{rd}^{D\downarrow})F_{a\leftrightarrow g} + \\ & (1-\tau_{ga})\alpha_s(S_s^{I\downarrow} + S_s^{D\downarrow})F_{a\leftrightarrow g}] \end{aligned} \quad \text{(Equation 3-25)},$$

where subscripts *w*, *g*, and *a* represent the wall, ground, and atmosphere above the canopy, respectively, and *F* is the view factor, and it is calculated in the UCM as given in Kusaka et al. (2001).

Longwave radiation is emitted isotropically from the tree canopy. Some of the radiation emitted from the tree leaves reaches the surface of other leaves within the tree canopy, while the remainder reaches the ground, building walls, or atmosphere above the street canyon. The longwave radiation emitted from tree leaves that reaches the surfaces of other leaves, the atmosphere above the canyon, building walls, and the ground is defined as in Lee and Park (2008):

$$L_{l\uparrow}^{l} = L_{l\uparrow} f_l [1 - T(0, h_{fc})] \quad \text{(Equation 3-26)},$$

$$L_{l\uparrow}^{a} = 0.5\sigma_l [L_{l\uparrow} - L_{l\uparrow}^{l}] F_{l\leftrightarrow a} \quad \text{(Equation 3-27)},$$

$$L_{l\uparrow}^{w} = \frac{w}{2h_b} 0.5\sigma_l [L_{l\uparrow} - L_{l\uparrow}^{l}](2 - F_{l\leftrightarrow a} - F_{l\leftrightarrow g}) \quad \text{(Equation 3-28)},$$

$$L_{l\uparrow}^{g} = 0.5\sigma_l [L_{l\uparrow} - L_{l\uparrow}^{l}] F_{l\leftrightarrow g} \quad \text{(Equation 3-29)},$$

where w is the width of the ground and $L_{l\uparrow}$ is defined as:

$$L_{l\uparrow} = \varepsilon_l \sigma_l T_l^4 \quad \text{(Equation 3-30)},$$

where ε_l and T_l are the emissivity and temperature of the leaves, respectively. The UCM allows for longwave radiation to be reflected twice within the urban canopy. The net longwave radiation at the surfaces of the building walls, roads, grass/soil, and trees are obtained by incorporating the downwelling atmospheric longwave radiation, longwave radiation emitted by building walls and roofs, roads, grass/soil, and trees, and multiple reflections in the urban street canyon: The net longwave radiation at the surface of the wall is

$$L_w^{\downarrow\uparrow} = \varepsilon_w[\tau_{wa}L^{c\downarrow}F_{w\leftrightarrow a} + \tau_{wg}(f_{rd}\varepsilon_{rd}F_{w\leftrightarrow g}\sigma T_{rd}^4 + f_s\varepsilon_s F_{w\leftrightarrow g}\sigma T_s^4) +$$
$$\tau_{ww}\varepsilon_w F_{w\leftrightarrow w}\sigma T_w^4 + L_{l\uparrow}^w - \sigma T_w^4 + \tau_{wg}(f_{rd}(1-\varepsilon_{rd})F_{w\leftrightarrow g}L_{l\uparrow}^{rd} +$$
$$f_s(1-\varepsilon_s)F_{w\leftrightarrow g}L_{l\uparrow}^s) + \tau_{ww}(1-\varepsilon_w)F_{w\leftrightarrow w}L_{l\uparrow}^w +$$
$$\tau_{wg}\tau_{wa}(f_{rd}(1-\varepsilon_{rd})F_{w\leftrightarrow g}F_{g\leftrightarrow a}L^{c\downarrow} + f_s(1-\varepsilon_s)F_{w\leftrightarrow g}F_{g\leftrightarrow a}L^{c\downarrow}) +$$
$$\tau_{wg}\tau_{wg}(f_{rd}(1-\varepsilon_{rd})F_{w\leftrightarrow g}F_{w\leftrightarrow g}\varepsilon_w\sigma T_w^4 + \quad \text{(Equation 3-31).}$$
$$f_s(1-\varepsilon_s)F_{w\leftrightarrow g}F_{w\leftrightarrow g}\varepsilon_w\sigma T_w^4) +$$
$$\tau_{ww}\tau_{wg}(f_{rd}(1-\varepsilon_w)F_{w\leftrightarrow w}F_{w\leftrightarrow g}\varepsilon_g\sigma T_g^4 +$$
$$f_s(1-\varepsilon_w)F_{w\leftrightarrow w}F_{w\leftrightarrow g}\varepsilon_s\sigma T_s^4) +$$
$$\tau_{ww}\tau_{wa}(1-\varepsilon_w)F_{w\leftrightarrow w}F_{w\leftrightarrow a}L^{c\downarrow} + \tau_{ww}\tau_{ww}(1-\varepsilon_w)F_{w\leftrightarrow w}F_{w\leftrightarrow w}\varepsilon_w\sigma T_w^4]$$

The net longwave radiation at the surface of the road is:

$$L_{rd}^{\downarrow\uparrow} = f_{rd}\varepsilon_{rd}[\tau_{ga}L^{c\downarrow}F_{g\leftrightarrow a} + \tau_{wg}\varepsilon_w F_{w\leftrightarrow g}\sigma T_w^4 +$$
$$L_{l\uparrow}^g - \sigma T_{rd}^4 + \tau_{wg}(1-\varepsilon_w)F_{g\leftrightarrow w}L_{l\uparrow}^w + \tau_{wg}\tau_{wa}(1-\varepsilon_w)F_{g\leftrightarrow w}F_{w\leftrightarrow a}L^{c\downarrow} + \quad \text{(Equation 3-32).}$$
$$\tau_{wg}\tau_{ww}F_{g\leftrightarrow w}F_{w\leftrightarrow w}\varepsilon_w\sigma T_w^4 + \tau_{wg}\tau_{wg}(f_{rd}(1-\varepsilon_w)F_{g\leftrightarrow w}F_{w\leftrightarrow g}\varepsilon_{rd}\sigma T_{rd}^4 +$$
$$f_s(1-\varepsilon_w)F_{g\leftrightarrow w}F_{w\leftrightarrow g}\varepsilon_s\sigma T_s^4)]$$

The net longwave radiation at the surface of the grass/soil is:

$$L_s^{\downarrow\uparrow} = f_s\varepsilon_s[\tau_{ga}L^{c\downarrow}F_{g\leftrightarrow a} + \tau_{wg}\varepsilon_w F_{w\leftrightarrow g}\sigma T_w^4 +$$
$$L_{l\uparrow}^g - \sigma T_s^4 + \tau_{wg}(1-\varepsilon_w)F_{g\leftrightarrow w}L_{l\uparrow}^w + \tau_{wg}\tau_{wa}(1-\varepsilon_w)F_{g\leftrightarrow w}F_{w\leftrightarrow a}L^{c\downarrow} + \quad \text{(Equation 3-33).}$$
$$\tau_{wg}\tau_{ww}F_{g\leftrightarrow w}F_{w\leftrightarrow w}\varepsilon_w\sigma T_w^4 + \tau_{wg}\tau_{wg}(f_{rd}(1-\varepsilon_w)F_{g\leftrightarrow w}F_{w\leftrightarrow g}\varepsilon_{rd}\sigma T_{rd}^4 +$$
$$f_s(1-\varepsilon_w)F_{g\leftrightarrow w}F_{w\leftrightarrow g}\varepsilon_s\sigma T_s^4)]$$

The net longwave radiation on the surface of leaves is:

$$L_l^{\downarrow\uparrow} = L_{l\uparrow}^{l} - L_{l\uparrow} + \frac{\varepsilon_l}{\sigma_l}[\, f_{rd} L^{c\downarrow} F_{g\leftrightarrow a}(1-\tau_{ga}) + f_s L^{c\downarrow} F_{g\leftrightarrow a}(1-\tau_{ga}) +$$
$$f_{rd} F_{g\leftrightarrow w} \varepsilon_w \sigma T_w^4 (1-\tau_{wg}) + f_s F_{g\leftrightarrow w} \varepsilon_w \sigma T_w^4 (1-\tau_{wg}) +$$
$$f_{rd} F_{g\leftrightarrow w} \varepsilon_{rd} \sigma T_{rd}^4 (1-\tau_{wg}) + f_s F_{g\leftrightarrow w} \varepsilon_s \sigma T_s^4 (1-\tau_{wg}) +$$
$$F_{w\leftrightarrow w} \varepsilon_w \sigma T_w^4 (1-\tau_{ww}) + f_{rd} F_{g\leftrightarrow a} \varepsilon_{rd} \sigma T_{rd}^4 (1-\tau_{ga}) +$$
$$f_s F_{g\leftrightarrow a} \varepsilon_s \sigma T_s^4 (1-\tau_{ga}) + F_{w\leftrightarrow a} \varepsilon_w \sigma T_w^4 (1-\tau_{wa}) +$$
$$(1-\tau_{ga})(\, f_{rd}(1-\varepsilon_{rd}) F_{g\leftrightarrow a} L_{l\uparrow}^{g} + f_s (1-\varepsilon_s) F_{g\leftrightarrow a} L_{l\uparrow}^{g} +$$
$$\tau_{ga} f_{rd}(1-\varepsilon_{rd}) F_{g\leftrightarrow a} F_{a\leftrightarrow g} L^{c\downarrow} + \tau_{ga} f_s (1-\varepsilon_s) F_{g\leftrightarrow a} F_{a\leftrightarrow g} L^{c\downarrow} +$$
$$\tau_{wg} f_{rd}(1-\varepsilon_{rd}) F_{g\leftrightarrow a} F_{w\leftrightarrow g} \varepsilon_w \sigma T_w^4 + \tau_{wg} f_s (1-\varepsilon_s) F_{g\leftrightarrow a} F_{w\leftrightarrow g} \varepsilon_w \sigma T_w^4) +$$
$$(1-\tau_{wa})(1-\varepsilon_w) F_{w\leftrightarrow a} L_{l\uparrow}^{w} + (1-\varepsilon_w) F_{w\leftrightarrow a} F_{a\leftrightarrow w} L^{c\downarrow} +$$
$$\tau_{ww}(1-\varepsilon_w) F_{w\leftrightarrow a} F_{w\leftrightarrow w} \varepsilon_w \sigma T_w^4 + \tau_{wg}(1-\varepsilon_w) F_{w\leftrightarrow a} F_{g\leftrightarrow w} \varepsilon_{rd} \sigma T_{rd}^4 +$$
$$\tau_{wg}(1-\varepsilon_w) F_{w\leftrightarrow a} F_{g\leftrightarrow w} \varepsilon_s \sigma T_s^4) + (1-\tau_{wg})(\, f_{rd}(1-\varepsilon_{rd}) F_{w\leftrightarrow g} L_{l\uparrow}^{g} +$$
$$f_s (1-\varepsilon_s) F_{w\leftrightarrow g} L_{l\uparrow}^{g}) + (1-\tau_{ww})(1-\varepsilon_w) F_{w\leftrightarrow w} L_{l\uparrow}^{w} +$$
$$\tau_{ga}(1-\tau_{ww})(\, f_{rd}(1-\varepsilon_{rd}) F_{w\leftrightarrow g} F_{g\leftrightarrow s} L^{c\downarrow} + f_s (1-\varepsilon_s) F_{w\leftrightarrow g} F_{g\leftrightarrow s} L^{c\downarrow}) +$$
$$\tau_{wg}(1-\tau_{wg})(\, f_{rd}(1-\varepsilon_{rd}) F_{g\leftrightarrow w} F_{w\leftrightarrow g} \varepsilon_w \sigma T_w^4 +$$
$$f_s (1-\varepsilon_s) F_{g\leftrightarrow w} F_{w\leftrightarrow g} \varepsilon_w \sigma T_w^4) + \tau_{wa}(1-\tau_{ww})(1-\varepsilon_w) F_{w\leftrightarrow s} F_{w\leftrightarrow w} L^{c\downarrow} +$$
$$\tau_{wg}(1-\tau_{ww})(\, f_{rd}(1-\varepsilon_w) F_{w\leftrightarrow g} F_{w\leftrightarrow w} \varepsilon_{rd} \sigma T_{rd}^4 +$$
$$f_s (1-\varepsilon_w) F_{w\leftrightarrow g} F_{w\leftrightarrow w} \varepsilon_s \sigma T_s^4) + \tau_{ww}(1-\tau_{ww})(1-\varepsilon_w) F_{w\leftrightarrow w} F_{w\leftrightarrow w} \varepsilon_w \sigma T_w^4 +$$
$$(1-\tau_{wg})(\, f_{rd}(1-\varepsilon_w) F_{g\leftrightarrow w} L_{l\uparrow}^{w} + f_s (1-\varepsilon_w) F_{g\leftrightarrow w} L_{l\uparrow}^{w}) +$$
$$\tau_{wa}(1-\tau_{wg})(\, f_{rd}(1-\varepsilon_w) F_{g\leftrightarrow w} F_{w\leftrightarrow s} L^{c\downarrow} + f_s (1-\varepsilon_w) F_{g\leftrightarrow w} F_{w\leftrightarrow s} L^{c\downarrow}) +$$
$$\tau_{wg}(1-\tau_{wg})(\, f_{rd}(\, f_{rd}(1-\varepsilon_w) F_{w\leftrightarrow g} F_{g\leftrightarrow w} \varepsilon_{rd} \sigma T_{rd}^4 +$$
$$f_s (1-\varepsilon_w) F_{w\leftrightarrow g} F_{g\leftrightarrow w} \varepsilon_s \sigma T_s^4) +$$
$$\tau_{ww}(1-\tau_{wg})(\, f_{rd}(1-\varepsilon_w) F_{w\leftrightarrow w} F_{g\leftrightarrow w} \varepsilon_w \sigma T_w^4 +$$
$$f_s (1-\varepsilon_w) F_{w\leftrightarrow w} F_{g\leftrightarrow w} \varepsilon_w \sigma T_w^4) +$$
$$\tau_{wg}(1-\tau_{wg})\, f_s (\, f_{rd}(1-\varepsilon_w) F_{w\leftrightarrow g} F_{g\leftrightarrow w} \varepsilon_{rd} \sigma T_{rd}^4 +$$
$$f_s (1-\varepsilon_w) F_{w\leftrightarrow g} F_{g\leftrightarrow w} \varepsilon_s \sigma T_s^4)] \qquad \text{(Equation 3-34).}$$

The UCM is coupled with the Noah land surface model to obtain the latent and sensible heat fluxes at the soil surface by passing the incident longwave and shortwave radiation at the soil surface. The sensible heat flux of the tree canopy, the moisture flux on tree leaves, and transpiration from the root zone are calculated, following Lee and

Park (2008). Transpiration from the root zone is obtained from the Noah land surface model, as a function of stomotal resistance.

The temperature of the tree leaves (T_l) is calculated using the energy balance equation of the tree canopy:

$$C_l \frac{\partial T_l}{\partial t} = S_l^{\downarrow\uparrow} + L_l^{\downarrow\uparrow} - H_l - L_v(E_l + E_{root}) \quad \text{(Equation 3-35)},$$

where C_l is the specific heat capacity of the leaves defined by:

$$C_l = C_{w1mm} LAI \quad \text{(Equation 3-36)},$$

L_v is the latent heat of vaporization, H_l is the sensible heat flux, E_l is the moisture flux on the tree leaves, and E_{root} is the transpiration from the root zone (Lee and Park, 2008). C_{w1mm} is set to 4186Jm^{-2}K^{-1}, which is the heat capacity of 1mm water depth.

If trees are taller than the adjacent buildings, then the heat and moisture fluxes are calculated for the portion of the tree canopy above the roof height and tree shading of the roof is considered. The direct and indirect solar radiation that reaches the leaves above the roof height are:

$$S_{la}^{D*} = S_a^{D\downarrow} f_l [1 - T(0, h_{fa}] \quad \text{(Equation 3-37)},$$

$$S_{la}^{I*} = S_a^{I\downarrow} f_l (1 - T(0, h_{fa})) \quad \text{(Equation 3-38)},$$

where S^{D*}_{la}, $S^{D\downarrow}_{a}$, S^{I*}_{la}, $S^{I\downarrow}_{a}$, and h_{fa} are the downward direct solar radiation that reaches the surfaces of the leaves, downward direct solar radiation from the atmosphere above, downward indirect solar radiation reaching the surfaces of the leaves, downward indirect solar radiation from the atmosphere, and height between the tree top and building roof level, respectively. The amount of direct and indirect solar radiation absorbed by the tree canopy entering the top of the tree canopy is defined as:

$$S_{la}^{D\downarrow} = \frac{S_{la}^{D^*}(1-\alpha_l)}{\sigma_l} \quad \text{(Equation 3-39)},$$

$$S_{la}^{I\downarrow} = \frac{S_{la}^{I^*}(1-\alpha_l)}{\sigma_l} \quad \text{(Equation 3-40)}.$$

Solar radiation is also transmitted through the sides of the tree canopy above the roof. The respective direct and indirect solar radiation absorbed through the side of the tree canopy are:

$$S_{la\_side}^{D\downarrow} = \frac{l_{shadow\_roof}}{h_{fa}} \frac{S_{la}^{D^*}(1-\alpha_l)}{\sigma_l} \quad \text{(Equation 3-41)},$$

$$S_{la\_side}^{I\downarrow} = \frac{S_{la}^{I^*}(1-\alpha_l)F_{la\_side\leftrightarrow a}}{\sigma_l} \quad \text{(Equation 3-42)},$$

where l_{shadow_roof} and $F_{la\_side\leftrightarrow a}$ is the normalized shadow on the roof and the view factor between the side of the tree canopy and the atmosphere above. The amount of solar radiation reflected from the roof and absorbed by the tree canopy is:

$$S_{la\_r}^{\downarrow} = \frac{S_r^{\downarrow\uparrow}(1-T(0,h_{fa})f_l\alpha_r(1-\alpha_l)F_{la\_side\leftrightarrow r}}{(1-\alpha_r)\sigma_l} \quad \text{(Equation 3-43)},$$

where $S^{\downarrow\uparrow}{}_r$, α_r, and $F_{la\_side\leftrightarrow r}$ are the solar radiation absorbed by the roof, albedo of the roof, and view factor between the roof and the side of the tree canopy, respectively. So, the solar radiative flux on the tree canopy above the rooftop is:

$$S_{la} = S_{la}^{D\downarrow} + S_{la}^{I\downarrow} + S_{la\_side}^{D\downarrow} + S_{la\_side}^{I\downarrow} + S_{la\_r}^{\downarrow} \quad \text{(Equation 3-44)}.$$

The solar radiative flux on the roof is:

$$S_r^{\downarrow\uparrow} = \frac{l_{roof} - l_{shadow\_roof}}{l_{roof}}(1-\alpha_r)S_a^{D\downarrow} +$$

$$[1-\frac{l_{roof} - l_{shadow\_roof}}{l_{roof}}](1-\alpha_r)S_a^{D\downarrow}\{1- f_l[1-T(0,h_{a\rightarrow r\_direct})]\} + \quad \text{(Equation 3-45),}$$

$$S_a^{I\downarrow}(1-\alpha_r)F_{r\leftrightarrow a} +$$

$$S_a^{I\downarrow}(1-\alpha_r)(1-F_{r\leftrightarrow a})\{1- f_l[1-T(0,h_{fa})]\}$$

where $h_{a\rightarrow r\_direct}$ is the distance of the path of the direct radiation through the tree canopy from the center of the shadow on the roof ($l_{shadow\_roof}/2$). The first term in the equation above is the amount of direct solar radiation that reaches the roof with no obstructions and is absorbed by the roof, the second term represents the transmitted direct solar radiation through the tree absorbed by the roof, the third term is the indirect solar radiation that reaches the roof with no obstructions and is absorbed by the roof, and the fourth term is the indirect solar radiation transmitted through the tree canopy that is absorbed by the roof.

When the trees are taller than the building height, the amount of longwave radiation entering the street canyon is:

$$L^{c\downarrow} = L^{a\downarrow}\{1- f_l[1-T(0,h_{fa})]\} + L^c_{la\uparrow} \quad \text{(Equation 3-46),}$$

where $L^c_{la\uparrow}$ is the amount of longwave radiation emitted from the tree canopy above the rooftop that enters the street canyon, defined by

$$L^c_{la\uparrow} = 0.5\sigma_l(L_{la\uparrow} - L^{la}_{la\uparrow}) \quad \text{(Equation 3-47),}$$

where $L_{la\uparrow}$ is emitted from the tree canopy above the roof defined by:

$$L_{la\uparrow} = \varepsilon_l\sigma_l T_{la}^4 \quad \text{(Equation 3-48),}$$

and $L^{la}_{la\uparrow}$ is the amount of longwave radiation that is emitted from the tree that reaches the surface of other tree leaves above the roof height:

$$L_{la\uparrow}^{la} = L_{la\uparrow} f_l [1 - T(0, h_{fa})] \quad \text{(Equation 3-49),}$$

where T_{la} is the temperature of the leaves above the roof.

The longwave radiation flux when the trees are taller than the adjacent buildings is defined as:

$$L_r^{\downarrow\uparrow} = \varepsilon_r [L^{a\downarrow} F_{r\leftrightarrow a} + L^{a\downarrow}(1 - F_{r\leftrightarrow a})\{1 - f_l [1 - T(0, h_{fa})]\} - \sigma T_r^4 + 0.25 \frac{w}{h_{fa}} \sigma_l (L_{la\uparrow} - L_{la\uparrow}^{la})(2 - F_{lr\leftrightarrow a} - F_{lr\leftrightarrow r}) F_{r\leftrightarrow lr\_side} \quad \text{(Equation 3-50),}$$

where the first term is the amount of longwave radiation from the atmosphere that is not obstructed by the tree canopy and is absorbed by the roof, the second term is the amount of longwave radiation from aloft that is transmitted through the tree canopy and absorbed by the roof, the third term is the amount of longwave radiation emitted by the roof, and the fourth term is the amount of radiation that is emitted by the tree canopy and absorbed by the roof.

The longwave radiation flux in the tree canopy above the rooftop is the sum of the amount of radiation that is emitted from the road, grass/soil, building walls, building roof, tree canopy in and above the canyon, and atmosphere above the trees that is captured by the tree leaves minus the amount of radiation emitted from the tree canopy above rooftops, which is defined as:

$$L_{la}^{\downarrow\uparrow} = -L_{la\uparrow} + L_{la\uparrow}^{la} + \frac{\varepsilon_{la}}{\sigma_l} f_l[1-T(0,h_{fa})][(L^{a\downarrow} +$$
$$\sigma\varepsilon_r T_r^4 F_{la\leftrightarrow r} + f_{rd}\sigma\varepsilon_{rd}T_{rd}^4\tau_{ga}F_{a\leftrightarrow g} +$$
$$f_g\sigma\varepsilon_g T_g^4\tau_{ga}F_{a\leftrightarrow g} + \sigma\varepsilon_w T_w^4\tau_{wa}F_{a\leftrightarrow w} + L_{l\uparrow}^a +$$
$$[f_{rd}(1-\varepsilon_{rd})F_{a\leftrightarrow g}L_{l\uparrow}^g + f_{rd}(1-\varepsilon_{rd})F_{a\leftrightarrow g}L^{c\downarrow}F_{g\leftrightarrow a}\tau_{ga} +$$
$$(1-\varepsilon_{rd})F_{g\leftrightarrow w}\sigma\varepsilon_w T_w^4 F_{g\leftrightarrow a}\tau_{wg} + f_s(1-\varepsilon_s)F_{a\leftrightarrow g}L_{l\uparrow}^g + \qquad \text{(Equation 3-51).}$$
$$f_s(1-\varepsilon_s)F_{a\leftrightarrow g}L^{c\downarrow}F_{g\leftrightarrow a}\tau_{ga} + (1-\varepsilon_s)F_{g\leftrightarrow w}\sigma\varepsilon_w T_w^4 F_{g\leftrightarrow a}\tau_{wg}]\tau_{ga} +$$
$$[(1-\varepsilon_w)F_{a\leftrightarrow w}L_{l\uparrow}^w + (1-\varepsilon_w)F_{a\leftrightarrow w}L^{c\downarrow}F_{w\leftrightarrow a}\tau_{wa} +$$
$$(1-\varepsilon_w)F_{a\leftrightarrow w}\sigma\varepsilon_w T_w^4 F_{w\leftrightarrow w}\tau_{ww} +$$
$$(1-\varepsilon_w)F_{a\leftrightarrow w}f_{rd}\sigma\varepsilon_{rd}T_{rd}^4 F_{w\leftrightarrow g}\tau_{wg} +$$
$$(1-\varepsilon_w)F_{a\leftrightarrow w}f_s\sigma\varepsilon_s T_s^4 F_{w\leftrightarrow g}\tau_{wg}]\tau_{wa}]$$

The sensible heat and moisture fluxes, transpiration, and temperature of the leaves for the portion of the tree above the street canyon are calculated using the same algorithms as described above for the tree canopy in the street canyons.

3.3 Sensitivity simulations

Three nested-grid simulations (i.e., No Trees, Trees, and No Trees Shorter Buildings) with the finest grid spacing of 0.5 km are analyzed alongside observations to investigate the role of urban trees and building heights on the UHI. Averaged over 23 measurement sites within the 0.5 km resolution domain, the near-surface (at z = 2 m) temperature for all three simulations are compared to temperature and wind velocity observations from the National Weather Service and the Maryland Department of the Environment (Figure 3-4). The observational sites include urban sites and sites that are downwind and upwind of urban areas. The Trees simulation consistently has lower surface temperatures than the No Trees simulation due to increased evapotranspiration and shading of roads and buildings. At the measurement sites, the surface temperature of

the Trees simulation is on average 0.3 K cooler than the No Trees simulation between 0000 UTC 8 July and 1200 UTC 10 July. The No Trees Shorter Buildings simulation has higher daytime temperatures but lower nighttime temperatures than the No Trees simulation. Averaged over all of the measurement sites, maximum differences between the No Trees Shorter Buildings and No Trees simulations peaked at 0.4 K during the day and 1.2 K during the night. Shorter buildings produce fewer shadows, thereby allowing more solar radiation to heat the building walls and roads. On the other hand, street canyons with shorter buildings trap less longwave radiation emitted from the surfaces allowing the surface to cool quicker during the nighttime.

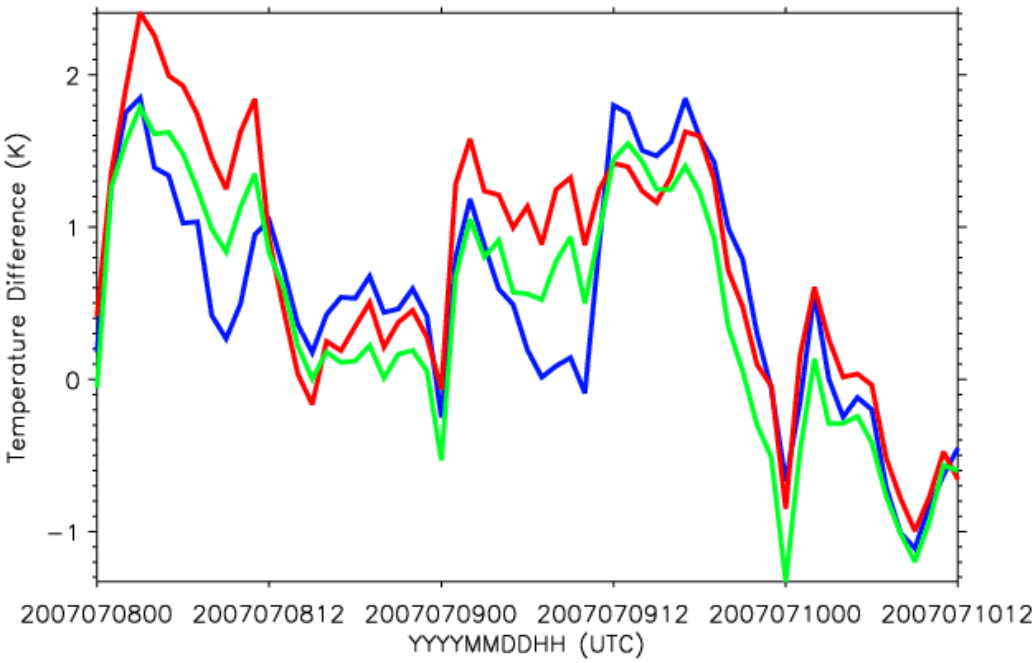

Figure 3-4: Timeseries of No Trees (red), No Trees Shorter Buildings (blue), and Trees (green) simulated 2 m temperature minus observed 2 m temperature at 23 measurement sites within the 0.5 km horizontal resolution domain. Results are averaged over 23 measurement sites.

At 2000 UTC (1500 LST) July 9, 2007, the Chesapeake Bay breeze's convergence zone was over Baltimore, MD (Figure 3-5), and at 2300 UTC (1800 LST) it was between Washington, DC and Baltimore, MD (Figure 3-6). The No Trees Shorter Buildings simulation is slightly warmer than the No Trees simulation. The maximum 2 m temperature difference between the No Trees Shorter Buildings and No Trees simulations in Washington, DC is 0.6 K at 2000 UTC and 0.4 K at 2300 UTC 9 July, (not shown). Even though this difference is small, it can be seen from Figures 3-5 and 3-6 that the spatial extent of the highest temperatures in the region is largest in the No Trees Shorter Buildings simulation followed by the No Trees and then the Trees simulations.

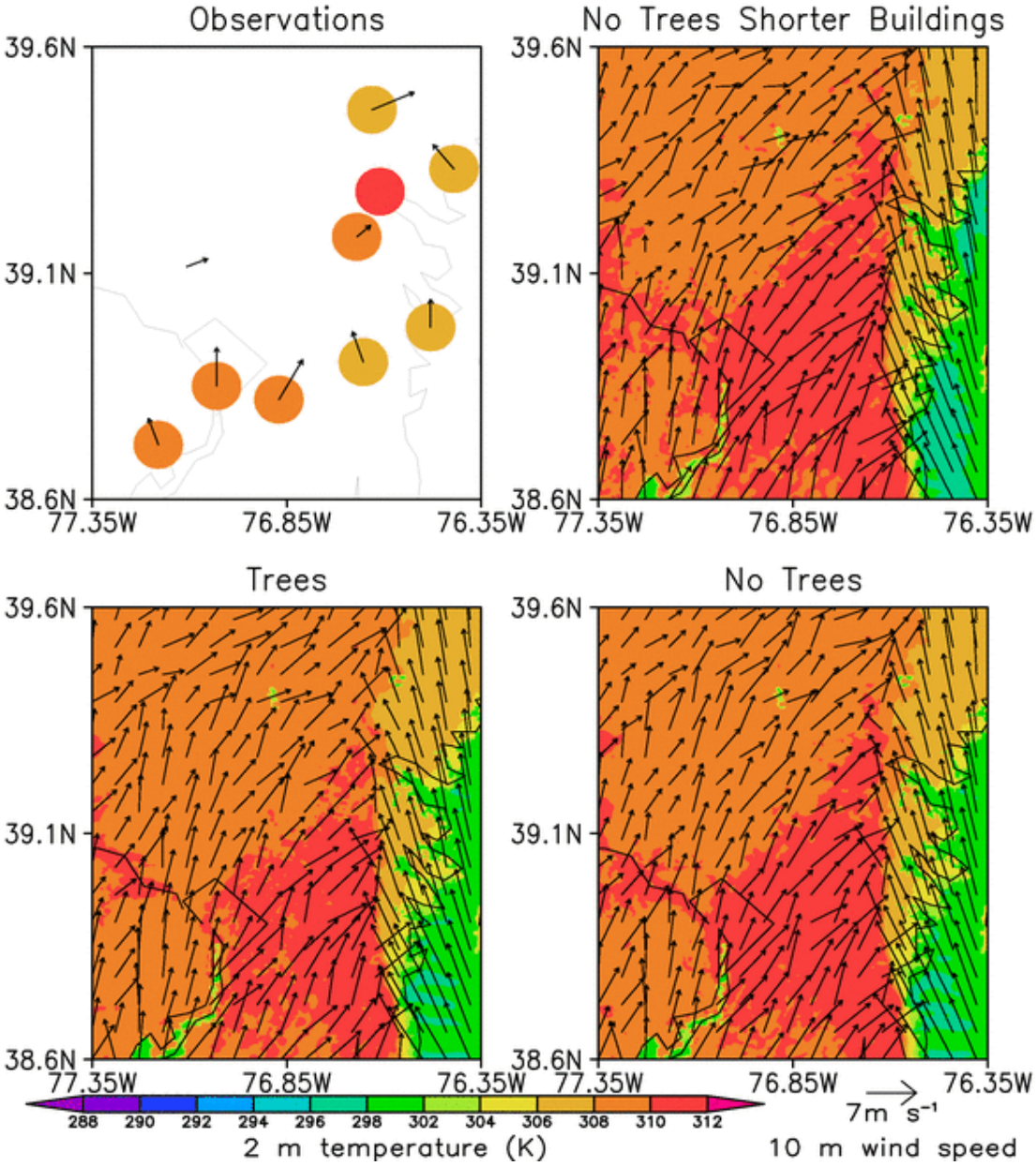

Figure 3-5: Observed and simulated 2 m temperature and 10 m wind speed with a horizontal resolution of 0.5 km at 2000 UTC (3 PM EST) 9 July 2007.

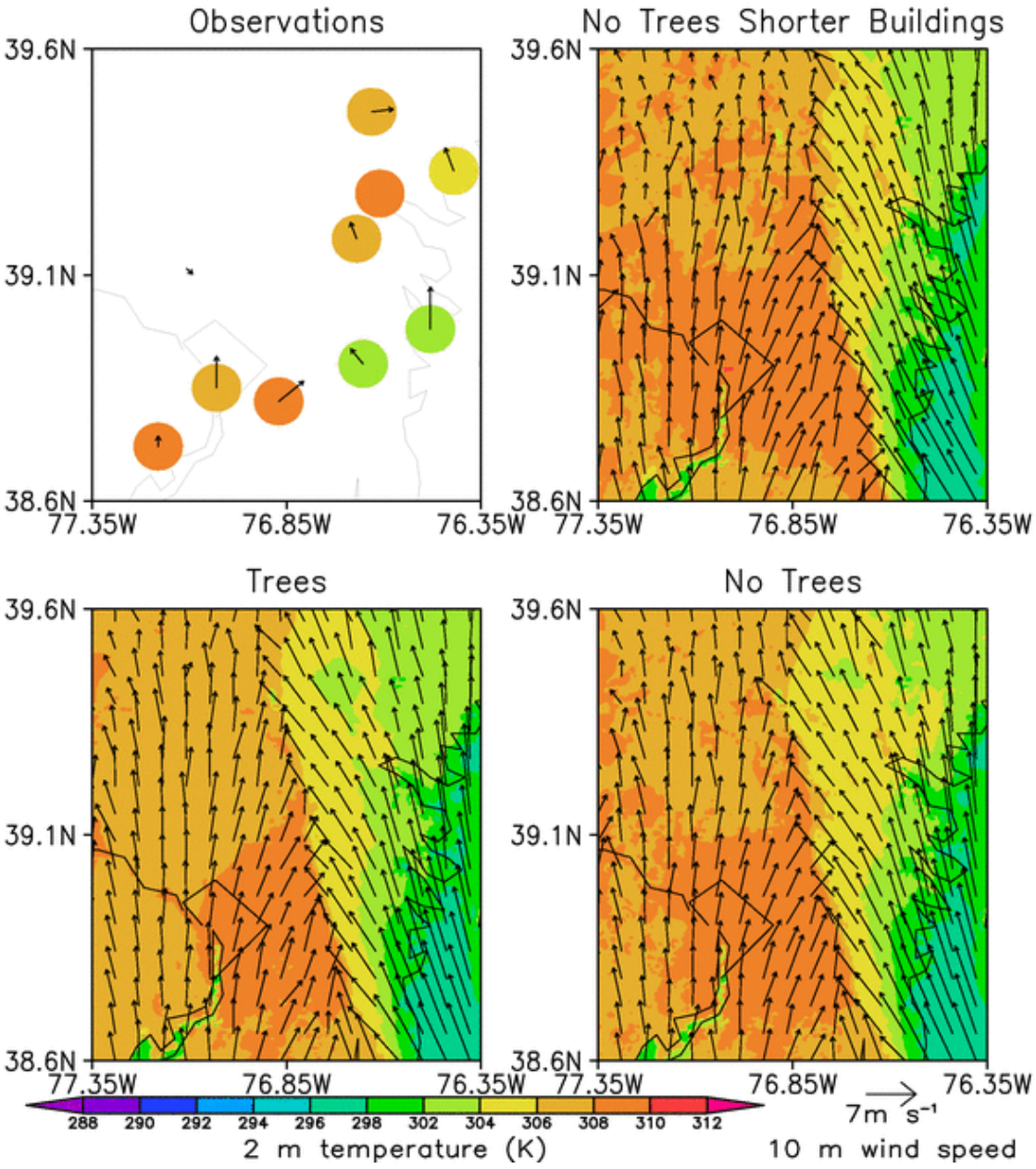

Figure 3-6: Observed and simulated 2 m temperature and 10 m wind speed with a horizontal resolution of 0.5 km at 2300 UTC (6 PM EST) 9 July 2007.

The maximum difference between the No Trees and Trees simulated 2 m temperature is 0.8 and 1.2 K at 2000 and 2300 UTC, respectively, in Washington, DC and 1.9 K at 2000 and 2300 UTC in Baltimore, MD. Differences in 2 m temperature between the No Trees and the Trees simulations at 2000 (Figure 3-7) and 2300 UTC

(Figure 3-8) show that thethe impact of planting trees in all urban areas in the domain is largest in Baltimore, MD.

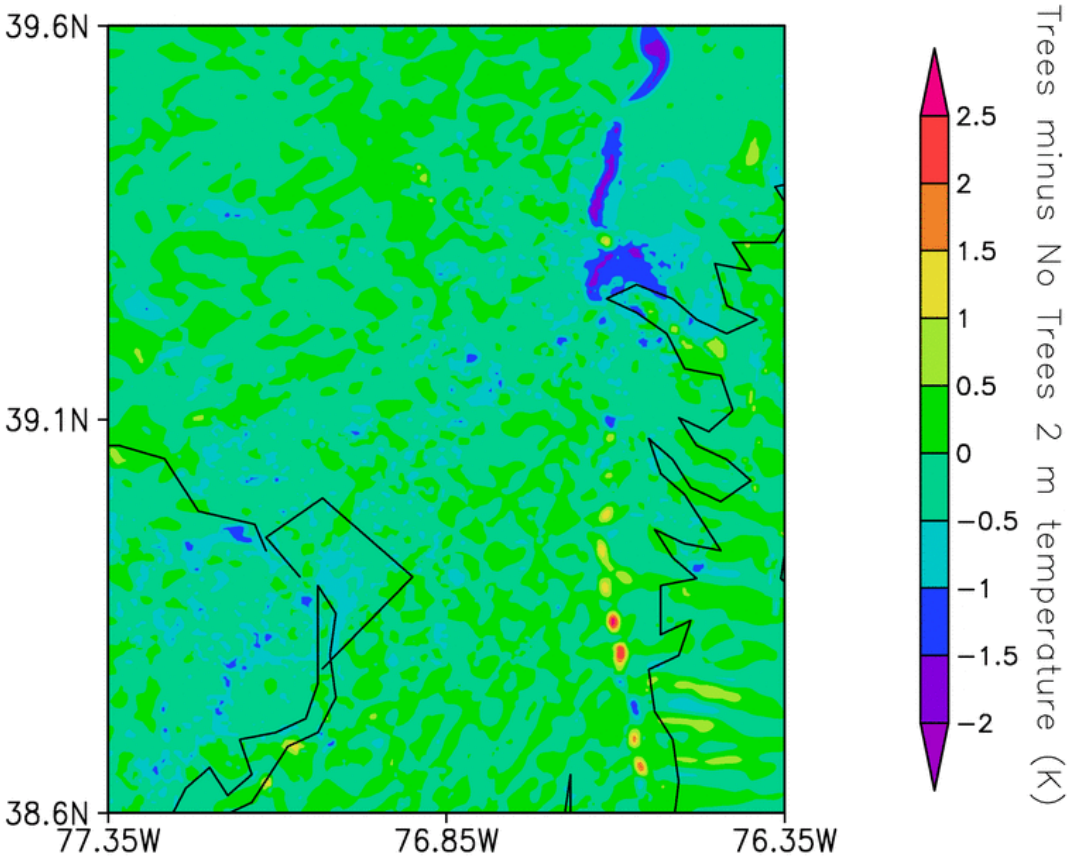

Figure 3-7: Trees minus No Trees simulated 2 m temperature with a horizontal resolution of 0.5 km at 2000 UTC (3 PM EST) 9 July 2007.

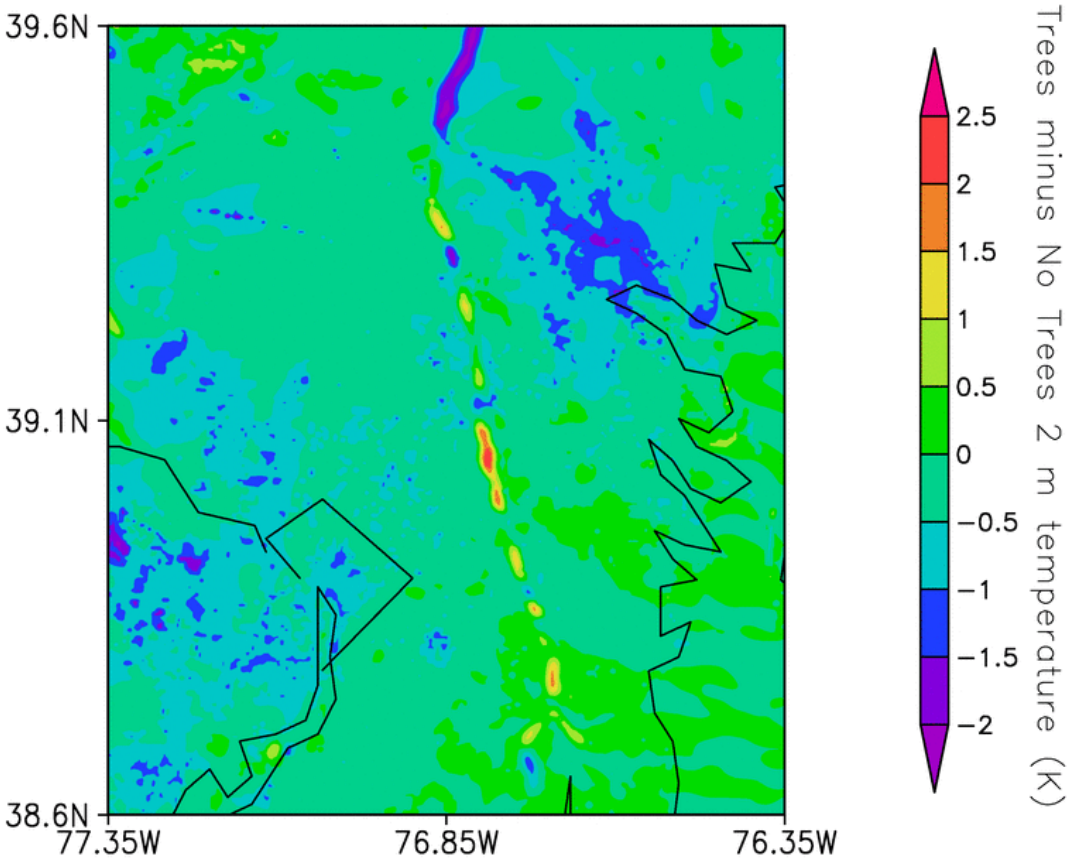

Figure 3-8: Trees minus No Trees simulated 2 m temperature with a horizontal resolution of 0.5 km at 2300 (6 PM EST) UTC 9 July 2007.

Urban trees are seen to impact the strength of the Chesapeake Bay breeze. Figures 3-7 and 3-8 show the change in temperature associated with trees at 3 PM and 6 PM, respectively. The most striking feature is a thin line of warmer temperatures in the Trees simulation than the No Trees simulation running north-south between Washington, DC and Baltimore, MD. Northwest of Baltimore, MD this thin line switches sign. At 2300 UTC the thin line shows warmer temperatures by up to 2 K in the Trees simulation than the No Trees simulation between Washington, DC and Baltimore, MD, but cooler temperatures by 2 K northwest of Baltimore, MD (Figure 3-8). This thin line is due to differences in the positioning of the Chesapeake Bay breeze convergence zone.

Differences in wind velocities north of Baltimore at 2000 UTC reveal a stronger bay breeze that penetrates further inland in the Trees simulation than the No Trees simulation (Figure 3-9). Wind velocity differences at 2300 UTC between Washington, DC and Baltimore, MD show a weaker bay breeze in the Trees simulation than the No Trees simulation (Figure 3-10). High temperatures due to the Washington, DC UHI propagating downwind near the coastline of the Chesapeake Bay strengthen the temperature gradient along the Chesapeake Bay coastline and therefore strengthen the bay breeze. The addition of urban trees dampens the urban heat island causing a weaker temperature gradient along the coastline and a weaker bay breeze that does not penetrate as far inland downwind of Washington, DC. So, the thin line of warmer temperatures in the Trees simulation shown in Figures 3-7, 3-8, and 3-10 is due to a weaker bay breeze that does not push the cooler air originating over the water as far inland. On the other hand, urban trees can amplify the bay breeze after being pushed through an urban area. The dampened UHI in Baltimore, MD due to urban trees when Baltimore, MD was on the cool side of the bay breeze, amplified the temperature gradient. The stronger temperature gradient caused the bay breeze to push further inland than the No Trees simulation as shown by the thin line of cooler temperatures northwest of Baltimore (Figures 3-7, 3-8, and 3-9).

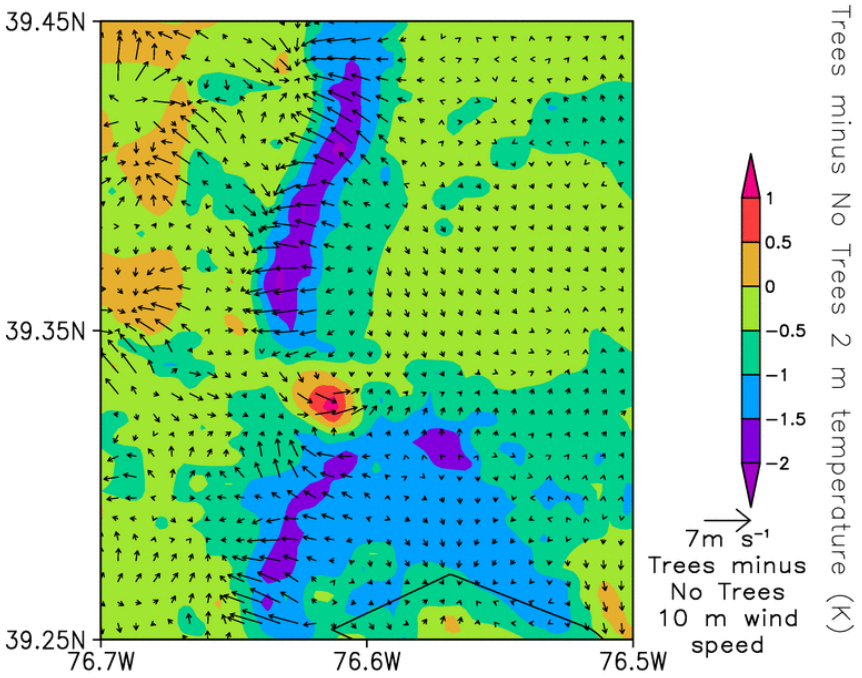

Figure 3-9: Trees minus No Trees simulated 2 m temperature and 10 m wind speed with a horizontal resolution of 0.5 km covering the bay breeze convergence zone north of Baltimore, MD at 2000 (3 PM EST) UTC 9 July 2007.

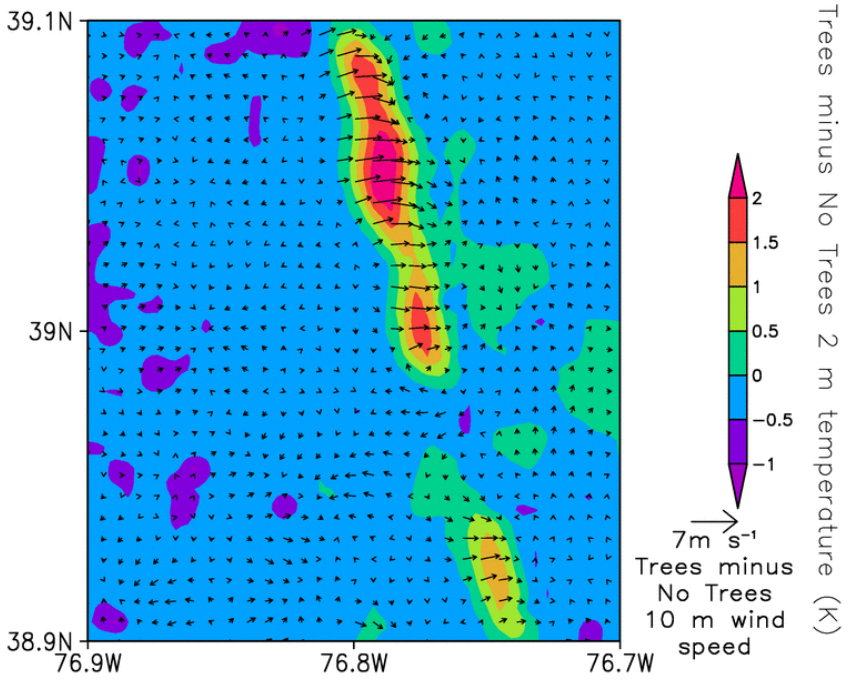

Figure 3-10: Trees minus No Trees simulated 2 m temperature and 10 m wind speed with a horizontal resolution of 0.5 km covering the bay breeze convergence zone between Washington, DC and Baltimore, MD at 2300 (6 PM EST) UTC 9 July 2007.

As mentioned previously, the impact of planting trees in all urban areas in the domain is larger in Baltimore, MD than Washington, DC. Since the bay breeze is stronger over and downwind of Baltimore in the Trees simulation than the No Trees simulation after the bay breeze convergence zone passes through Baltimore, more air originating over the cool surface waters is transported to Baltimore. So, cooler temperatures over Baltimore in the Trees simulation than the No Trees simulation are due to more evapotranspiration and shading from the added vegetation and a stronger bay breeze transporting cooler air over Baltimore at a faster rate.

There are significant urban temperature differences on the subgrid scale. Figure 3-11 shows building roof, building wall, and road surface temperatures as well as street canyon air temperature averaged over all urban buildings, roads, and street canyons for the three simulations. The roof surface temperatures vary little between the three simulations because the roofs for both the No Trees and No Trees Shorter Buildings simulations are not shaded and only the low-intensity residential roofs in the Trees simulations are partially shaded at low solar zenith angles. The No Trees Shorter Buildings simulation's maximum daytime building wall and road surface temperatures and maximum canyon air temperature are 1.9, 2.4, and 1.5 K greater than the No Trees simulation's temperatures on July 9 due to more shading from the buildings. On the other hand, the No Trees Shorter Buildings simulation's minimum nighttime building wall and road surface temperatures and minimum canyon air temperature are 0.4, 0.6, and 0.6 K lower than the No Trees simulation's temperatures between sunset on 8 July and sunrise on 9 July due to less longwave radiative trapping in the urban canyon. The Trees simulation's maximum building wall and road surface temperatures and maximum canyon air temperature are 8.9, 15.4, and 4.1 K lower than the No Trees simulation's temperatures on July 9 due to tree shading and evapotranspiration. The Trees simulation's minimum wall and road surface temperatures and canyon air temperature are 3.1, 3.2, and 2.5 K lower than the No Trees simulation's temperatures during the night of July 8.

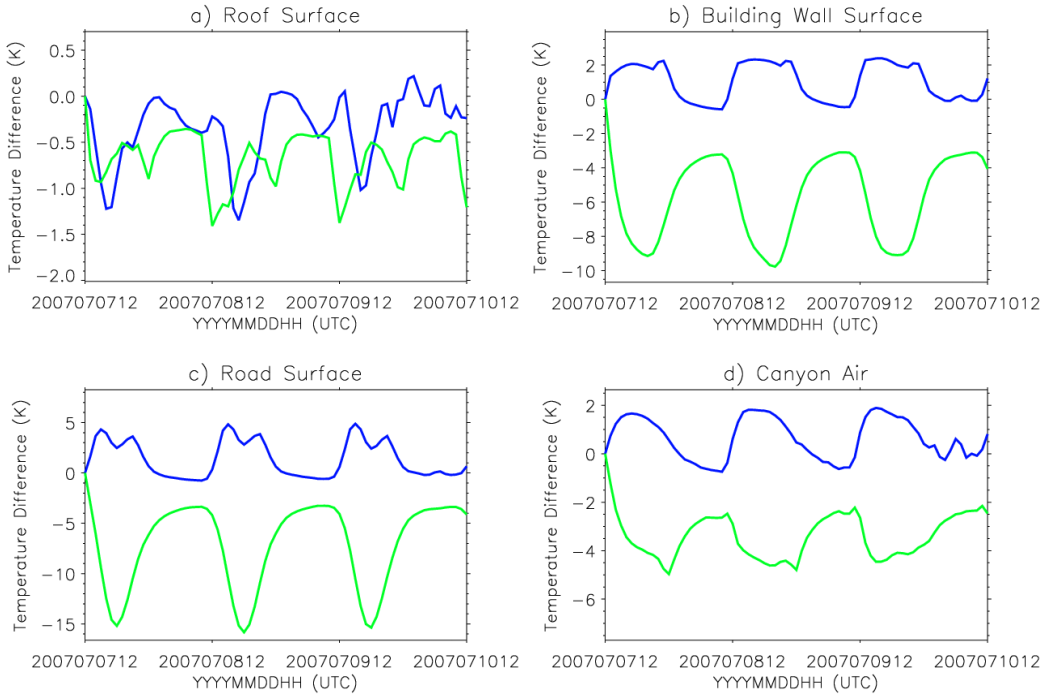

Figure 3-11: Timeseries of No Trees Shorter Buildings minus No Trees (blue), and Trees minus No Trees (green) simulated subgrid a) roof, b) building wall, and c) road surface temperatures and d) canyon air temperature with a horizontal resolution of 0.5 km averaged over all urban land use categories.

3.4 Conclusions and future directions

In this study, the role of urban trees and building height in UHI effects are investigated by performing simulations with the WRF-UCM and a modified version of WRF-UCM including the parameterized effects of urban trees, soil, and grass. Results show that urban areas with shorter buildings have a diurnal cycle of large amplitudes. Shorter urban buildings cause higher surface and near surface air temperatures during the daytime due to less building shading and lower temperatures at night due to less longwave radiative trapping in urban street canyons. In the model simulations, decreasing building size resulted in maximum daytime urban canyon air temperature to increase by 1.5 K and minimum nighttime urban canyon air temperature to decrease by

0.6 K. Urban trees result in lower surface and near surface air temperatures due to tree shading and evapotranspiration. The addition of trees in the simulations caused maximum daytime and minimum nighttime urban canyon air temperatures to decrease by 4.1 and 2.5 K, respectively. Future investigations will look into how these temperature differences due to varying building height and urban vegetation cover influence emissions, climate, and air quality.

Urban trees alter the strength of the Chesapeake Bay breeze by altering the temperature gradient near the coastline. Urban trees downwind of the Chesapeake Bay breeze dampen the strength of the breeze and therefore suppress the penetration of the bay breeze inland. The urban trees decrease the near surface air temperature over the warm land and therefore decreases the temperature gradient between the warm air over land and relatively cool air over the water. However, after the bay breeze penetrates inland past Baltimore, MD, it is found that urban trees increase the strength of the bay breeze. The addition of urban trees in Baltimore, MD causes the temperature of the cool side of the bay breeze to decrease resulting in a stronger temperature gradient and bay breeze. Since the bay breeze can impact air quality, future research can examine how altering the bay breeze due to the addition of urban trees can impact air quality.

Since urban areas in the WRF-UCM only include impervious surfaces, buildings and roads, the WRF-UCM with trees can be used to simulate the meteorology under more realistic urban land surface coverage. The National Land Cover dataset used in this study is from 2001. Keeping urban tree fraction and building height datasets up to date is useful for initializing the WRF-UCM with trees given that the UHI is sensitive to these parameters.

WRF-UCM with trees can be used as a tool to investigate how vegetative land surface changes to urban areas impact many aspects of earth science. Results show that urban trees can lower surface and air temperatures in and downwind of cities and alter a bay breeze. Future studies will investigate how lower summertime building surface temperatures due to an increase in urban trees can result in less energy demand for cooling buildings, quantify the reduction in energy demand to a decrease in anthropogenic emissions, and determine the climate and air quality impact of urban trees. In addition, the WRF-UCM with trees can investigate how an increase in urban trees, grass, and soil impacts the hydrological cycle by decreasing runoff, increasing evapotranspiration, and their effects on precipitation in and downwind of cities.

Chapter 4: Impact of urban trees on air quality

4.1 Introduction

High temperatures are associated with sunny skies, high pressure, subsidence, and weak winds. Chemically, high temperatures lead to faster reaction rates, greater biogenic and anthropogenic emissions and favor dissociation of peroxyacetyl nitrate (PAN) into.nitrogen dioxide (NO2), an ozone precursor. Therefore a positive correlation exists between observed air pollution and temperatures (Bloomer et al., 2009; Bloomer et al., 2010; Tai et al., 2010; U.S. EPA, 2006). Air quality model simulations agree that air pollution events are amplified with increasing temperatures (Weaver et al., 2009; Banta et al., 1998; Cheng and Byun, 2008; Jacob and Winner, 2009).

Urbanization can increase temperatures, and therefore exacerbate air pollution events. Creating impervious urban surfaces causes increased runoff, decreased evapotranspiration, increased solar radiation absorption, additional release of anthropogenic heat, and changes in surface friction (e.g., Oke, 1987; Bornstein and Lin, 2000; Arnfield, 2003). Previous studies show that rural to urban temperature differences are amplified as city size and building density increase (Oke, 1973; Landsberg, 1981; Atkinson, 2003; Imhoff et al., 2010). However, Zhang et al. (2009; 2011) show that UHI effects are not necessarily proportional to city size or building density as the effects from one city can be advected over another city. They show that the UHI effects over Baltimore, MD can be larger than the UHI effects over Washington, DC, a larger city than Baltimore, when Washington is upwind of Baltimore.

Urban trees can dampen the UHI and decrease near-surface air and building surface temperatures through direct shading and evaporative cooling. This cooling may result in lower air pollution levels. A change in temperature can also alter local weather patterns. For example, planting trees in a coastal city can alter a sea breeze as discussed in Chapter 3

A sea breeze circulation can exacerbate air pollution levels (Boucouvala and Bornstein, 2003; Evytugina et al., 2006). In Houston, high ozone episodes begin when the large scale flow is offshore before the onset of a bay breeze develops (Banta et al., 2005; Darby, 2005). As the bay breeze begins to strengthen, stagnant conditions develop allowing ozone and ozone precursors to accumulate before being advected further onshore as the bay breeze increases in intensity later in the afternoon (Banta et al., 2005; Darby, 2005). A change in the strength of a sea, bay, or lake breeze due to planting urban trees can therefore potentially alter air quality.

Trees can act to remove pollutants from the air, but also emit trace gases. Air pollutants can be deposited on trees, decreasing air pollution levels in the atmosphere. On the other hand, trees emit biogenic volatile organic compounds (VOCs), which can oxidize to form secondary organic aerosols (SOAs) or react in the presence of nitrogen oxides to form ozone, two secondary pollutants harmful to human health. Choi and Ehrman (2003) found that biogenic VOCs contribute significantly to ozone production in the Baltimore area during high ozone episodes.

In Hong Kong, a 1°C increase in monthly ambient temperature increases electricity consumption by 9.2, 3.0, and 2.4% in the domestic, commercial, and industrial sectors, respectively (Fung et al., 2006). Therefore cooler summertime surface wall and

roof temperatures of urban buildings associated with planting trees reduce energy demand on the electrical grid and anthropogenic emissions. Therefore decreasing anthropogenic emissions helps dampen climate change and improve air quality.

Herein, I show how the WRF-UCM with trees can be used as a tool to investigate how urban tree cover changes can affect air quality. In the present study, I examine how air quality can be altered by meteorological changes and biogenic emissions changes due to the addition of urban trees. This work does not include the impact of reductions in anthropogenic emissions on air quality due to planting urban trees. Future research will investigate how cooling building surface walls and roofs reduces electrical demand and anthropogenic emissions. The stated objectives are accomplished by performing air quality model simulations down to a horizontal resolution of 0.5 km. Model simulations are performed for the following three cases: (1) a No Trees case which includes meteorology and emissions for urban areas with no trees; (2) a Trees case which includes meteorology for an urban area with urban trees but no biogenic emissions from urban trees; and (3) a Trees Altered Emissions case which includes meteorology for an urban area with urban trees and biogenic emissions from the urban trees. Ash trees are used for the urban trees, which are low VOC emitters. At 30°C, ash trees emit 290 times less isoprene and 2 times less monoterpenes than oak trees, which are high VOC emitters. The simulations cover the Washington-Baltimore metropolitan areas from 1200 UTC 7 to 1200 UTC 10 July 2007. High air pollution was observed in the region alongside hot, sunny, stagnant conditions. A cold front passed through the area on 6 July 2007, followed by an anticyclone approaching the Mid-Atlantic states. A bay breeze was present during the daytime on July 7, 8, and 9. The Baltimore, MD UHI exhibited a 2 m

temperature of 37.5°C and downwind of Baltimore near-surface 8 h maximum ozone mixing ratios reached 125 ppb (the current air quality standard is 75 ppb) on July 9. This same time period was analyzed to investigate the impact of upstream urbanization on the UHI (Zhang et al., 2009; Zhang et al., 2011), characterize the air pollution event (Yegorova et al., 2011), and examine the impact of fair-weather cumulus clouds and the Chesapeake Bay breeze on air quality (Loughner et al., 2011).

4.2 Model description

The No Trees and Trees modeling scenarios performed with the Weather Research and Forecasting model coupled with an Urban Canopy Model (WRF-UCM) discussed in Chapter 3 are used to investigate how local and downwind weather modifications due to planting urban trees impacts air quality. The WRF-UCM output is fed into Version 4.6 of the Environmental Protection Agency's (EPA) Community Multiscale Air Quality (CMAQ) model (Byun and Schere, 2006) via the Meteorology-Chemistry Interface Processor (MCIP) (Otte and Pleim, 2010). Emissions input files for CMAQ are created with the Sparse Matrix Operator Kernel Emissions (SMOKE) modeling system (Houyoux and Vukovich, 1999).

4.2.1 Meteorological post-processing

MCIP Version 3.4 was used to ingest the WRF-UCM outputs and create input files for processing emissions data and running air chemistry simulations. As mentioned in Chapter 2, this step requires modifying MCIP to write out the percentage of each WRF-UCM grid cell that is urban. This urban fraction information is used in CMAQ to calculate vertical diffusion. This model update is available beginning in Version 3.5_beta of MCIP.

MCIP calculates the dry deposition velocity of gaseous species, which is then used in CMAQ to calculate pollutant removal from the atmosphere. MCIP uses the Models-3 Dry deposition velocity scheme (M3Dry) as described in Pleim et al. (2001), Byun and Ching (1999), and Otte and Pleim (2010). Four parameters used to calculate dry deposition velocities, a minimum stomatal resistance, leaf area index, vegetation fraction, and soil moisture in the root zone, are functions of landuse. MCIP was modified to scale these variables for the three urban categories for both the No Trees and Trees cases by:

$$X_{notrees} = X_{urban} \times f_{urban} + X_{USGS\_crop/grass} \times (1 - f_{urban}) \quad \text{(Equation 4-1),}$$

$$X_{trees} = X_{urban} \times f_{urban} \times (1 - f_{lu}) + X_{USGS\_decid\_broadleaf} \times f_{urban} \times f_{lu} + X_{USGS\_crop/wood} \times 0.5 \times (1 - f_{urban}). \quad \text{(Equation 4-2).}$$

Here $X_{notrees}$, X_{trees}, $X_{USGS\_crop/grass}$, $X_{USGS\_decid\_broadleaf}$, $X_{USGS\_crop/wood}$, and X_{urban} represent either minimum stomatal resistance, leaf area index, vegetation fraction, or soil moisture for a No Trees urban grid cell, Trees urban grid cell, USGS landuse type cropland / grassland mosaic, USGS landuse type deciduous broadleaf, USGS landuse type cropland / woodland mosaic, or a grid cell that is 100% urban, respectively. The formula for X_{urban} is:

$$X_{urban} = \frac{X_{USGS\_urban} - X_{USGS\_crop/grass} \times (1 - f_{USGS\_urban})}{f_{USGS\_urban}} \quad \text{(Equation 4-3),}$$

where f_{USGS_urban} is the urban fraction for USGS landuse type urban and X_{USGS_urban} represents either minimum stomatal resistance, leaf area index, vegetation fraction, or soil moisture for USGS landuse type urban. Here, USGS landuse type urban has an urban

fraction of 0.9 and the remaining landuse is USGS landuse type cropland / grassland mosaic. f_{lu} is the tree coverage fraction in the urban area and is set to 0.25 to account for trees in the street canyons. f_{urban} is the urban fraction and is set to 0.95, 0.9, and 0.5 for urban landuse type commercial/industrial/transportation, high-intensity residential, and low-intensity residential, respectively. The first term on the right hand side in the equation for the parameters for the No Trees case represents the portion of the grid cell that is urban, while the second term represents the non-urban area of the grid cell. The first term on the right hand side in the equation above for the Trees case represents the urban area with no tree coverage, the second term represents the tree covered urban streets, and the third term represents the non-urban portion of the grid cell with a 50% tree coverage.

4.2.2 Emissions

Emissions input files are created with SMOKE using the same methodology as described in Chapter 2. An interim 2007 emissions inventory from the U.S. Regional Planning Organizations (RPOs) is available. The interim 2007 emissions inventory is used instead of the projected 2009 emissions inventory which was utilized in Chapter 2. The interim 2007 inventory consists of actual 2007 point source emissions and interpolated area source emissions from existing 2002 and 2009 inventories. The 2007 emissions inventory has 1.2 times more NO_x than the projected 2009 inventory.

Biogenic emissions are created with the Biogenic Emissions Inventory System (BEIS) Version 3.12 coupled within SMOKE and are dependent on the meteorology and landuse (Vukovich and Pierce, 2002). The landuse data, which is created with the MIMS Spatial Allocator as described in Chapter 2, is modified to be consistent with the three

categories of urban landuse for the Trees and No Trees simulations. Ash trees, which are low biogenic volatile organic compound (VOC) emitters that are favorable urban trees found in the Mid-Atlantic, are chosen for the urban tree species used in the Trees Altered Emissions case.

4.2.3 Air quality model description

The CMAQ model is used to investigate the impact of changes in biogenic emissions and meteorology due to urban trees on air quality. . The model is run with the same user options and chemical initial and boundary conditions as described in Chapter 2. CMAQ is run with 32 vertical levels with 20 layers in the lowest 2 km. The 13.5 km resolution domain simulation begins 2 weeks prior to 1200 UTC 7 July 2007 to spin up the chemistry of the atmosphere for the species that are not available from global model output files used for chemical initial conditions.

4.3 Results

The three CMAQ model simulations, No Trees, Trees, and Trees Altered Emissions, at horizontal resolutions of 0.5 km are analyzed alongside observations to investigate how meteorological changes due to planting urban trees and biogenic emissions from urban trees impacts air quality. The impact of adding trees to removing atmospheric pollutants through dry deposition and adding more sources of biogenic VOC emissions are explored.

Due to changes in the surface properties and local meteorology in the urban areas, dry deposition processes of chemical species are altered. The dry deposition velocities altered for the Trees and Trees Altered Emissions cases as described in Section 4.2.1 with Equations 4-1, 4-2, and 4-3 are shown in Table 4-1. The added urban trees cause more

air pollutants to be removed from the atmosphere. For example, averaged over the 72 hour simulation in the commercial/industrial/transportation urban grid cells, the dry deposition velocities of O_3, NO, NO_2, HONO, and HCHO are faster with urban trees by 21, 5, 14, 32, and 51%.

		No urban trees	Urban trees
O_3 (cm / s)	LI	0.28	0.30
	HI	0.27	0.30
	C	0.24	0.29
NO (cm / s)	LI	0.062	0.064
	HI	0.62	0.065
	C	0.060	0.063
NO_2 (cm / s)	LI	0.15	0.15
	HI	0.14	0,15
	C	0.13	0.15
HONO (cm / s)	LI	0.38	0.44
	HI	0.37	0.45
	C	0.33	0.43
HCHO (cm / s)	LI	0.32	0.41
	HI	0.30	0.41
	C	0.27	0.41

Table 4-1: Average dry deposition velocities of O_3, NO, NO_2, HONO, and HCHO in the three urban categories (low-intensity residential (LI), high-intensity residential (HI), and commercial/industrial/transportation (C)) with and without urban trees.

Ash trees, which are low VOC emitters, are used for the urban trees. Emissions from urban trees are included in the Trees Altered Emissions case, while the No Trees and Trees cases do not include urban tree emissions. The Trees Altered Emissions case has more biogenic emissions of terpenes in the low-intensity residential, high-intensity residential, and commercial/industrial/transportation urban grid cells and more biogenic emissions of isoprene in the high-intensity residential and commercial/industrial/transportation urban grid cells (Table 4-2). Biogenic emissions are a function of temperature. Even though the Trees Altered Emissions case include more

sources of biogenic emissions of isoprene due to the urban trees, the lower temperatures in the low-intensity residential urban grid cells yield lower isoprene emissions.

	Isoprene (kg / day)			Terpenes (kg / day)		
	LI	HI	C	LI	HI	C
No urban trees	1088	81	110	2069	219	316
Urban trees	1050	91	128	2260	242	345

Table 4-2: Daily average biogenic emissions of isoprene and terpenes in the three urban categories (low-intensity residential (LI), high-intensity residential (HI), and commercial/industrial/transportation (C)) with and without urban trees.

Model simulated 8-h maximum ozone concentrations on 9 July 2007 for the No Trees, Trees, and Trees Altered Emissions cases are analyzed alongside observations (Figure 4-1). The model simulations have a low bias along the northern coast of the Chesapeake Bay, but a high bias northwest of Baltimore, MD. These biases are due to the model simulating southerly winds in the morning and early afternoon, while observations reveal westerly winds at this time (Figure 4-2). This result causes the model to simulate pollutants emitted in the Washington, DC metropolitan region to be transported north-northeastward to the area of high model simulated ozone concentrations instead of further eastward toward the Chesapeake Bay.

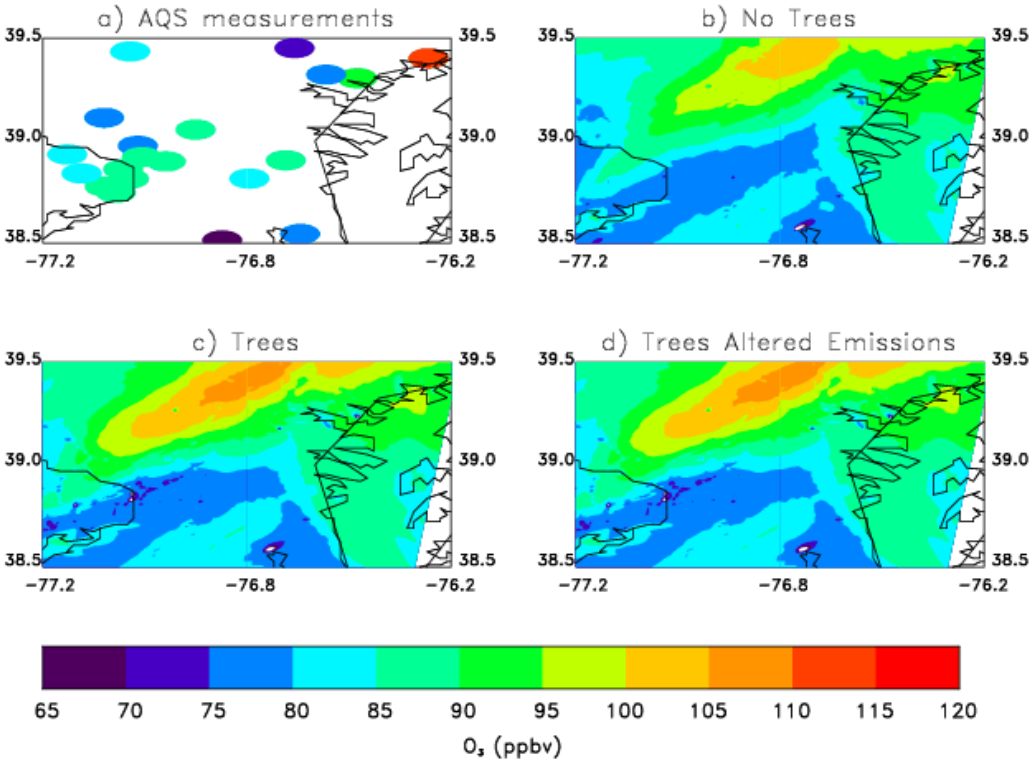

Figure 4-1: 8-h maximum ozone concentrations (ppbv) from a) EPA's Air Quality System (AQS) observations and the b) No Trees, c) Trees, d) Trees Altered Emissions cases on 9 July 2007.

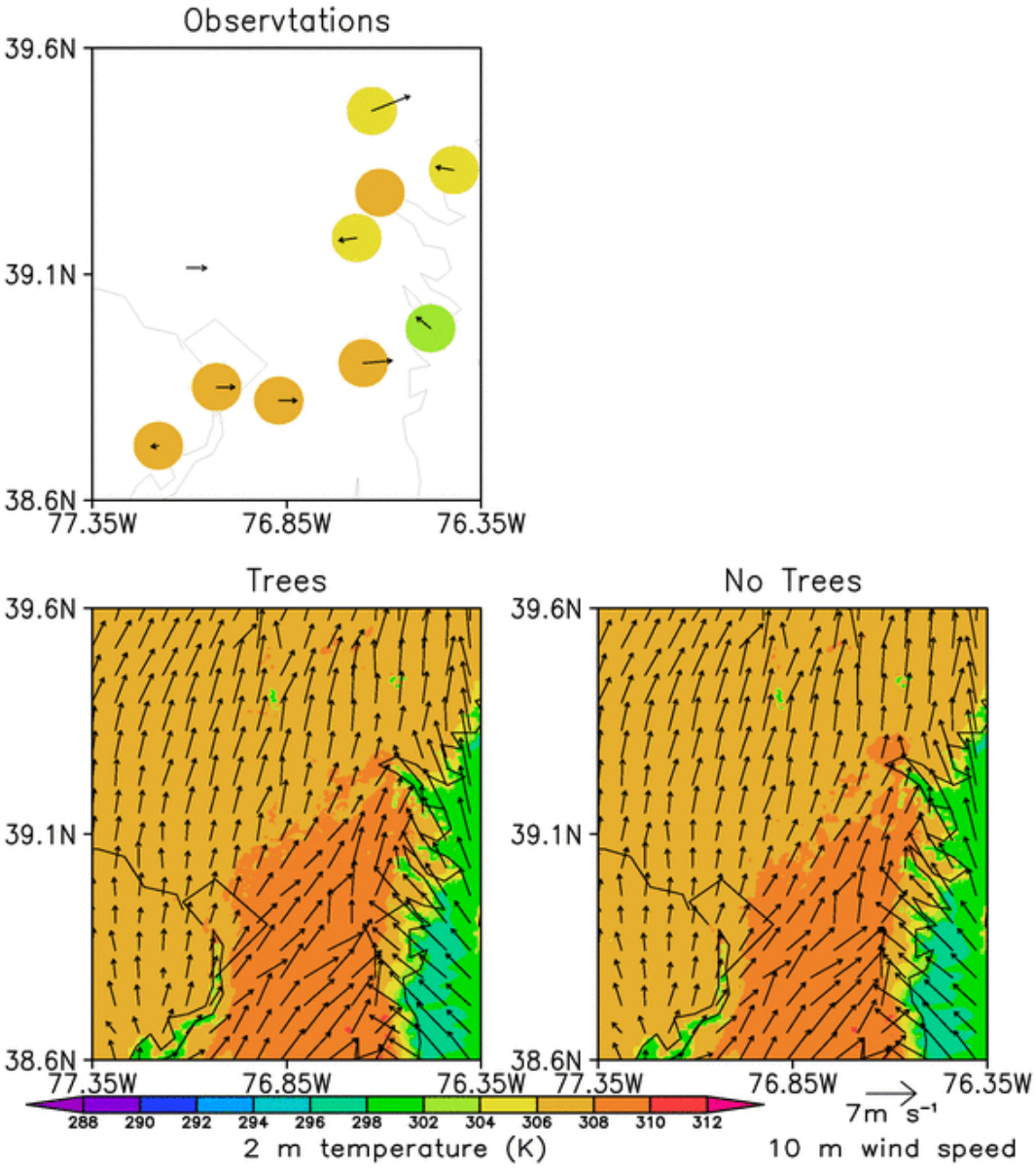

Figure 4-2: Observed and simulated 2 m temperature and 10 m wind speed at 1600 UTC (11 AM EST) 9 July 2007.

The Trees and Trees Altered Emissions model runs simulated higher ozone concentrations than the No Trees simulation. The peak simulated 8-h maximum ozone concentration for the Trees case is 3 ppb higher than the No Trees simulation. Lower surface temperatures in and downwind of urban areas in the Trees simulation contributes

to lower PBL heights compared to the No Trees simulation. The shallower PBL causes higher pollutant concentrations by volume in the PBL in the Trees simulation (Figure 4-3). The PBL height at 2100 UTC 9 July averaged over 900 km^2 at 39.31° latitude -76.87° longitude, an area of high ozone concentrations west of Baltimore, in the No Trees and Trees simulations is 1.73 and 1.68 km, respectively. Higher ozone concentrations in the Trees and Altered Trees simulations than the No Trees simulation northwest of Baltimore may also be due to a stronger simulated bay breeze. As discussed in Chapter 3, added trees in Baltimore strengthened the bay breeze after the bay breeze convergence zone passes through Baltimore. A stronger bay breeze that penetrates further inland may result in more pollutants converging and accumulating at the bay breeze convergence zone.

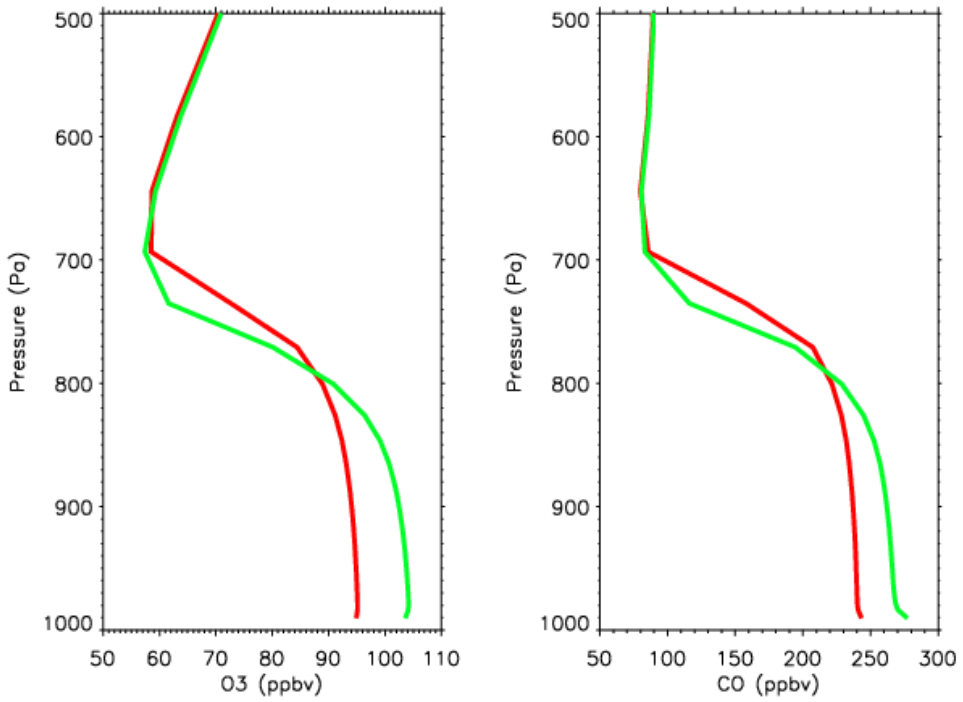

Figure 4-3: O_3 (left) and CO (right) profiles for the No Trees (red) and Trees (green) simulations averaged over 900 km^2 at 39.31° latitude -76.87° longitude at 2100 UTC (4 PM EST) 9 July 2007. Maximum differences in ground-level ozone concentrations in the simulation is found in this area and at this time.

As shown in Figure 4-1, there are little differences in simulated 8-h maximum ozone concentrations between the Trees and Trees Altered Emissions cases even though the VOC emissions differ. The peak 8-h maximum ozone concentration of the Trees Altered Emissions simulation is only 0.005 ppb higher than the Trees case. The small difference in ozone concentrations could be due to the region being NO_x limited. This means a change in VOC concentrations will have little impact on ozone formation, but a change in NO_x concentrations will alter the rate of ozone formation. The small difference between the two simulations may also be due to the use of low VOC emitting trees instead of high VOC emitting trees like Oak trees.

4.4 Conclusions

In this study, I demonstrate how the WRF-UCM with trees can be used to investigate how urban vegetation changes affect air quality. CMAQ simulations are used to investigate how meteorological changes due to planting urban trees impacts air quality during a high air pollution episode in the Mid-Atlantic. The impact of additional biogenic VOC emissions due to low VOC emitting urban trees on air quality is shown to have little impact on ozone formation. For this particular modeling scenario, the model simulations with urban trees results in a shallower PBL, which results in higher pollutant concentration in the PBL. However, the changes in PBL depth are too small to explain much of the increase in surface layer pollutant concentrations. It appears that urban trees strengthen the Chesapeake Bay breeze, which causes a buildup of pollutants near the Chesapeake Bay Breeze convergence zone. This unexpected result may not be robust as it was obtained from a model simulation of one pollution episode.

Additional research is needed to fully gain an understanding on how urban trees impact air quality. Urban trees can alter meteorology, deposition, biogenic emissions, and anthropogenic emissions, all of which impact air quality. Gaining an understanding on how cooling urban building walls and roofs with urban trees impacts electrical demand and anthropogenic emissions is needed. Incorporating this information in air quality model simulations will help achieve the goal of determining how urban trees affect air quality. In addition, further research is needed on the sensitivity of sea breeze circulations to the distribution of trees. Further research can also investigate how different types of urban trees impacts ozone concentrations.

Chapter 5: Conclusions

5.1 Research summary

Interactions among meteorology, land surface processes, and atmospheric chemistry were examined, and the impact of model resolution on meteorological and air quality simulations was explored. I found that as model resolution increases, (i) more sulfur dioxide is transported through fair weather cumulus clouds causing faster sulfate formation, (ii) more pollutants are vented from the PBL to the free troposphere, (iii) more pollution accumulates in a convergence zone with weak surface winds west of the Chesapeake Bay, and (iv) a stronger bay breeze forms preventing pollutants from being transported across the coastline near the surface but instead the pollutants are lofted before being transported downwind. These results improve our understanding of air quality and climate. Sulfate aerosols are harmful to human health and play a role in scattering radiation as well as impact cloud and precipitation processes. Transporting pollutants from the PBL to the free troposphere, even the lower free troposphere, increases their lifetime and the distance they can travel (Taubman et al., 2004). This causes the pollutants to have a larger impact on climate and be able to impact air quality further downwind. A stronger simulated bay breeze produces higher and more realistic 8-h maximum ozone concentrations at locations near the Bay Breeze convergence zone and lower concentrations over the surface of the Chesapeake Bay.

Differences in the cloud parameters used in CMAQ's aqueous chemistry and photolysis schemes were analyzed. The photolysis clouds agreed better with observations during the three day modeling time period by producing more cloud cover.

This resulted in more sulfur dioxide oxidation to form sulfate aerosols and shows the importance of accurately modeling the spatial coverage of clouds in model sulfate aerosol concentrations. It is also important to accurately model clouds and transport processes through clouds. Pollutants can be lofted and vented through clouds into the free troposphere.

Building heights and urban trees affect near surface air temperature and building wall and roof surface temperatures. Shorter buildings cause less direct shading of streets and adjacent building walls, which results in higher daytime air and surface temperatures. On the other hand, shorter buildings trap less longwave radiation in urban street canyons, allowing more radiative cooling and causing lower nighttime temperatures. Urban trees provide cooling through shading and evapotranspiration. Urban trees near coastlines can alter a sea, bay, or lake breeze. The model suggests that planting trees in Washington, DC could decrease the temperature gradient along the coastline causing a weaker Chesapeake Bay breeze. However, urban trees in Baltimore, MD might amplify the bay breeze. Once the bay breeze convergence zone is inland past Baltimore with Baltimore on the cool side of the bay breeze, the addition of urban trees causes lower temperatures on the cool side of the bay breeze. This magnifies the temperature gradient along the convergence zone and the strength of the bay breeze.

Urban trees can impact air quality by emitting biogenic VOCs, removing pollutants from the atmosphere, and decreasing surface temperatures. It was shown how the WRF-UCM with trees can be used to examine how urban vegetation changes impact air quality. For one particular modeling scenario, adding urban trees to Washington, DC and Baltimore, MD resulted in lower PBL heights, a stronger bay breeze northwest of

Baltimore, and higher surface ozone concentrations. This modeling scenario did not include the impact of anthropogenic emissions reductions associated with the additional urban trees. Cooler surface temperatures from adding trees results in lower anthropogenic emissions, which is expected to decrease air pollution.

5.2 Recommendations for further research

It is difficult to simulate or parameterize fine spatial scale features, such as fair-weather cumulus clouds and bay breezes, at coarse model resolutions. However, it is impractical to run model simulations at a horizontal resolution of 0.5 km for many projects due to computational restraints. Results discussed above suggest vertical diffusion schemes for coarse simulations should be modified to produce faster vertical transport to allow more pollutants to be transported through clouds and across the top of the boundary layer. It is also shown that CMAQ's aqueous chemistry and photolysis schemes generate dramatically different cloud cover. These cloud properties need to be harmonized. To simulate a bay, sea, or lake breeze at resolutions coarser than 4.5 km, a bay, sea, or lake breeze parameterization needs to be developed. Otherwise, finer horizontal resolutions are needed along coastlines. This might be accomplished with nested simulations along coastlines or a stretched grid with the resolution increasing as the distance from the coastline decreases.

The impact of building height on the UHI was examined. Future work can look into how building depth and the width of street canyons impact the UHI. An urban tree canopy parameterization was developed and implemented into the WRF-UCM to study the effect of planting urban trees on temperatures and meteorology. Future work can look into how different tree planting strategies could influence temperatures and

meteorology. For example, instead of examining how planting urban trees uniformly along streets in urban cores and suburban neighborhoods, future work can look into how planting a high concentration of trees only in suburban neighborhoods affects the UHI. In addition, future WRF-UCM experiments can be performed to examine how replacing urban roofs with a more reflective surface affects the UHI.

Additional research is needed to determine how urban trees impact air quality and climate. Urban trees can alter meteorology, deposition, biogenic emissions, and anthropogenic emissions, all of which impact air quality. Future work is needed to learn how cooling building walls and roofs can decrease the electrical demand on utilities and anthropogenic emissions. Results from this work can then be incorporated in climate and air quality models to fully understand how urban trees impact the atmosphere.

Chapter 6: References

Annandale, J.G., N.Z. Jovanovic, G.S. Campbell, N. Du Sautoy, and P. Lobit, 2004. Two dimensional solar radiation interception model for hedgerow fruit trees, Agricultural and Forest Meteorology, 121, 207-225.

Atkinson, B.W., 2003. Numerical modeling of urban heat island intensity. Boundary Layer Meteorology, 109, 285-310.

Arnfield, A J., 2003. Two decades of urban climate research: A review of turbulence, exchanges of energy and water, and the urban heat island. International Journal of Climatology, 23, 1-26.

Banta, R., C. Senff, J. Nielsen-Gammon, L. Darby, T. Ryerson, R. Alvarez, P. Sandberg, E. Williams, and M. Trainer, 2005. A bad air day in Houston, Bulletin of the American Meteorological Society, 86, 657-669, doi: 10.1175/BAMS-86-5-657.

Bloomer, B. J., J. W. Stehr, C. A. Piety, R. J. Salawitch, and R. R. Dickerson, 2009. Observed relationships of ozone air pollution with temperature and emissions. Geophysical Research Letters, 36, L09803, doi:10.1029/2009GL037308.

Bloomer, B.J., R. R. Dickerson, and K. Vinnikov, 2010. A Chemical Climatology and Trend Analysis of Ozone and Temperature over the Eastern US, Atmospheric Environment, 44, 2543-2551.

Booker, F., R. Muntifering, M. McGrath, K. Burkey, D. Decoteau, E. Fiscus, W. Manning, S. Krupa, A. Chappelka, and D. Grantz, 2009. The ozone component of global change: Potential effects on agricultural an horticultural plant yield, product

quality and interactions with invasive species, Journal of Integrative Plant Biology, 51, 337-351.

Bornstein, R., and Q. L. Lin, 2000. Urban heat islands and summertime convective thunderstorms in Atlanta: Three case studies, Atmospheric Environment, 34, 507-516, doi:10.1016/S1352-2310(99)00374-X.

Boucouvala, D. and R. Bornstein, 2003. Analysis and transport patterns during an SCOS97-NARSTO episode, Atmospheric Environment, 37, #2 S73-S94.

Byun, D.W. and J.K.S. Ching, 1999. Science Algorithms of the EPA Models-3 Community Multiscale Air Quality (CMAQ) Modeling System, NERL, Research Triangle Park, NC, EPA/600/R-99/030.

Byun, D. and K.L. Schere, 2006. Review of the governing equations, computational algorithms, and other components of the Models-3 Community Multiscale Air Quality (CMAQ) modeling system, Applied Mechanics Review, 59, 51-77.

Byun, D.W., J.E. Pleim, R.T. Tang, and A. Bourgeois, 1999. Meteorology-Chemistry Interface Processor (MCIP) for Models-3 Community Multiscale Air Quality (CMAQ) Modeling System, in Science algorithms of the EPA Models-3 Community Multiscale Air Quality (CMAQ) Modeling System, EPA-600/R-99/030, pp. 12-1 - 12-90, U.S. Environmental Protection Agency, Washington, DC.

Campbell, G.S., Norman, J.M., 1998: An Introduction to Environmental Biophysics, 2nd ed. Springer, New York.

Castellanos, P., 2009. Analysis of temporal sensitivities and vertical mixing in CMAQ, and measurements of NO2 with cavity ring-down spectroscopy, Ph.D. Thesis,

Department of Chemical and Biomolecular Engineering, University of Maryland, College Park, MD, pp. 165.

Castellanos, P., L.T. Marufu, B.G. Doddridge, B.F. Taubman, J.J. Schwab, J.C. Hains, S.H. Ehrman, and R.R. Dickerson, 2011. Ozone, oxides of nitrogen and carbon monoxide during pollution events over the eastern US: An evaluation of emissions and vertical mixing, Journal of Geophysical Research (in press).

Chang, J.S., R.A. Brost, I.S.A. Isaksen, S. Madronich, P. Middleton, W.R. Stockwell, and C.J. Walcek, 1987. A three-dimensional Eulerian acid deposition model: Physical concepts and formulation, Journal of Geophysical Research, 92, 14681-14700.

Chameides, W.L., R.W. Lindsay, J. Richardson, C.S. Kiang, 1998. The Role of Biogenic Hydrocarbons in Urban Photochemical Smog: Atlanta as a Case Study, Science, 241, 1473-1475.

Chen F. and J. Dudhia, 2001. Coupling an advanced land-surface-hydrology model with the Penn State-NCAR MM5 modeling system. Part I: model implantation and sensitivity, Monthly Weather Review, 129, 569-585.

Cheng, Y. Y., and D. W. Byun, 2008. Application of high resolution land use and land cover data for atmospheric modeling in the Houston-Galveston metropolitan area, Part I: Meteorological simulation results. Atmospheric Environment, 42, 7795-7811.

Chicago Botanic Garden, 2001. Urban Trees and Shrubs - A guide to the selection of trees and shrubs in urban areas, last accessed March 1, 2011, http://www.na.fs.fed.us/spfo/pubs/uf/uts/index.htm.

Choi, Y.-D. and S.H. Ehrman, 2003. Investigation of sources of volatile organic carbon in the Baltimore area using highly time-resolved measurements, Atmospheric Environment, 38, 775-791.

Cohan, D.S., Y. Hu, and A.G. Russell, 2006. Dependence of ozone sensitivity analysis on grid resolution, Atmospheric Environment, 40, 126-135.

Colella P. and P.R. Woodward (1984). The piecewise parabolic method (PPM) for gas-dynamical simulations, Journal of Computational Physics, 54, 174-201.

Darby, L.S., 2005. Cluster analysis of surface winds in Houston, Texas, and the impact of wind patterns on ozone, Journal of Applied Meteorology, 44, 1788-1806, doi:10.1175/JAM2320.1.

Daum, P.H. 1990. Observations of H2O2 and S(IV) in air, cloudwater, and precipitation and their implications for the reactive scavenging of SO2, Atmospheric Research, 25, 89-102.

Docker, D.W., C.A. Pope, X. Xu, J.D. Spengler, J.H. Ware, M.E. Fay, B.G. Ferris, and F.E. Speizer, 1993. An association between air pollution and mortality in six U.S. cities, New England Journal of Medicine, 329, 1753-1759.

Dwyer, J.F. and D.J. Nowak, 2000. A national assessment of the urban forest: an overview. Proceedings of the Society of American Foresters 1999 National Convention, Portland, OR, 157-162.

Eatough, D.J., R.J. Arthur, N.L. Eatough, M.W. Hill, N.F. Mangelson, B.E. Richter, and L.D. Hansen, 1984. Rapid conversion of SO_2(g) to sulfate in a fog bank, Environmental Science and Technology, 18, 855-869.

Emmons, L.K., S. Walters, P.G. Hess, J.-F. Lamarque, G.G. Pfister, D. Fillmore, C. Granier, A. Guenther, D. Kinnison, T. Laepple, J. Orlando, X. Tie, G. Tyndall, C. Wiedinmyer, S.L. Baughcum, and S. Kloster, 2010. Description and evaluation of the Model for Ozone and Related chemical Tracers, version 4 (MOZART-4), Geoscientific Model Development 3, 43-67.

Evtyugina, M.G., T. Nunes, C. Pio, and C.S. Costa, 2006. Photochemical pollution under sea breeze conditions, during summer, at the Portuguese West Coast. Atmospheric Environment 40, 6277-6293.

Eyth, A.M. and B. Brunk, 2005. New features in Version 3 of the MIMS Spatial Allocator, paper presented at 4th Annual CMAS Models-3 Users' Conference, Chapel Hill, NC.

Finlayson-Pitts, B.J. and J.N. Pitts, 2000. Chemistry of the upper and lower atmosphere, Academic Press, San Diego, CA.

Fishman, J, J.K. Creilson, P.A. Parker, E.A. Ainsworth, G.G. Vining, J. Szarka, F.L. Booker, and X. Xu. 2010. An investigation of widespread ozone damage to the soybean crop in the upper Midwest determined from ground-based and satellite measurements, Atmospheric Environment 44, 2248-2256.

Fishman, J., V. Ramathan, P.J. Crutzen, and S.C. Liu, 1979. Tropospheric ozone and climate, Nature, 282, 818-820.

Galloway, J.N., J.D. Aber, J.W. Erisman, S.R. Seitzinger, R.W. Howarth, E.B. Cowling, and B.J. Cosby, 2003. The Nitrogen Cascade, Bioscience, 53, 341-356.

Gilliland, A.B., C. Hogrefe, R.W. Pinder, J.M. Godowitch, K.L. Foley, and S.T. Rao, 2008. Dynamic evaluation of regional air quality models: Assessing changes in O_3

stemming from changes in emissions and meteorology, Atmospheric Environment, 42, 5110-5123.

Godowitch, J.M. G.A. Pouliot, and S.T. Rao 2010. Assessing multi-year changes in modeled and observed urban NOX concentrations from a dynamic model evaluation perspective, Atmospheric Environment, 44 2894-2901.

Grell, G. A., and D. Devenyi, 2002. A generalized approach to parameterizing convection combining ensemble and data assimilation techniques, Geophysical Research Letters, 29, Article 1693.

Hains, J.C., 2007. A chemical climatology of lower tropospheric trace gases and aerosols over the Mid-Atlantic region, Ph.D. Thesis, Department of Atmospheric and Oceanic Science, University of Maryland, College Park, MD, pp. 254.

Hansen, J., M. Sato, and R. Ruedy, 1997. Radiative forcing and climate response, Journal of Geophysical Research, 102, 6831-6864.

Hogrefe, C., S.T. Rao, I.G. Zurbenko, and P.S. Porter, 2000. Interpreting the information in ozone observations and model predictions relevant to regulatory policies in the Eastern United States, Bulletin of the American Meteorological Society, 81, 2083-2106.

Houyoux, M., R. and J. M. Vukovich, 1999. Updates to the Sparse Matrix Operator Kernel Emissions (SMOKE) Modeling System and Integration with Models-3, paper presented at The Emission Inventory: Regional Strategies for the Future, Air and Waste Management Association, Raleigh, NC.

Imhoff, M.L., P. Zhang, R.E. Wolfe, and L. Bounoua, 2010. Remote sensing of the urban heat island effect across biomes in the continental USA, Remote Sensing of Environment, 114, 504-513.

Jacob, D.J. E.W. Gottlieb, and M.J. Prather 1989. Chemistry of a polluted cloudy boundary layer, Journal of Geophysical Research, 94, 12975-13002.

Jacob, D. J. and D. A. Winner, 2009. Effect of climate change on air quality, Atmospheric Environment, 43, 51-63.

Janjic, Z.I., 1994. The step-mountain eta coordinate model: further developments of the convection, viscous sublayer and turbulence closure scheme, Monthly Weather Review, 122, 927-945.

Jimenez, P., O. Jorba, R. Parra, and J.M. Baldasano, 2006. Evaluation of MM5-EMICAT2000-CMAQ performance and sensitivity in complex terrain: High-resolution application to northeastern Iberian Peninsula, Atmospheric Environment, 40, 5056-5072.

Klemp, J. B., J. Dudhia, and A. Hassiotis, 2008. An upper gravity wave-absorbing layer for NWP applications, Monthly Weather Review, 136, 3987-4004.

Kunkel, K. E., S.A. Changnon, B.C. Reinke, and R.W. Arritt, 1996. The July 1995 heat wave in the Midwest: A climatic perspective and critical weather factors. Bulletin of the American Meteorological Society, 77, 1507-1518.

Kusaka, M. and F. Kimura, 2004. Coupling a single-layer urban canopy model with a simple atmospheric model: Impact on urban heat island simulation for an idealized case, Journal of the Meteorological Society of Japan, 82, 67-80.

Kusaka H., H. Kondo, Y. Kikegawa, and F. Kimura, 2001. A simple single layer urban canopy model for atmospheric models: Comparison with multi-layer and slab models, Boundary-Layer Meteorology, 101, 329-258.

Landsberg, H.E., 1981. The urban climate. International Geophysics Series, 28, Academic Press, 288pp.

Lee, C., R.V. Martin, A. Donkelaar, H. Lee, R.R. Dickerson, J.C. Hains, N. Krotkov, A. Richter, K. Vinnikov, and J.J. Scwabb, 2011. SO2 emissions and lifetimes: Estimates from inverse modeling using in situ and global, space-based (SCIAMACHY and OMI) observations, Journal of Geophysical Research, 116, doi:10.1029/2010JD014758.

Lee, S.-H. and S.-U. Park, 2008. A Vegetated Urban Canopy Model for Meteorological and Environmental Modelling, Boundary-Layer Meteorology, 126:73-102.

Lim, K.-S.S. and S.-Y. Hong, 2010. Development of an effective double-moment cloud microphysics scheme with prognostic Cloud Condensation Nuclei (CCN) for weather and climate models, Monthly Weather Review, 138, 1587-1612.

Loughner, C.P., D.J. Allen, K.E. Pickering, R.R. Dickerson, D.-L. Zhang, and Y.-X. Shou 2011. Impact of the Chesapeake Bay breeze and fair-weather cumulus clouds on pollutant transport and transformation, Atmospheric Environment, accepted for publication.

Mass, C., D. Ovens, M. Albright, and K. Westrick, 2002. Does increasing horizontal resolution produce better forecasts?: The results of two years of real-time numerical weather prediction in the Pacific Northwest, Bulletin of the American Meteorological Society, 83, 407–430.

McGinn, C., 1982. Microclimate and Energy Use in Suburban Tree Canopies, Ph.D. Thesis, University of California, Davis, CA, pp. 299.

Moffat, A.S., 1998. Global nitrogen overload problem grows critical, Science, 279, 988-989.

Morgan, C. and N. Owens, 2001. Benefits of water quality policies: the Chesapake Bay, Ecological Economics, 39, 271-284.

Mudway, I.S. and F.J. Kelly, 2000. Ozone and the lung: a sensitive issue, Molecular Aspects of Medicine, 21, 1-48.

Mueller, S.F., E.M. Bailey, T.M. Cook, and Q. Mao, 2006. Treatment of clouds and the associated response of atmospheric sulfur in the Community Multiscale Air Quality (CMAQ) modeling system, Atmospheric Environment, 40, 6804-6820.

Norman, J.M. and J.M. Welles, 1983. Radiative transfer in an array of canopies, Agronomy Journal, 75, 481-488.

(NRC) National Research Council, 2006. Understanding Marine Biodiversity, Washington, DC, National Academy Press.

Odman, M.T. and Y. Hu, 2009. Georgia Institute of Technology, last accessed October 27, 2010, http://people.ce.gatech.edu/~todman/bugs/bugs.htm.

Oke, T.R., 1973. City size and the urban heat island, Atmospheric Environment, 7, 769-779, doi:10.1016/0004-6981(73)90140-6.

Oke, T.R., and H.A. Cleugh, 1987. Urban heat-storage derived as energy balance residuals, Boundary Layer Meteorology, 39, 233–245, doi:10.1007/BF00116120.

Otte, T. and J.E. Pleim, 2010. The Meteorological-Chemistry Interface Processor (MCIP) for the CMAQ modeling system: updates through MCIPv3.4.1, Geoscientific Model Development, 3, 243-256.

Pleim, J.E., 2007. A combined local and non-local closure model for the atmospheric boundary layer. Part 1: Model description and testing, Journal of Applied Meteorology and Climatology, 46, 1383-1395.

Pleim, J.E. and J. Chang, 1992. A non-local closure model for vertical mixing in the convective boundary layer, Atmospheric Environment, 26A, 965-981.

Pleim, J.E., A. Xiu, P.L. Finkleston, and T.L. Otte, 2001. A coupled land-surface and dry deposition model and comparison to field measurements of surface heat, moisture, and ozone fluxes. Water, Air, and Soil Pollution: Focus, 1, 243-25.

Rosenfeld D., 2000. Suppression of rain and snow by urban and industrial air pollution. Science, 287, 1793-1796.

Rosenfeld D. and A. Givati, 2006. Evidence of orographic precipitation suppression by air pollution-induced aerosols in the western United States, Journal of Applied Meteorology and Climatology, 45, 893-911.

Samet, J.M., F. Dominici, F.C. Curriero, I. Coursac, and S.L. Zeger, 2000. Fine particulate air pollution and mortality in 20 U.S. cities, 1987-1994, New England Journal of Medicine, 343, 1742-1749.

Sanders, G.E., J.J. Colls, and A.G. Clark, 1992. Physiological changes to Phaseolus vulgarisin response to long-term ozone exposure, Annals of Botany, 69, 123-133.

Shine, K.P., 2000. Radiative forcing of climate change, Space Science Reviews, 94, 363-373.

Shou, Y., and D.-L. Zhang, 2010. Impact of environmental flows on the urban daytime boundary layer structures over the Baltimore metropolitan region. Atmospheric Science Letters, 11, 1-6.

Skamarock, W.C., J.B. Klemp, J. Dudhia, D.O. Gill, D.L. Barker, M.G. Duda, X.-Y. Huang, W. Wang, J.G. Powers, 2008. A description of the Advanced Research WRF Version 3, NCAR Technical Note, NCAR/TN-475+STR, NCAR, Boulder, CO.

Sokhi, R.S., R. San Jose, N. Kitwiroon, E. Fragkou, J.L. Perez, D.R. Middleton, 2006. Prediction of ozone levels in London using the MM5-CMAQ modelling system, Environmental Modelling and Software, 21, 566-576.

Souch, C.A. and C. Souch, 1993. The effect of trees on summertime below canopy urban climates: a case study, Bloomington, Indiana, Journal of Arboroculture, 19:303-312.

Tai, A. P. K., L. J. Mickley, and D. J. Jacob, 2010. Correlations between fine particulate matter (PM2.5) and meteorological variables in the United States: Implications for the sensitivity of PM2.5 to climate change, Atmospheric Environment, 44, 3976-3984.

Taubman, B.F., J.C. Hains, A.M. Thompson, L.T. Marufu, B.G. Doddridge, J.W. Stehr, C.A. Piety, and R.R. Dickerson, 2006. Aircraft vertical profiles of trace gas and aerosol pollution over the mid-Atlantic United States: Statistics and meteorological cluster analysis, Journal of Geophysical Research, 111, D10S07, doi:10.1029/2005JD006196.

Taubman, B.F., L.T. Marufu, C.A. Piety, B.G. Doddridge, J.W. Stehr, R.R. Dickerson, 2004. Airborn characterization of the chemical, optical, and meteorological properties, and origins of a combined ozone-haze episode over the Eastern United States, Journal of Atmospheric Sciences, 61, 1781-1793.

Toon O.B., 2000. How Pollution Suppresses Rain. Science, 298, 794-799.

TreesNY and CENYC, Citizen Pruners, and USDA Forest Service Northeastern, Research Station, 2002. Neighborhood Tree Survey - Summary by Tree Species, last accessed March 1, 2011, http://www.oasisnyc.net/trees/downloads/sum-by-species.pdf.

Twomey, S., 1974. Pollution and the planetary albedo, Atmospheric Environment, 8, 1251-1256.

U.S. Environmental Protection Agency, 2006. Air Quality Criteria for Ozone and Related Photochemical Oxidants, Research Triangle Park, NC, National Center for Environmental Assessment, Office of Research and Development, report number EPA 600/R-05/004aF, available at http://www.epa.gov/ncea/isa/.

U.S. Environmental Protection Agency, 2003. User's Guide to MOBILE6.1 and MOBILE6.2: Mobile source emission factor model, EPA420-R-03-010, U.S. EPA National Vehicle and Fuel Emissions Laboratory, Ann Arbor, MI, pp. 262.

Vukovich, J. and T. Pierce, 2002. The Implementation of BEIS-3 within the SMOKE modeling framework, Presented at Emissions Inventories – Partnering for the Future, paper presented at the 11th Emissions Inventory Conference of the U.S. Environmental Protection Agency, Research Triangle Park, NC.

Wallace, J.M. and P.V. Hobbs, 1997. Atmospheric science an introductory survey. Academic Press, San Diego, CA.

Weaver, C. P., E. Cooter, R. Gilliam, A. Gilliland, A. Grambsch, D. Grano, B. Hemming, S.W. Hunt, C. Nolte, and D.A. Winner, 2009. A Preliminary Synthesis of Modeled Climate Change Impacts on Us Regional Ozone Concentrations, Bulletin of the American Meteorological Society, 90, 1843-1863.

Weijers, E. P., A. Y. Khlystov, G. P. A. Kos, and J. W. Erisman, 2004. Variability of particulate matter concentrations along roads and motorways determined by a moving measurement unit. Atmospheric Environment, 38, 2993-3002.

Yarwood, G., S. Rao, M. Yocke, and G.Z. Whitten, 2005. Updates to the Carbon Bond Mechanism: CB05, RT-0400675, U.S. Environmental Prediction Agency, Washington, DC.

Yegorova, E.A., D.J. Allen, C.P. Loughner, K.E. Pickering, and R.R. Dickersion, 2011. Characterization of an eastern U.S. severe air pollution episode using WRF/chem., Journal of Geophysical Research (in final review).

Yu, S., R. Mathur, G. Sarwar, D. Kang, D. Tong, G. Pouliot, and J. Pleim, 2010. Eta-CMAQ air quality forecasts of O_3 and related species using three different photochemical mechanisms (CB4, CB05, SAPRC-99): comparisons with measurements during the 2004 ICARTT study, Atmospheric Chemistry and Physics, 10, 3001-3025.

Yu, S., R. Mathur, K. Schere, D. Kang, J. Pleim, and T.L. Otte, 2007. A detailed evaluation of the Eta-CMAQ forecast model performance for O_3, its related

precursors, and meteorological parameters during the 2004 ICARTT study, Journal of Geophysical Research, 112, D12S14, doi:10.1029/2006JD007715.

Zhang, D.-L., H.-R. Chang, N.L. Seaman, T.T. Warner, and J.M. Fritsch, 1986. A two-way interactive nesting procedure with variable terrain resolution, Monthly Weather Review, 114, 1330-1339.

Zhang, D.-L. Y. Shou, and R.R. Dickerson, 2009. Upstream urbanization exacerbates urban heat island effects, Geophysical Research Letters, 36, L244-1, doi:10.1029/2009GL041082.

Zhang, D.-L., Y.-X. Shou, R.R. Dickerson, and F. Chen, 2011. Impact of Upstream Urbanization on the Urban Heat Island Effects along the Washington-Baltimore Corridor, submitted to Journal of Applied Meteorology and Climatology.